FIU Electronic Theses and Dissertations   University Graduate School

4-23-2021

Stimulation Paradigms and Transduction Patterns for Optogenetic Intervention of Astrocytes

Lakshmini Balachandar
Florida International University, lbala010@fiu.edu

FLORIDA INTERNATIONAL UNIVERSITY

Miami, Florida

STIMULATION PARADIGMS AND TRANSDUCTION PATTERNS FOR

OPTOGENETIC INTERVENTION OF ASTROCYTES

A dissertation submitted in partial fulfillment of

the requirements for the degree of

DOCTOR OF PHILOSOPHY

in

BIOMEDICAL ENGINEERING

by

Lakshmini Balachandar

2021

To: Dean John L. Volakis
      College of Engineering and Computing

This dissertation, written by Lakshmini Balachandar, and entitled Stimulation Paradigms and Transduction Patterns for Optogenetic Intervention of Astrocytes, having been approved in respect to style and intellectual content, is referred to you for judgment.

We have read this dissertation and recommend that it be approved.

_____
Jeremy Chambers

_____
Timothy Allen

_____
Jacob McPherson

_____
James Schummers

_____
Wei-Chiang Lin

_____
Jorge Riera Diaz, Major Professor

Date of Defense: April 23, 2021

The dissertation of Lakshmini Balachandar is approved.

_____
Dean John L. Volakis
College of Engineering and Computing

_____
Andrés G. Gil
Vice President for Research and Economic Development
and Dean of the University Graduate School

Florida International University, 2021

ii

DEDICATION

I dedicate this dissertation firstly to my late maternal grandmother, Ms. Rukmani Rajagopalan, whose dreams far exceeded those of my own, to my mom, Dr. Geetha Balachandar for being so motivating and loving, and to my husband, Mr. Ramkrishnan for his unconditional love and moving across the world to support me in this endeavor.

ACKNOWLEDGMENTS

ABSTRACT OF THE DISSERTATION

STIMULATION PARADIGMS AND TRANSDUCTION PATTERNS FOR

OPTOGENETIC INTERVENTION OF ASTROCYTES

by

Lakshmini Balachandar

Florida International University, 2021

Miami, Florida

Professor Jorge Riera Diaz, Major Professor

Gliosis observed in several neurological disorders is associated with neuroinflammation and enhanced astrocytic Ca^{2+} levels. The inherent multicellular nature of this neuroinflammation poses challenges in deciphering the exact role of astrocytic Ca^{2+} signaling and whether it leads to the generation and/or exacerbation of neuroinflammation. These challenges are aggravated by the dearth of systematic characterization of a regulated method for eliciting astrocytic Ca^{2+} increases.

The primary goal of this dissertation is to address the lack of a characterized method by studying optogenetics for eliciting astrocytic Ca^{2+} increases. As part of this analysis, we aim to identify light stimulation paradigms resulting in consistent astrocytic Ca^{2+} increases and assess optogenetic construct serotypes yielding maximum target cell transduction. Firstly, a novel protocol was devised to perform simultaneous optogenetics and astrocytic Ca^{2+} imaging in adult murine brain slices. Neocortical astrocytes exhibited synchronous patterns of Ca^{2+} activity upon light stimulation, drastically different from resting spontaneous activity, and based on the effect of various light paradigms; we identified those conducive for robust astrocytic signaling. Secondly, a theoretical model was

constructed to study the effect of short and long-term light stimulation of optogenetically-enabled (ChR2-expressing) astrocytes on their Ca^{2+} spiking activity and basal level. We further investigated how ChR2 gating dynamics, buffering, and coupling coefficient of Ca^{2+} influence astrocytic activity in a single cell and a network. The response of select variants of ChR2 to varying light stimulation paradigms and key parameters to design future constructs was explored. A preliminary evaluation revealed model similarities to our *in situ* experimental data. Finally, to facilitate future translational work and eventual comparison to current disease models, astrocytic transduction of various serotypes of an AAV optogenetic construct was assessed *in vivo*, and the serotype with maximal transduction efficiency was identified.

Overall, we identified light stimulation paradigms that lead to repeated robust activation of astrocytes and AAV serotypes with high astrocytic transduction efficiency, thereby verifying that via an analysis of light stimulation paradigms and serotype transduction patterns, optogenetics can be implemented for inducing astrocytic Ca^{2+} increases in a controlled and tunable manner.

TABLE OF CONTENTS

LIST OF TABLES

LIST OF FIGURES

CHAPTER 1   INTRODUCTION

Astrocytes, a heterogenous group of non-neuronal cells in the central nervous system (CNS), are involved in several fundamental functions. Rudolf Virchow, in 1858, coined the term neuroglia ("nervenkitt"), referring to "passive, connective cellular elements" in the nervous system, which acted as a "putty" or "nerve glue", in which the "excitable nervous elements were embedded". These cells were called the neuroglia as these connective elements seemed unique with respect to morphology and appearance from those in other parts of the body (Somjen, 1988). Neuroglia was further studied in detail via novel tissue staining techniques developed by Camillo Golgi, an Italian physician and cytologist, and Ramón y Cajal, a Spanish neurohistologist, later in the 19th century. They were the pioneers in elucidating that nerve cells and neuroglia were distinct cellular populations capable of transforming into one another. They also identified a variety of glial morphologies, types, and forms, as well as networks formed in conjunction with other types of non-neuronal cells, like the glial endfeet near blood vessels (De Carlos & Borrell, 2007; Kettenmann & Verkhratsky, 2008; Matias, Morgado, & Gomes, 2019). In 1893, the term 'astrocyte' was introduced by Michael von Lenhossék, the Hungarian anatomist and histologist, which referred to "star-shaped (stellate) glial cells", although electrically silent, their functions were as crucial as neurons (Somjen, 1988; Verkhratsky & Nedergaard, 2018).

1.1   ASTROCYTIC CALCIUM SIGNALING

Ca^{2+} signaling—both local (spatially confined-bearing resemblance to blips and puffs in other cell types) and global (i.e., spikes and intercellular Ca^{2+} waves)—is one of the

fundamental regulatory mechanisms in astrocytes. Astrocytic Ca^{2+} signaling has been widely exploited in the neuroscience community to probe, interrogate and understand the various complexities of astrocytic function and implications of their interplay in neuronal circuitry. Astrocytes exhibit "spontaneous" calcium elevations which propagate throughout the cell, as well as over long distances involving multiple cells (A. C. Charles, 1994; Fatatis & Russell, 1992; Hirase, Qian, Bartho, & Buzsaki, 2004; Nett, Oloff, & Mccarthy, 2002; Parri, Gould, & Crunelli, 2001). These spontaneous calcium transients, which occur in the absence of external triggers are attributed to the release of Ca^{2+} from the IP$_3$ receptors (IP$_3$Rs) clustered on the membrane of the endoplasmic reticulum (ER). Astrocytic Ca^{2+} signaling can also be evoked via agonists *in vitro*, in acute brain slice preparations, and *in vivo*, which have been crucial in providing an avenue for studying intercellular signaling and propagation in glial cells (Cornell-Bell, Finkbeiner, Cooper, & Smith, 1990; Dani, Chernjavsky, & Smith, 1992; Hirase et al., 2004; Porter & McCarthy, 1996; X. Wang et al., 2006). This set the foundation for elucidating a signaling system in the CNS, in addition to neuronal signaling. Astrocytic Ca^{2+} waves were also mediated by purinergic receptors/ATP and propagated to neighboring cells, thereby establishing long-range propagation of intercellular astrocytic signaling (Arcuino et al., 2002; P. B. Guthrie et al., 1999; Hamilton et al., 2008).

1.2   ASTROCYTIC FUNCTION IN THE CNS

The past few decades have witnessed an upsurge in research on understanding the role of astrocytes in brain function. Aside from providing structural support to neurons (Bernardinelli, Muller, & Nikonenko, 2014; Theodosis, Poulain, & Oliet, 2008), regulating

the 'excitatory-inhibitory' neurotransmitter balance (J. J. Riera, Schousboe, Waagepetersen, Howarth, & Hyder, 2008), and finely controlling the brain environment by regulating pH, water and ion homeostasis (Steardo Jr et al., 2015), the exact contribution of these cells, particularly in processes involving their Ca^{2+} signaling, is unknown and is highly debated [see refs (A. Araque et al., 2014; Bazargani & Attwell, 2016; Todd A Fiacco & McCarthy, 2018; Guerra-Gomes, Sousa, Pinto, & Oliveira, 2017; Iadecola, 2017; Khakh & McCarthy, 2015; Lopez-Hidalgo, Kellner, & Schummers, 2017; Savtchouk & Volterra, 2018; Schummers, Yu, & Sur, 2008; Andrea Volterra, Liaudet, & Savtchouk, 2014)]. For instance, astrocytes are thought to be directly involved in neurovascular coupling by sensing neuronal activity and releasing Ca^{2+}-mediated vasoactive agents to relax smooth muscle cells of parenchymal arterioles (Attwell et al., 2010; Lind, Brazhe, Jessen, Tan, & Lauritzen, 2013; Takano et al., 2006). However, recent experimental evidence has thrown the validity of this assumption into disarray by questioning astrocytes' involvement, and the extent of their influence, in the onset of the hyperemic response (Bonder & McCarthy, 2014; Nizar et al., 2013; Takata et al., 2013). Another controversy involving astrocytes is their potential role in modulating neuronal activity via Ca^{2+}-mediated release of gliotransmitters. A flurry of studies following the initial observations of astrocytic Ca^{2+} signaling investigated the feasibility of bidirectional communication between astrocytes and neurons, thereby discovering "gliotransmission"-active transfer of information from glia to neurons (A. Araque et al., 2014; Alfonso Araque, Parpura, Sanzgiri, & Haydon, 1998; A. Araque, Parpura, Sanzgiri, & Haydon, 1999; Parpura et al., 1994; Pascual et al., 2005; A. Volterra & Meldolesi, 2005). These studies thereby established astrocytes as active partners with neurons in synaptic signaling in the central nervous system. While

3

several groups present evidence for the active involvement of gliotransmission in neuromodulation, others argue that this process is not likely to occur under physiological conditions (Agulhon et al., 2012; Todd A Fiacco & McCarthy, 2018; Savtchouk & Volterra, 2018).

1.3 ASTROCYTES IN BRAIN DISORDERS

CNS injury has been associated with astrocytes, among other cell types, undergoing significant morphofunctional changes, proliferation, and hypertrophy, termed as reactive gliosis (Burda, Bernstein, & Sofroniew, 2016; Hamby & Sofroniew, 2010). In its acute phase, reactive gliosis is a mechanism for neuroprotection, important for the restoration of homeostasis and lesion demarcation. Reactive astrocytes form a barrier between the lesion and the surrounding brain tissue, e.g., in focal ischemic lesions and in Alzheimer's Disease (AD), where they inhibit the growth of amyloid plaques and restrict microglial infiltration (Pekny & Pekna, 2016). They have been reported to have stem-cell-like properties with the possibility of differentiating into other cell types (Robel, Berninger, & Gotz, 2011; Sirko et al., 2013). In the cases of acute ischemic stroke, they play a crucial role in ischemic preconditioning, scavenging reactive oxygen species, and enhancing neuronal survival (Pekny & Pekna, 2014, 2016).

In the chronic phase of infections, reactive gliosis could also become detrimental to the brain environment. They might exacerbate the neuroinflammatory milieu, leading to extensive glial scar formation, inhibiting axonal growth, regeneration, and functional recovery. Aside from reactivity, astrocytes also undergo atrophy or asthenia with loss of function and pathological remodeling in neuropsychiatric disorders and neurodegeneration

(Verkhratsky, Steardo, Parpura, & Montana, 2016). Astrocytes undergo specific morphological alterations, and there is an increase in hypertrophic soma and processes (Losi, Cammarota, & Carmignoto, 2012; Pekny & Pekna, 2014). In affected brain areas, there is morphofunctional remodeling and generalized dysfunction of astroglial-dependent homeostasis due to changes in receptors, ion channels, and vessel calcification (Bedner et al., 2015; Steinhäuser, Grunnet, & Carmignoto, 2016; Zarb et al., 2019). An enhanced expression of glial fibrillary acidic protein (GFAP) has been observed in several disease models, both in experimental studies and human pathology (Eng, Ghirnikar, & Lee, 2000; Pekny & Pekna, 2014; Seiffert et al., 2004). The expression of glutamine synthetase is altered in several neurological conditions, including toxic damage to the brain and mood disorders like Schizophrenia (Verkhratsky, Steardo, et al., 2016). Due to their intimate relation with microvasculature resulting from wrapped astrocytic endfeet around endothelial cells, astrocytic dysfunction results in modifications in vascular tone (Girouard & Iadecola, 2006; Tian et al., 2005) and blood-brain barrier (BBB) permeability. This results in BBB damage, enhanced angiogenesis, and disruption of tight junction proteins.

Astrocytes work closely with microglia—the innate immune cells in the CNS—which are activated by brain injury/insults. Following this, there is a production of cytokines, chemokines and trophic factors like TNFα, TGF- β, ILs and activation of toll-like receptors (TLRs) in several disorders, including epilepsy (temporal lobe, focal cortical dysplasia (FCD-II), etc.) and nervous system infections like meningitis and encephalitis, leading to the modulation of neuroinflammation (Aronica, Ravizza, Zurolo, & Vezzani, 2012; Deshmukh et al., 2018; Devinsky, Vezzani, Najjar, De Lanerolle, & Rogawski, 2013;

5

Hanisch, 2002; Pascual, Ben Achour, Rostaing, Triller, & Bessis, 2012; Verkhratsky, Steardo, et al., 2016).

Astrocytic Ca^{2+} homeostasis is dramatically altered in astrocytes under several pathological conditions. These include elevated Ca^{2+} levels, as well as intercellular waves in epilepsy (Heuser et al., 2018), AD (Kuchibhotla, Lattarulo, Hyman, & Bacskai, 2009; J. Riera, Hatanaka, Uchida, Ozaki, & Kawashima, 2011), and spreading depression (Kunkler & Kraig, 1998; Peters, Schipke, Hashimoto, & Kettenmann, 2003). Larger aberrant Ca^{2+} signals are observed in ischemic cores of acute stroke models and Alexander Disease (Shigetomi, Saito, Sano, & Koizumi, 2019). The implications of astrogliosis, its disease-specific repercussions, and its effects, along with changes in astrocytic networks, are yet to be fully unraveled. Understanding the role of elevated astrocytic Ca^{2+} in the development of tissue hyperexcitability and reactivity can offer insights into astrocytic function and better understand their role in neuroinflammation, which remains elusive.

1.4   MODULATION OF ASTROCYTIC ACTIVITY

Studying the role of astrocytes in health and disease relies on controlled and tunable eliciting of astrocytic Ca^{2+} signaling. Several research groups have demonstrated the ability to elevate Ca^{2+} activity in astrocytes via electrical (A. Araque et al., 1999; Fleischer, Theiss, Slotta, Holland, & Schnitzler, 2015; Hassinger, Guthrie, Atkinson, Bennett, & Kater, 1996; Monai & Hirase, 2016; Monai et al., 2016; Nedergaard, Cooper, & Goldman, 1995), mechanical (Andrew C Charles, Merrill, Dirksen, & Sandersont, 1991; Peter B Guthrie et al., 1999; Stout, Costantin, Naus, & Charles, 2002) and pharmacological (Bonder & McCarthy, 2014; Durkee et al., 2019; Jeremic, Jeftinija, Stevanovic, Glavaski, & Jeftinija,

2001; Parpura et al., 1994) approaches. Electrical stimulation lacks cell specificity due to potential concurrent activation of neurons and suffers low spatial resolution. Mechanical stimulation, performed to mimic responses to brain injury and spreading depression (Ellis, McKinney, Willoughby, Liang, & Povlishock, 1995; Nedergaard et al., 1995), lacks clinical feasibility. The use of pharmacological techniques for targeting these cells in the brain has been limited to basic research due to high invasiveness and low temporal resolution. Contrarily, optogenetics is an avant-garde minimally invasive approach that provides a platform for genetically targeting specific cell types with high temporal and spatial precision (Adamantidis, Zhang, de Lecea, & Deisseroth, 2014; Deisseroth, 2015; Fenno, Yizhar, & Deisseroth, 2011; Krook-Magnuson, Ledri, Soltesz, & Kokaia, 2014). For facilitating optogenetic intervention of astrocytes, it is essential to identify light stimulation paradigms conducive for eliciting Ca^{2+} signaling. This is further described in detail in this dissertation, with *in situ*, *in silica,* and *in vivo* approaches, and sheds light on how Ca^{2+} signaling can be studied and manipulated.

1.5 CHANNELRHODOPSIN 2—AN OPTOGENETIC CONSTRUCT

Despite the recent inception of the field of optogenetics, a wide variety of optogenetic tools have been constructed, among which channelrhodopsin 2 (ChR2) has been one of the most used. It is an algal-derived light-sensitive cationic channel, which undergoes a conformational change from all-trans to cis configuration upon exposure to blue light. The biophysical characterization and the response to light stimulation in several ChR2 variants, predominantly in excitable cells, are available in literature (John Y Lin, 2012; J. Y. Lin, Lin, Steinbach, & Tsien, 2009). Several ChR2 variants have been engineered for enhanced

channel conductance (ChETA) (Gunaydin et al., 2010), increased calcium permeability (CaTCh) (Kleinlogel et al., 2011), and faster recovery kinetics (ChRET/TC) (André Berndt et al., 2011).

ChR2 constructs have also been modified to create bi-stable opsins, where photocurrents via the channel can be initiated and terminated precisely with different wavelengths of light. An example would be the ChR2(C128S) variant which is ~300 times more sensitive to light than the wild-type variant, with long-term activation and precise switching between the open and closed states of the channel (A. Berndt, Yizhar, Gunaydin, Hegemann, & Deisseroth, 2009). Applications of optogenetics in astrocytes have helped examine the role of these cells in memory enhancement (Adamsky et al., 2018), cortical state switching (Poskanzer & Yuste, 2016), and hyperemic response (Masamoto et al., 2015; Takata et al., 2018). However, contrary to neurons, a holistic approach to quantify the effect of light stimulation on astrocytes has not yet been formulated.

1.6 ASTROCYTIC GENE DELIVERY FOR OPTOGENETIC INTERVENTION

1.6.1 Viral delivery of the optogenetic construct

Viral delivery of the optogenetic construct has precise localization of cellular targeting and is time and cost-effective (Kuhlman & Huang, 2008). Viral delivery vector backbones are of multiple types—Lentiviral (LV), Adeno-viral vectors (AVV), Retroviral (RV), and Adeno-associated viral (AAV). The backbone choice is solely based on application, with LV, AVV, and RV facing immunogenic responses upon integration with the host. AAVs, on the other hand, are desired for a multitude of reasons – their characteristics of low

immunogenicity, ability to efficiently target both dividing and non-dividing cells, robust gene delivery, and persistence of expression in rodent models make them very potent tools for research and gene therapy. They can be engineered to facilitate high transduction capabilities of a diverse set of target tissues and species (McCown, Xiao, Li, Breese, & Samulski, 1996; Sushrusha Nayak & Roland W Herzog, 2010; S. Sun & Schaffer, 2018). Cellular targeting using AAV-based optogenetics requires an appropriate selection of the AAV serotype (expression of cell surface antigens). The serotype determines transduction efficiency (incorporation of genetic material in the cell) and differs based on target cell type, brain area, species of intervention, and construct size.

1.6.2 Animal genetic engineering approach

A transgenic animal model for optogenetic control of astrocytes serves as a non-invasive modality for controlling and manipulating astrocytes. The mouse model (Mlc1-tTA::tetO-ChR2(C128S)-EYFP developed by Tanaka *et al.* (Tanaka et al., 2012) offers an expression of ChR2(C128S), the bistable opsin in astrocytes viz the MlC1 promoter. This facilitates an effective control modality of astrocytes to study their implications in neuroinflammatory cascades in the brain.

1.7 OVERVIEW OF THIS DISSERTATION

Despite the involvement of astrocytes in neuroinflammation and several multi-cellular phenomena in the brain, differentiating their specific contributions from concurrent neuronal activity has remained one of the most enduring challenges in the field. Probing the exact role of astrocytic Ca^{2+} signaling and its involvement in the generation of neuroinflammation can offer answers to delineate their contribution in unveiling the

pathophysiology behind this multifaceted process. To understand the role of astrocytic Ca^{2+} signaling and its implications in neuroinflammation, it is crucial to first establish robust control and manipulate astrocytes, using a technique like optogenetics due to its high cellular specificity and temporal resolution. To achieve this, it is important to systematically characterize and identify light stimulation paradigms and transduction patterns for inducing regulated, on-demand increases in astrocytic Ca^{2+}.

The overall goal of this dissertation is to provide a holistic characterization of a) induced increases in astrocytic Ca^{2+} due to varying light stimulation paradigms and b) optogenetic construct serotype transduction targeting astrocytes to implement optogenetics for inducing astrocytic Ca^{2+} increases, in a controlled and tunable manner. The specific aims listed below serve to accomplish these goals.

1.8   SPECIFIC AIMS

1.8.1   Specific Aim 1

Specific Aim 1 is to develop a method to characterize astrocytic Ca^{2+} responses elicited by various light stimulation paradigms and implement it for *in situ* studies. Challenges include a) the accelerated deterioration of *in situ* slice health and age-related changes associated with the usage of adult animals for Ca^{2+} imaging, b) the overlapping light issues between ChR2 and the Ca^{2+} indicator during simultaneous optogenetic stimulation and imaging, and c) a lack of understanding of the effect of various light stimulation paradigms on astrocytic Ca^{2+} response.

This specific aim can be subdivided into the following sub aims:

a) Establishment of the transgenic mouse line

b) Protocol for slice collection and Rhod-2 AM loading in adult mice

c) Setup for simultaneous optogenetic stimulation and Ca^{2+} recording

d) *In situ* experiments for varying light stimulation paradigms

1.8.2   Specific Aim 2

Specific Aim 2 is to construct a theoretical model of optogenetically-enabled astrocytes to study Ca^{2+} responses and compare with experimental observations. A systematic study quantifying the response of optogenetically modified astrocytes to light, both short-term and long-term, can aid in further understanding the behavior of astrocytic Ca^{2+} to light stimulation and is yet to be performed. Given that light activation of ChR2-enabled astrocytes alters dynamics of intracellular ionic species, mathematical modeling can be of importance in predicting how laser specifications, as well as the biophysical properties of the ChR2 construct, can affect astrocytic Ca^{2+} signaling.

This specific aim can be subdivided into the following sub aims:

a) Construct a mathematical model for a single astrocyte and network activity

b) Study effects of various light paradigms (T, δ, intensities), buffering, network connectivity, ChR2 biophysical properties on astrocytic Ca^{2+}

c) Perform sensitivity analysis

d) Tuning model parameters for comparison with experimental data

1.8.3 Specific Aim 3

Specific Aim 3 compares astrocytic transduction of various serotypes of an optogenetic construct targeting astrocytes *in vivo*. Rat-based models for studying a variety of brain disorders, including AD (Do Carmo & Cuello, 2013), FCD-II (Deshmukh et al., 2018), and Huntington's Disease (HD) (Hohn et al., 2011), can benefit from the translation of ChR2-based intervention of astrocytes. This can aid in understanding the roles of astrocytic Ca^{2+} signaling in several of these disorders and explore their translational potential. However, AAV-ChR2 capsid serotypes targeting astrocytes in the *in vivo* rat brain cortex have not been previously characterized.

This specific aim can be subdivided into the following sub aims:

a) Experimental protocol for AAV microinjection

b) *In vivo* experiments

c) Cryo-sectioning, imaging, and analysis

1.9   ORGANIZATION OF THE DISSERTATION

Chapter 1 serves as an introduction to this dissertation, including relevant literature, background and discusses the rationale, specific aims, and organization of the dissertation.

In Chapter 2, we provide an experimental setting that uses live adult murine brain slices from a knock-in model expressing ChR2(C128S) in cortical astrocytes, loaded with Rhod-2 AM to elicit robust Ca^{2+} response to light stimulation. We develop and standardize a protocol for brain extraction, sectioning, Rhod-2 AM loading, slice health maintenance,

and Ca^{2+} imaging during light stimulation. We demonstrate how this can be successfully applied to optogenetically control adult cortical astrocytes, test and compare several stimulation paradigms, and elicited astrocytic responses in contrast with resting spontaneous activity. We identify light stimulation paradigms that can be used to induce astrocytic Ca^{2+} increases in a controlled, robust and regulated manner in the order of ~10 minutes.

In Chapter 3, we design a novel stochastic model of Ca^{2+} dynamics in astrocytes that incorporates a light-sensitive component—ChR2. Utilizing this model, we investigate the effect of different light stimulation paradigms on cells expressing select variants of ChR2 (wild type, ChETA, and ChRET/TC). We analyze how depending on paradigm specification, astrocytes might undergo drastic changes in their basal Ca^{2+} level and spiking probability, both in short-term (order of minutes) and long-term (order of hours), as an extension of our *in situ* work. Furthermore, we perform a global sensitivity analysis to assess the effect of variation in parameters pertinent to the shape of the ChR2 photocurrent on astrocytic Ca^{2+} dynamics. Additionally, we evaluate the effect of Ca^{2+} buffering and coupling coefficient in a network of ChR2-expressing astrocytes and their implications on the astrocytic basal level in the stimulated region and propagation of calcium activity to unstimulated cells. We also discuss the comparison of our theoretical model to our *in situ* astrocytic Ca^{2+} imaging data.

In Chapter 4, we focus on the translational aspect of the optogenetic setup and its adaptation to perform optogenetics in a rat model, which can in the future be compared to several neurological disorder models. We evaluate AAV serotypes 1, 5, and 8 of the vector AAV-

GFAP-hChR2(H134)-mCherry targeting astrocytes in the rat brain neocortex, study corresponding transduction patterns, and identify the serotype yielding the highest astrocytic transduction.

In Chapter 5, we discuss the significance of this dissertation, its limitations, and the future avenues to be explored.

CHAPTER 2   SIMULTANEOUS CA²⁺ IMAGING AND OPTOGENETIC STIMULATION OF CORTICAL ASTROCYTES IN ADULT MURINE BRAIN SLICES

The partial contents of this chapter are published in Current Protocols in Neuroscience as Lakshmini Balachandar, Karla A. Montejo, Eleane Castano, Melissa Perez, Carolina Moncion, Jeremy W. Chambers, J. Luis Lujan, and Jorge Riera Diaz. "Simultaneous Ca²⁺ Imaging and Optogenetic Stimulation of Cortical Astrocytes in Adult Murine Brain Slices" (Balachandar et al., 2020).

2.1   INTRODUCTION

Several disease models studying brain disorders employ adult mice (>2 months) to investigate disease progression (Maragakis & Rothstein, 2006; J. Riera, Hatanaka, Uchida, et al., 2011; Verkhratsky, Rodriguez, & Parpura, 2014). Calcium serves as a ubiquitous second messenger for intracellular signaling cascades that mediate astrocytic function. Live calcium imaging is utilized to gauge astrocytic activity and to determine its role in disease and health (T. A. Fiacco & McCarthy, 2006; Verkhratsky & Kettenmann, 1996). However, the study of adult (>2 months) and aged (>18 months) animals is challenging due to age-related increase in oxidative stress, glutamatergic excitotoxicity due to higher synaptic spine density and morphofunctional changes disrupting homeostasis, leading to a rapid decline in the viability of acute slices (Matias et al., 2019; Verkhratsky, Zorec, Rodriguez, & Parpura, 2016).

To investigate the role of astrocytic Ca²⁺ dynamics and its implications in neuroinflammation, it is essential to use a non-invasive approach like optogenetics, which provides a platform for targeting and activating specific cell types with a high temporal

and spatial resolution (Adamantidis et al., 2014; Deisseroth, 2015; Fenno et al., 2011). Optogenetics also employs the development of transgenic models to genetically target astrocytes, rendering them sensitive to light. The knock-in mouse model developed by Tanaka *et al.* (Tanaka et al., 2012) offers an expression of ChR2(C128S) in astrocytes (viz the MlC1 promoter), which is opened by blue light, closed by amber light, and carries a channel fluorescence readout—an Enhanced Yellow Fluorescent Protein (EYFP) tag. Notably, this leaves a narrow excitation spectrum for a fluorescent Ca^{2+} indicator. Therefore, when using a ChR2 mouse model, it is vital to use a red-shifted Ca^{2+} indicator like Rhod-2 AM. Several research groups using infant mice brain slices (P14-P20) (He, Linden, & Sapirstein, 2012; W. Sun et al., 2013; Takano et al., 2014) and Robillard et al. (Robillard, Gordon, Choi, Christie, & MacVicar, 2011) employ Rhod-2 AM in murine hippocampal slices. In this article, we provide a protocol for Rhod-2 AM staining to study cortical astrocytes in adult murine brain slices.

In this chapter, we describe a method for utilizing adult (2-5 months) mice brain slices from the abovementioned transgenic mouse model to assess astrocytic Ca^{2+} responses to light stimulation in the murine neocortex. We have developed and standardized a protocol for mouse brain extraction, vibratome sectioning, slice recovery, Rhod-2 AM loading, slice health maintenance, and Ca^{2+} imaging during light stimulation in these adult brain slices. Upon stimulation with light, cortical astrocytes exhibited robust increases in Ca^{2+} activity qualitatively different from resting spontaneous activity. Simultaneous optogenetics and functional imaging in situ in adult murine cortical astrocytes can provide information on their role in neurodegenerative disorders, including epilepsy, AD, stroke, and Parkinson's

disease. Notably, many of these diseases exacerbate over time, and the protocol provided can be applied to longitudinal studies on mice of various ages.

Basic Protocol 1 describes the experimental setup and describes the steps crucial for efficient adult murine brain tissue processing—brain extraction, mounting, sectioning, and Rhod-2 AM loading for successful Ca^{2+} imaging, with a strategic overlap of timelines suggested. The recipes for making the cutting solution and artificial cerebrospinal fluid (aCSF) are listed, both of which are critical for maintenance of slice health of the adult brain slices and aimed towards minimizing slice degradation due to oxidative stress. Additionally, the protocol delves into the vibratome setup with critical sectioning parameters suitable for acquiring healthy brain slices, experimental checkpoints, and recovery of the adult mice brain slices. Lastly, the protocol also elaborates on the suitable Rhod-2 AM concentration, bulk tissue loading, and appropriate temperatures, in addition to incubation times. Basic Protocol 2 discusses the setup for performing simultaneous optogenetic stimulation and calcium imaging of adult murine cortical astrocytes. The outline for time-lapse confocal image acquisition of mice brain slices, data processing, and analysis are given in this chapter. Astrocyte specificity of Mlc1-ChR2-EYFP expression in the transgenic model is leveraged to differentiate astrocytes of interest from other Rhod-2 AM loaded cell types, with elaboration on pre-processing, motion correction, and fluorescence time-series analysis of astrocytic Ca^{2+} responses.

Additionally, we investigate the effect of various light stimulation paradigms and repeated stimulations on astrocytic Ca^{2+} dynamics. In this process, we also identify paradigms that lead to robust astrocytic responses very time the light is incident and characterize several

astrocytic Ca^{2+} signaling parameters to compare the effect of the light stimulation paradigms.

2.2 EXPERIMENTAL SETUP, SLICE PREPARATION, AND RHOD-2 AM STAINING

This protocol has four sections. The first section describes the preparation and setup needed for performing acute slice experiments employing adult mice brains. The second section outlines the steps necessary for efficient mouse brain extraction, mounting, settings for vibratome sectioning, and incubation parameters. The third and fourth sections discuss the preparation steps of Rhod-2 AM and bulk tissue loading for subsequent Ca^{2+} imaging, respectively. All experimental procedures and animal care in this protocol are approved by the Institutional Animal Care and Use Committee (IACUC) at Florida International University (Approval No. 19-045), IBC exception protocol (18-006), and NIH guidelines. tTA-MlC1-tetO-ChR2(C128S)-EYFP mice (2-5 months old) are housed in standard cages at a 12h-12h light-dark cycle with free access to food and water.

NOTE: A similar protocol must be approved by your IACUC before initiating.

2.2.1 Materials

1) Anhydrous dimethyl sulfoxide (DMSO; Life Technologies cat. no. D12345); **2)** 20% Pluronic (Biotium cat. no. 59004); **3)** Kolliphor EL (Sigma Aldrich cat. no. C5135); **4)** Antibacterial soap; **5)** Deionized water; **6)** Isopropyl alcohol (Fisher Scientific cat. no. A4591); **7)** Cutting solution (see Table 2-1 for recipe); **8)** Tissue adhesive (Ted Pella, cat. no. 10033); **9)** Agarose gel mount: 2.5% [Agarose (Invitrogen, cat. no. 16500) in TAE

[Fisher Scientific cat. no. BP13351]); **10)** Anesthetic (as specified by the approved animal care protocol); **11)** Mice: tTA-MlC1-tetO-ChR2(C128S)-EYFP (2-5 months old, bred in house after obtaining mice lines; RIKEN, Japan RBRC05450 and RBRC05454); **12)** Rhod-2 AM (ThermoFisher Scientific, cat. no. R1245MP); **13)** aCSF (see Table 2-1 for recipe); **14)** Pyrex Heavy-Duty Griffin beakers (Fisher Scientific 2 L - 02-555-25H, 1 L - 02-555-25F, 600 ml - 02-555-25D); **15)** Vibratome (Model: Vibratome 1000 Plus); **16)** Water bath (Polyscience, cat. no. WB10A11B); **17)** pH meter (Fisher Scientific, cat. no. Accumet AB150); **18)** Mixed gas tanks (95% O_2, 5% CO_2; Airgas, cat. no. UN3156); **19)** 50-ml tubes (Fisher Scientific, cat. no. 1443222); **20)** Anesthesia machine (Vetamac, VAD compact research machine); **21)** Digital scale (Ohaus, cat. no. 30253027); **22)** Induction chamber (Vetequip, cat. no. 941448); **23)** Biohazard bag (Thomas Scientific, cat. no. P410812); **24)** Decapicone (Braintree Scientific cat. no. MDC-200); **25)** Rodent guillotine; **26)** Clock or timer; **27)** Iris scissors, 14-cm supercut curved scissors (World Precision Instruments, cat. no. 503262); **28)** Double-edged safety razor blades, use one half per preparation (wiped with EtOH); **29)** Scalpel (Carbon Steel Blades #22; IMS, cat. no. CBLD22); **30)** Forceps, 25.5.cm (World Precision Instruments, cat. no. 500364-G); **31)** Fine spatula (World Precision Instruments, cat. no. 504022); **32)** Kimwipes; **33)** Plastic transfer open pipettes (Globe Scientific Inc., cat. no. 135040); **34)** Custom-designed recovery chamber: made by open trimming of four 50-ml tubes (~ 3-4 cm in height), heat glued together to a fine plastic mesh (200 mesh; ATPWONZ cat. no. 4335511389) (see Figure 2-1A, recovery step); **35)** Vortex mixer (Fisher Scientific, cat. no. 02215365); **36)** Mini-Centrifuge (Southwest Sciences, cat. no. SC1008-B); **37)** Ultrafree Centrifugal Filters (Millipore, cat. no. Duropore; PVDF 0.22 µm); **38)** Sonicator (Branson, cat. no.

19

1800); **39)** 6-well plate (Fisher Scientific, cat. no. 0720083); **40)** Custom-designed bubbling probes for the 6-well plate: made using PTFE tubing (0.7 mm I.D.; PerkinElmer. cat. no. B0507021) anchored by Eppendorf foam slivers and tape (see Figure 2-1A, orange anchors in staining step); **41)** 15 ml tubes (Fisher Scientific, cat. no. 1495949D).

2.2.2 Experimental preparation and setup

1. Prepare surfactant stocks once a month. *Pluronic*: Make 10% Pluronic from the 20% stock in DMSO. *Kolliphor EL*: Make a 5% solution in DMSO.

2. Clean all beakers used to prepare and contain aCSF thoroughly using antibacterial soap and water, followed by a final deionized (DI) water rinse.

3. Rinse the vibratome chamber, specimen holder, and blade holder with antibacterial soap and water, followed by an isopropyl alcohol spray and a final DI water rinse. *If oil is present on the blade holder, clean with an isopropyl alcohol-soaked Kimwipe.*

4. Warm the 10% Pluronic in the water bath at 34°C; this facilitates complete Pluronic dissolution.

5. Make 1.5 L of the cutting solution and 0.75 L of aCSF according to the recipes (see Table 2-1).

6. Standardize the pH meter and adjust the pH of the solutions in the range of 7.3-7.4 by titration.

7. Bubble the solutions with mixed gas (95% O_2, 5% CO_2) and recheck pH *(Bubbling with mixed gas makes the cutting solution more basic and aCSF more acidic)*. Titrate the solutions

20

to bring them within the range of 7.3-7.4. It is critical to maintain this pH range for longevity of good slice health.

8. Mix equal parts of the cutting solution and aCSF to fill the incubation beaker (400 ml in the 600-ml beaker). This solution will serve as the mixed recovery solution, used later in the experiment for recovery of brain slices (step 17). Place it in the water bath (34°C), and start bubbling with mixed gas *(Bubbling makes this solution more basic)*. Titrate the pH of the mixed solution so that it ranges from 7.3-7.4. Wait for the mixed solution to come to temperature before use. This solution will be used for the recovery step after slicing.

9. Freeze a portion of the ice-cold cutting solution (about 200 ml, distributed in 50- ml tubes) at -20°C to be used for brain extraction and temperature control during sectioning (see step 15). Freeze the remaining solution at -5 to -10°C to be used for filling the vibratome buffer tray to collect sections. The freezing step usually takes about 1.5-2 hr. The ice-cold cutting solution used during extraction should be the consistency of a slush *(Complete freezing should be avoided to not drastically alter the osmolality)*. This solution preserves the enzymatic activity of tissue and slows metabolism while slightly stiffening tissue for optimal sectioning.

2.2.3   Slice preparation

10. Prepare the surgical suite with the anesthesia machine, digital scale, induction chamber, dissection tools, biohazard bag, and decapicone *(keep the dissection tools on ice until decapitation)*.

11. Before starting the experiment, do the following:

a. Use the blade angle indicator to adjust the angle of the sectioning blade on the vibratome to 25°.

b. Wipe razor blade half with isopropyl alcohol before inserting into blade holder on the vibratome (see Figure 2-1A).

c. Fill the vibratome half-way with the ice-cold cutting solution and begin bubbling with mixed gas.

d. Ensure that all solutions are saturated with carbogen before use, ensuring stable pH buffering and adequate oxygenation.

e. Check that the mixed recovery solution pH is maintained between 7.3 and 7.4 and immerse the recovery chamber in the mixed solution beaker such that it is half- immersed in the solution and held by bent zip ties hanging off of the rim of the beaker *(complete immersion of the recovery chamber will lead to floating of slices, lack of immersion will lead to drying and damage of brain slices)*. This solution is to be maintained at 34°C in the water bath.

f. Make a suitable agarose block (see step 14 below) to provide mechanical support to the brain and glue it to the vibratome head using the biocompatible tissue adhesive (curing time ∼ 10 s).
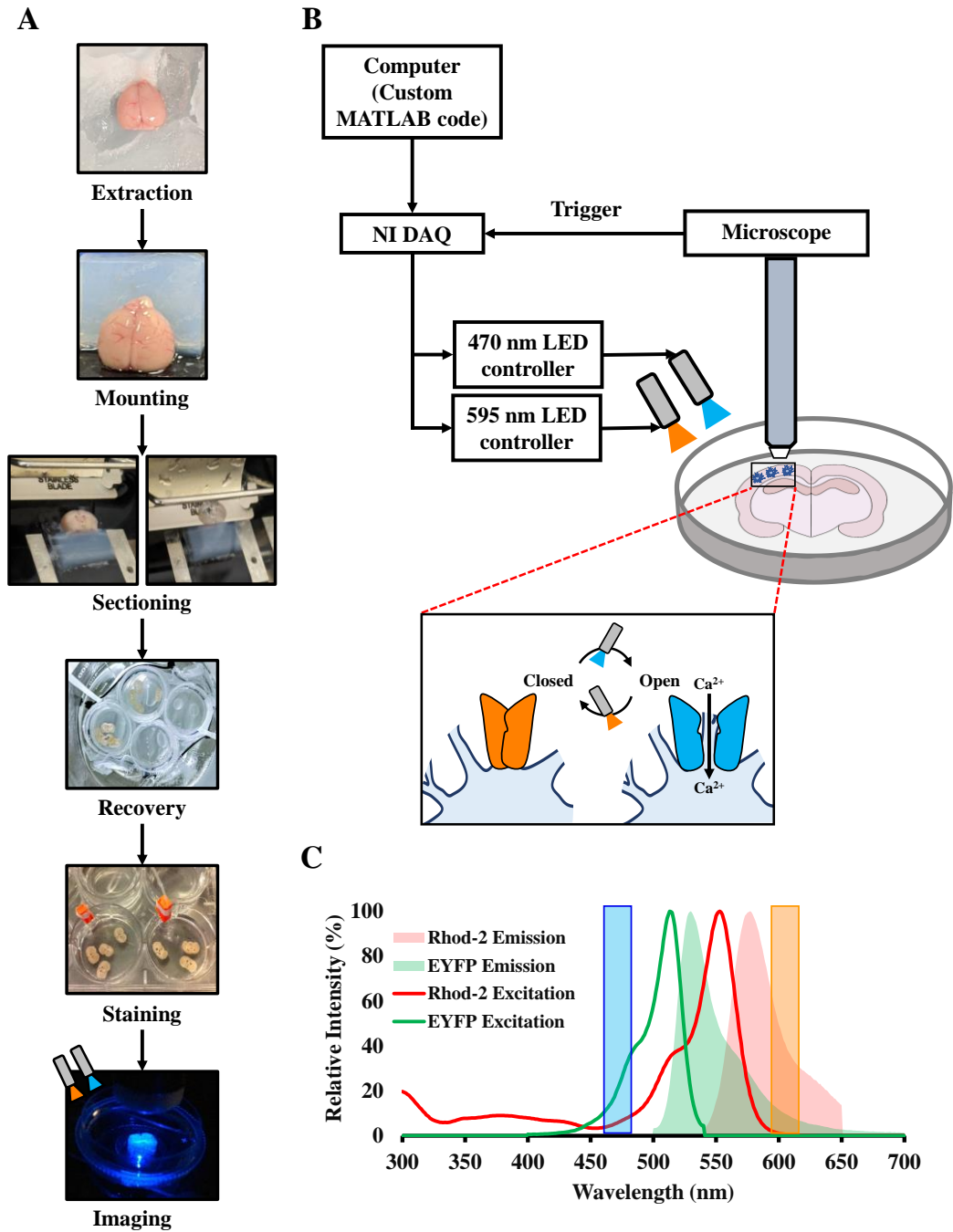
Figure 2-1 Experimental setup for simultaneous optogenetics and Ca²⁺ imaging. (**A**) Flowchart of the entire experiment, including extraction, tissue processing, staining, and imaging. (**B**) Schematic of the setup for simultaneous optogenetic stimulation and confocal imaging of a murine coronal brain slice. Inset shows closed and open configurations of Mlc1-ChR2(C128S)-EYFP on the astrocytic membrane, opened by blue light to allow an influx of Ca²⁺ and closed by amber light. (**C**) Excitation-emission spectra of Rhod-2 AM and EYFP. Blue and Amber shaded bars represent wavelengths of LED illumination of the brain slice during light stimulation.

12. Anesthetize the mouse for initial induction with 5% isoflurane with 1 L/min O_2, 14.7 PSI. Once the mouse loses righting reflex, change isoflurane to 1.5% for maintenance. Once animal breathing stabilizes (40-60 bpm), switch off isoflurane, flush the induction box with O_2 to prevent anesthetic inhalation. Open the box and place the animal inside the decapicone. Decapitate rapidly using the guillotine while starting the timer.

13. Extract the brain on the semi-solidified ice-cold cutting solution in under 3 min (see Figure 2-1A). To extract the brain, using the Iris scissors, cut through the scalp and expose the skull. Cut in the front between the eyes and the back of the skull where the cerebellum begins, such that only the forebrain remains. Carefully slide the scissors between the skull and the brain to gently cut along the midline of the skull. Exercise caution for the scissors to not scrape the brain to prevent damage. Use the forceps to pry open the skull pieces to each side, and using the fine spatula, gently extract the brain onto the frozen cutting solution.

14. After verifying that no damage is evident on the neocortex, gently dry the brain sufficiently (by removing surrounding liquid using a Kimwipe) to glue the brain's base to the vibratome head using biocompatible tissue adhesive. Place ventral surface against agarose, ensuring that the brain is pressed against the agarose support block (Figure 2-1A, mounting step) and that agarose height does not exceed a couple of millimeters above the brain, as this will delay initial gross trimming to remove the olfactory bulb.

15. Fill the vibratome chamber with ice-cold cutting solution, including any chunks of ice that may have formed, until the blade is submerged. Begin sectioning to perform initial trimming and further to achieve 350-μm coronal sections. We obtain good sections on a Vibratome 1000 Plus at a speed setting of 1.5 (0.3 mm/s) and an amplitude setting of 8 (1.6

mm). *Sectioning of an entire brain takes about 30 min; longer sectioning times can lead to deterioration of slice health.*

16. After each slice is obtained, transfer with a plastic transfer pipette (cut the end of the pipette to produce a wide opening) to incubate in the recovery chamber immersed in the mixed solution at 34°C with active bubbling. Incubate for 30 min at 34°C once the last slice is collected. *At this time, prepare the dye cocktail (see step 18 below) and sonicate for 30 min.*

17. Move the beaker (from step 16) containing the slices to room temperature (RT) and maintain bubbling for an additional 30 min.

2.2.4   Rhod-2 AM preparation

We have determined that for 350-μm adult mice brain slices, a concentration of 5.7 μM is optimal for Rhod-2 AM staining and imaging in the neocortex. This dye concentration was selected because higher concentrations led to dye blotches in the slices, observed while imaging.

18. Dissolve Rhod-2 AM in 8 μl of 10% Pluronic/DMSO and subsequently add 8 μl of 5% Kolliphor EL/DMSO. Vortex this dye mix, and briefly spin down [5-10s at 2000g (~6000 rpm)], RT by centrifuging, and then bring up the volume to 250 μl using aCSF.

19. Filter the dye through the centrifugal filter tube for 20-30 s at 2000g (~6000 rpm), RT. Add the filtrate to 7.75 ml of aCSF (total 8 ml of 5.7 μM Rhod-2 AM) in a 15-ml tube. Sonicate for 30 min before adding to the slices.

2.2.5 Bulk tissue loading with Rhod-2 AM

20. Using an open pipette, place slices in a 6-well plate (3-4 slices/well).

21. Remove excess solution while ensuring that a thin film of liquid remains over the slices *(this is to prevent slice health deterioration due to drying)*.

22. Add the Rhod- 2 AM dye solution by gently placing it on each of the slices before filling the well (total volume/well ~4 ml). Start bubbling mixed gas using the custom-made probes by placing one probe in each well of the 6-well plate containing the slices. Adjust the pressure such that the slices do not swirl in the 6-well plate while getting bubbled.

23. Place the 6-well plate at 34°C in a water bath for 45 min while bubbling. Fill adjacent wells (not containing brain slices) with aCSF and bubble using additional custom-designed probes (this solution will be used in steps 24 and 25 for washing and de-esterification).

24. After 45 min, remove the bubbling probes and wash the slices by gently pipetting out the staining solution followed by immediate addition of freshly bubbled aCSF (from the adjacent wells). Repeat this step 2-3 times.

25. Add fresh aCSF (~4 ml) and allow slices to de-esterify in the 6-well plate for 30 min at RT while resuming bubbling.

26. After 30 min, transfer the slices using an open pipette into a 50-ml beaker containing fresh aCSF, under constant bubbling for imaging afterward.

The entire protocol (Figure 2-1A) takes approximately 3 hours.

2.3   IMAGE ACQUISITION AND ANALYSIS

In this article, we validate Rhod-2 AM loading of adult murine cortical astrocytes and the ability to perform simultaneous optogenetics and Ca^{2+} imaging. We discuss an example setup (block stimulation paradigm) for performing optogenetic stimulation and provide an outline for confocal image acquisition; the corresponding data processing and analysis are also given in this protocol. It is noteworthy that the analysis of Ca^{2+} imaging data can be done by using other equivalent software, and implementing the suggested software is not a limiting factor in performing simultaneous Rhod-2 AM imaging and optogenetic stimulation.

2.3.1   Materials

1) aCSF (see Table 2-1 for recipe) Brain slices (see Basic Protocol 1); **2)** Imaging chamber: 35-mm dish superglued on a slide (Southern Labware cat. no. 706011); **3)** Kimwipes; **4)** Open transfer pipette; **5)** Custom tissue restraining harp: nylon fibres glued using tissue adhesive to flattened inert metal (e.g., silver) shaped as a harp; **6)** 10X Water objective (Olympus cat. no. UMPlanFLN); **7)** Confocal microscope (Model: Olympus FV 1200 with filter cubes cat. no. U-N49002 and U-N49004); **8)** Microscope TTL cable (Olympus cat. no. FV-TTLCA); **9)** Data Acquisition (DAQ) System – NI USB 6259; **10)** BNC Power Meter (Thorlabs cat. no. PM100A), **11)** Silicon Power Head (Thorlabs cat. no. S120C); **12)** Fiber Coupled LED :470 nm (Thorlabs cat. no. M470F3); **13)** Fiber Coupled LED: 595 nm (Thorlabs cat. no. M595F2); **14)** LED driver (Thorlabs cat. no. LEDD1B); **15)** Pigtail Rotary Joint, 200 µm, 1.25 Ferrule (Thorlabs cat. no. RJPSL2); **16)** Pigtail Rotary Joint, 400 µm, 2.5 Ferrule (Thorlabs cat. no. RJPSF4); **17)** Data Acquisition (DAQ) System —

NI USB 6259 BNC; **18)** Analysis software [such as FIJI, MATLAB (Mathworks, R2018a), GraphPad Prism].

2.3.2   Preparation for data acquisition

1. For optogenetic stimulation, check LED power and position to ensure consistency across experiments. Point fiber optic LEDs at a 45° angle to illuminate the slice area under the objective. Move the microscope objective to the side to allow for placement of power meter probe incident to the LEDs. Adjust LED power to be 500 µW for the 470-nm fiber-coupled LED (blue) and 100 µW for the 595-nm fiber-coupled LED (amber). The entire setup for optogenetic stimulation and Ca^{2+} imaging is shown in Figure 2-1B.

2. For optogenetic stimulation of the slice, illuminate the field of view using the fiber optic LEDs and sync to image acquisition. An analog trigger signal sent every time an image is acquired is read using a TTL cable connecting the NI-DAQ to the microscope box. The desired stimulation paradigm is programmed in MATLAB using the Data Acquisition Toolbox and synchronized to the confocal acquisition trigger signal on the DAQ. The program uses the DAQ digital output channels to trigger the T- cube LED drivers via a BNC connector according to the stimulation paradigm.

The example recording shown in Figure 2-4C is 12 min long, with the blue LEDs beginning at 100 s into the recording. The blue LED is on for 20 s, followed by a 5 s amber pulse, repeating every 100s. Other recorded paradigms are shown in Figure 2-5.

3. Cut a piece of Kimwipe to fit the bottom of the imaging chamber, fill with enough aCSF to soak it, and position the brain slice in the center of the Kimwipe using an open transfer

pipette. *The Kimwipe beneath the slice creates friction between the harp and the plastic dish needed to minimize slice motion.*

4. With minimal liquid covering the slice, position the tissue restraining harp over the slice to cover the area evenly and avoid folding or wrinkling of the tissue. Once positioned, fill the chamber with enough aCSF to image using the 10× water immersion objective.

2.3.3   Data acquisition

5. While Rhod-2 AM loaded cells are distributed throughout the depth of the slice, astrocytes at the surface of the slice (0 to 20 μm deep) often display a reactive phenotype (visualized as dye aggregates and hypertrophy of primary processes). It is advisable to avoid the superficial layer and select the field of view such that the cells imaged are >20-μm deep into the slice.

6. Acquire an image with the EYFP (astrocytic marker due to Mlc1-ChR2(C128S- EYFP)) and Rhod-2 AM filter sets of the chosen field of view. This image will serve as the reference image during processing to identify astrocytes stained with Rhod-2 AM (refer to step 11).

7. Depending on the stimulation setup protocol selected, the user will need to run the custom-MATLAB script, which waits for a trigger from the microscope to initiate stimulation. This will also serve to synchronize Ca^{2+} imaging with the optogenetic stimulation.

8. Begin time-series data collection for simultaneous optogenetic stimulation and Ca^{2+} imaging on the Olympus Fluoview or equivalent microscope software.

2.3.4 Data processing and analysis

In our experiment, we acquire raw Ca^{2+} imaging data (time series, step 8) and a static image overlap of EYFP and Rhod-2 AM (step 6). After acquisition using the Olympus Fluoview software, or similar acquisition software, the steps for data processing and analysis are given in Figure 2-2. These data processing steps suggested account for common artifacts encountered in single-photon fluorescence (confocal) data acquisition. *The authors would like to mention that the analysis and recording setup employed in this article can be implemented using alternative software like AQuA and Python to quantify astrocytic activity and LabVIEW, or an Arduino for signal synchronization and trigger setup.*

9. Export the raw data to MATLAB for motion correction to improve image registration using (Pnevmatikakis & Giovannucci, 2017)—a piecewise nonrigid motion correction algorithm implemented in MATLAB (step 1, Figure 2-2).

10. Export successfully registered videos as 16-bit Tiff stacks for analysis using FIJI ROI Analyzer (Schindelin et al., 2012). ROI selection is based on the inclusion criteria, as illustrated in Figure 2-4A. A Z project image is generated from the time series, which demarcates active Rhod-2 AM labeled cells with dynamic fluorescence changes (step 2, Figure 2-2). This directs resources to analyze the most active or responsive cells from each slice.
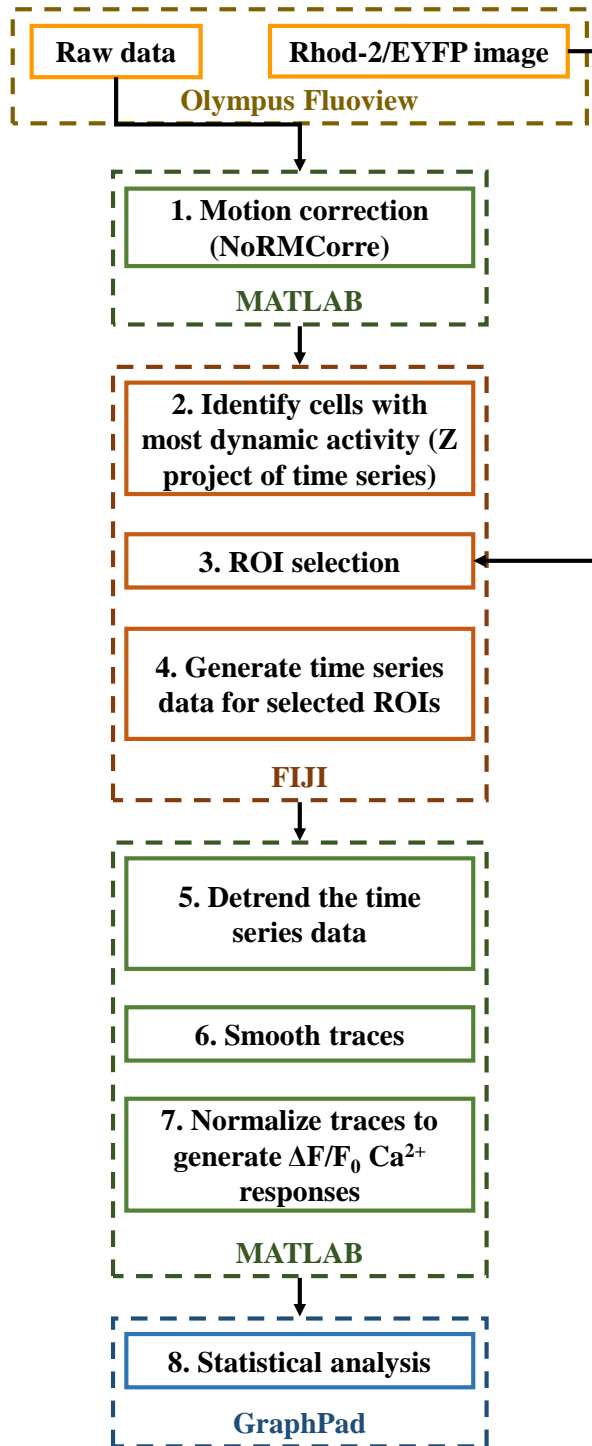
Figure 2-2 Flowchart for processing 1-photon Ca^{2+} imaging data. Suggestive data processing pipeline for Ca^{2+} imaging time-lapse data. After acquiring data using the microscope software (e.g., Olympus Fluoview), the data is motion-corrected in MATLAB, time series plots are generated on FIJI and further detrended, smoothed, and normalized on MATLAB. GraphPad was employed to perform statistical analysis of the data.

31

11. We leverage astrocyte specificity of Mlc1-ChR2-EYFP expression in our model to differentiate astrocytes of interest from other Rhod-2 AM loaded cell types. Cells with explicit somatic Rhod-2 AM loading overlapping with EYFP labeling are chosen for fluorescence signal extraction and further analysis.

12. Using processed data from steps 10 and 11, regions of interest (ROI) encompassing astrocytes for fluorescent signal extraction are manually selected using the ROI manager (step 3, Figure 2-2). The time-series data for the selected ROIs are generated on FIJI (step 4, Figure 2-2) and saved as an Excel file.

13. Detrend the fluorescence time-series data from selected ROIs to correct for the effect of fluorophore bleaching on the baseline of traces in MATLAB (step 5, Figure 2-2).

14. Smooth the traces using a gaussian filter to remove imaging artifacts (step 6, Figure 2-2).

15. Finally, normalize and visualize traces as a percentage of $\Delta F/F_0$, where baseline fluorescence (F_0) is taken to be the median fluorescence intensity of the pre-stimulus imaging window (step 7, Figure 2-2).

16. Run statistical analysis using GraphPad Prism version 8.4.3 (step 8, Figure 2-2). E.g., for the dataset in Figure 2-4, we confirm the normal distribution of the data using the Shapiro-Wilkins test, following which we perform a one-way ANOVA and Dunnett's T3 multiple comparisons test with significance declared at $p < 0.05$. For figures 2-5 to 2-11, we confirm the normality of the distribution, and accordingly run either a 1-way ANOVA or Kruskal Wallis test with suitable multiple comparisons tests. We present summary data as mean ±

std and do not exclude any experimental data points. The sample size is defined as the number of mice, the number of slices, or the number of cells, mentioned in each figure legend.

2.4 COMMENTARY

2.4.1 Critical Parameters and Troubleshooting

Several steps in our optimized protocol, including holding temperatures, incubation, and vibratome slicing parameters, were determined by assessing the health of the brain slices. A robust methodology employed by Buskila *et al.* (Buskila et al., 2014), was used to co-stain DAPI, the nuclear stain, and propidium iodide (PI), a marker for identification of dead cells, thereby giving us an estimate of live/dead cells (Figure 2-3B). Table 2-2 highlights several challenges that one might encounter during the experiments, along with possible causes and solutions.

2.4.2 Time considerations

The outlined protocol typically takes about 11 hours from the preparation of solutions until the end of imaging for 6-7 brain slices (12-min recordings). Pluronic should be warmed in the water bath (34°C) at the beginning of the experiment so that it completely dissolves and is ready for dye preparation. After about 2 hours of warming in the water bath, Pluronic and Kolliphor EL need to be sonicated for 1-2 hours. The dye mixture comprising of Rhod-2 AM, Pluronic, and Kolliphor EL must be prepared immediately post sectioning while the slices are incubated at 34°C, to allow adequate time for sonication. Calibration of LED power to ensure consistency between experiments can be done during the staining step.

2.5 RESULTS AND DISCUSSION

These protocols enable the generation of viable adult cortical murine brain slices stained with Rhod-2 AM, suitable for simultaneous optogenetic stimulation and Ca^{2+} imaging experiments. The experimenter can expect to have about 8-10 brain slices with a thickness of 350 μm from an adult mouse. The viability of the slices generally deteriorates about 6-7 hours after decapitation.

2.5.1 Quantification of loading, spontaneous and evoked Ca^{2+} responses

Cell counts of Rhod-2 loaded astrocytes and cellular viability in the Mlc1-ChR2(C128S)-EYFP transgenic mice slices are shown in Figure 2-3. The overlap between ChR2(C128S)-EYFP and Rhod-2 AM channels is used to determine astrocytes loaded with Rhod-2 AM to subsequently study Ca^{2+} responses (Figure 2-3A, n = 8 mice, 10 slices). Approximately half of all Rhod-2 AM loaded cells are astrocytes expressing the optogenetic construct (right panel), as per the inclusion criteria delineated in Figure 2-4A. We report this yield in the neocortex as an average of percentages across slices. Cellular viability is roughly 55%, quantified as the number of DAPI cells only. Those which have also taken up PI, indicating membrane permeability and cell death, are expressed as percentages (Figure 2-3B, n = 2 mice, 4 slices). This yield was achieved at optimized vibratome sectioning and processing steps.

A

Rhod-2 EYFP

B

DAPI PI
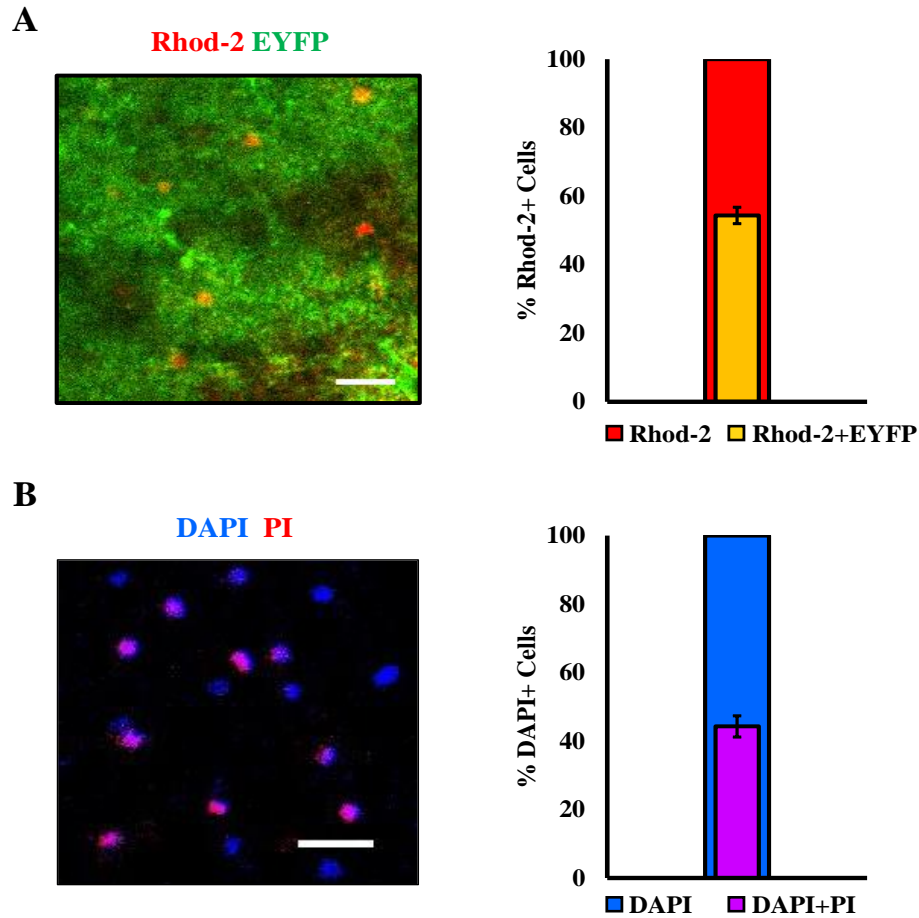
Figure 2-3 Quantification of astrocytic staining and cell viability. (**A**) Left: representative image of a cortical field of view from mice expressing Mlc1-ChR2(C128S)-EYFP (green), showing overlap with Rhod-2 AM staining (red). Right: a fraction of Rhod-2 AM positive cells expressing Mlc1- ChR2(C128S)-EYFP in the neocortex, indicating astrocytes ($n = 8$ mice, 10 sections, mean ± std). (**B**) Left: representative image of Propidium Iodide (PI) stained cells (red) showing overlap with DAPI stained cells (blue). Cells that are positive for DAPI and PI are considered dead. Right: a fraction of DAPI positive cells also stained by PI in the neocortex ($n = 2$ mice, 4 sections, mean ± std). Scale bar – 30 μm.

Time-lapse imaging of Mlc1-ChR2 (C128S)-EYFP mice brain slices loaded with Rhod-2

AM is performed to evaluate astrocytic Ca^{2+} responses (Figure 2-4). A representative image

with examples of cells excluded or analyzed is shown in Figure 2-4A. Refer to steps 11 and

12 of the data processing and analysis section (Basic Protocol 2) for elaboration on the

inclusion/exclusion criteria. Spontaneous Ca^{2+} traces (depicted as $\Delta F/F_0$) demonstrate random transients when no stimulus is applied (Figure 2-4B, n = 5 astrocytes).

A

Rhod-2 EYFP

Excluded   Analyzed

B

$40\% \Delta F/F_0$

50s
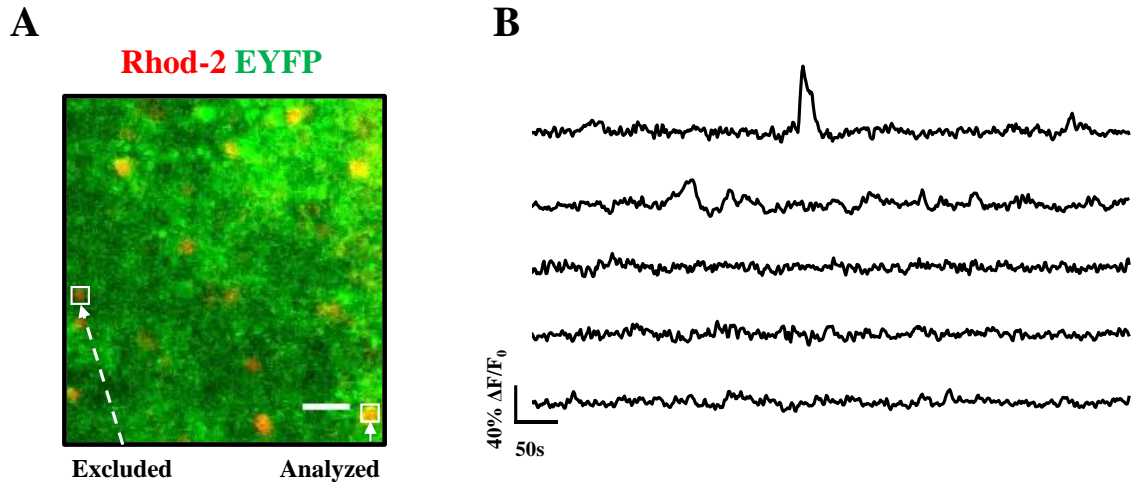
Figure 2-4 Spontaneous Rhod-2 AM Ca^{2+} responses from murine cortical astrocytes. (**A**) Representative image of a cortical section from mice expressing Mlc1- ChR2(C128S)-EYFP (green), showing overlap with Rhod-2 AM (red). Examples of an analyzed astrocyte (Rhod-2 AM[+]/Mlc1-ChR2(C128S)-EYFP[+]) and excluded cell (only Rhod-2 AM[+]) are bound by white boxes. (**B**) Representative $\Delta F/F_0$ traces of spontaneous calcium responses from cortical astrocytes expressing Mlc1-ChR2(C128S)-EYFP.
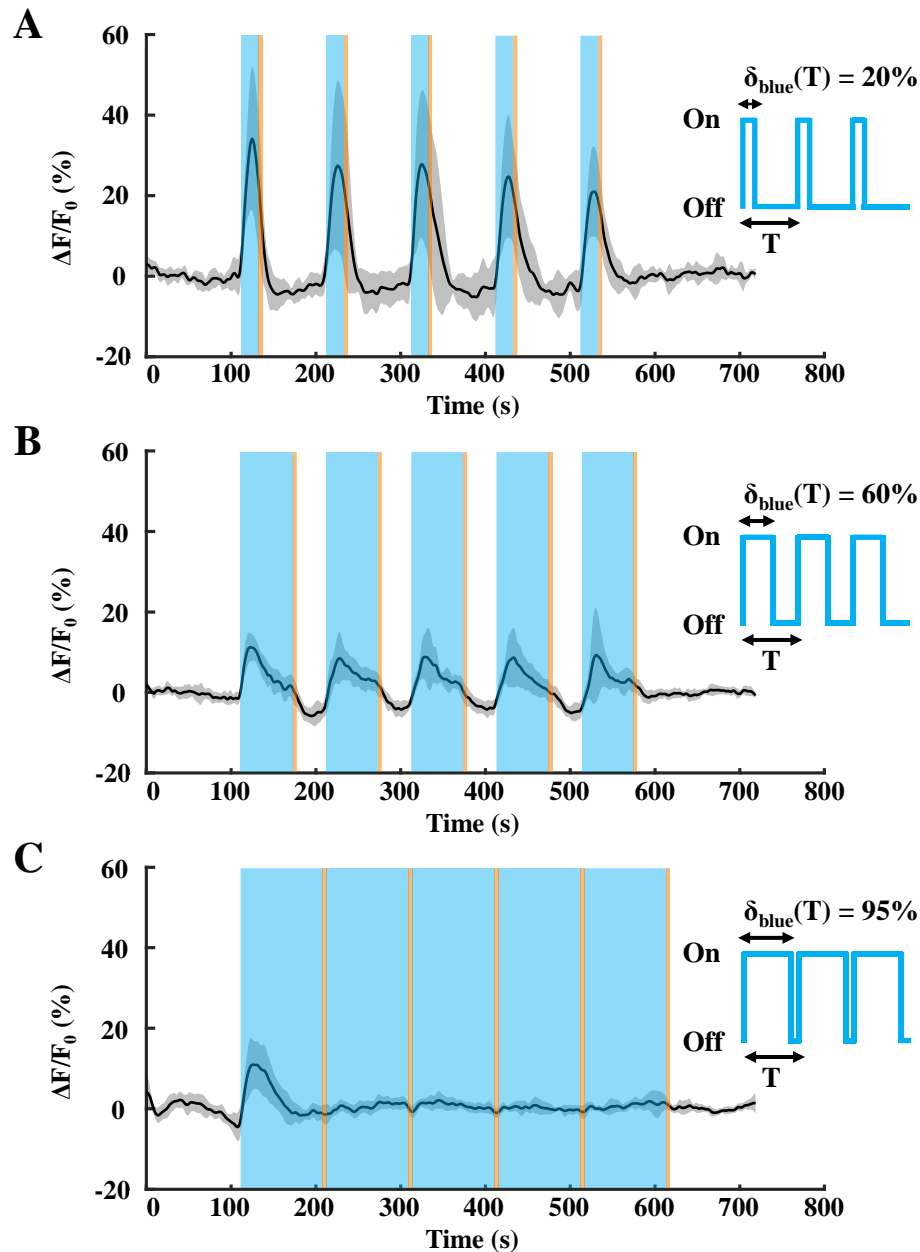
Figure 2-5 Light-evoked Rhod-2 AM Ca²⁺ responses from adult murine cortical astrocytes subjected to various light stimulation paradigms. (**A**) Average $\Delta F/F_0$ trace (central dark trace) of calcium responses from cortical astrocytes expressing Mlc1-ChR2(C128S)-EYFP (n =14 cells, 3 slices, 3 mice) upon repeated light stimulation over the recording period, grey shaded region depicts the standard deviation. Light stimuli: Blue-20s/500 μW (i.e., $\delta_{blue}(T) = 20\%$ where T = 100s) and Amber-5s/100 μW pulses were produced using LED light sources to open and close ChR2(C128S) channels, respectively (denoted as shaded blue and amber colored regions). (**B**) Average $\Delta F/F_0$ trace of astrocytes, n =10 cells, 3 slices, 3 mice. Light stimuli: Blue-60s/500 μW (i.e., $\delta_{blue}(T) = 60\%$; T = 100s) and Amber-5s/100 μW. (**C**) Average $\Delta F/F_0$ trace of astrocytes, n =11 cells, 3 slices, 3 mice. Light stimuli: Blue-95s/500 μW (i.e., $\delta_{blue}(T) = 95\%$; T = 100s) and Amber-5s/100 μW.
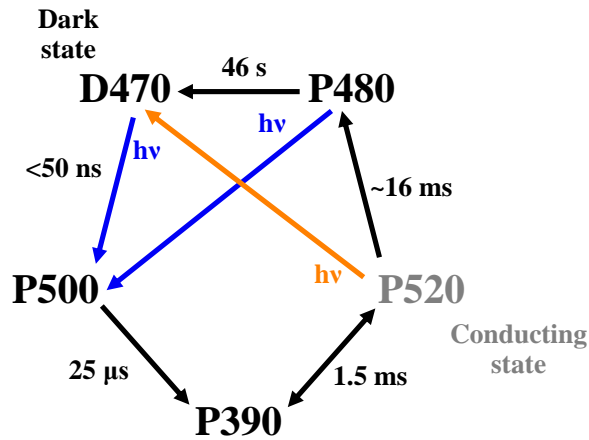
Figure 2-6 Photocycle of ChR2(C128S). Adapted from (A. Berndt et al., 2009; Ritter, Stehfest, Berndt, Hegemann, & Bartl, 2008) with corresponding time conversions.

2.5.2   Response of astrocytic Ca^{2+} to varying light stimulation

Figure 2-5 shows the light-evoked response of MlC[+]/ Rhod-2 AM[+] astrocytes subjected to differing light paradigms. The blue light stimulation paradigms were chosen to be a fraction of the paradigm period (T = 100s), 20%, 60%, and 95%, and five stimulations of each paradigm were incident on the brain slices. Each of these blue light stimulations was followed by a 5s amber pulse (5% of T). While repeated light stimulation of 20% and 60% (Figure 2-5A and B) elicited robust Ca^{2+} responses in these neocortical astrocytes, the 95% paradigm led to only one Ca^{2+} elevation (Figure 2-5C) followed by minimal to no response during the subsequent stimulations.

It is important to note three aspects of these Ca^{2+} responses - firstly, all Ca^{2+} responses tend to initially increase with light stimulation due to cytosolic Ca^{2+} influx via ChR2, and with time, start decreasing. This can be attributed to the bell-shaped response of the IP_3R to cytosolic Ca^{2+}, where an influx of Ca^{2+} into the astrocytic cytosol leads to translocation of

Ca^{2+} from the ER to cytosol, but subsequently, at higher cytosolic concentrations leads to inhibition of the IP_3R, resulting in no subsequent Ca^{2+} spikes (Mak & Foskett, 2015; Watras & Ehrlich, 1991). Secondly, Ca^{2+} clearing mechanisms via buffer proteins, sarco(endo)plasmic reticulum Ca^{2+}-ATPase (SERCA) and plasma membrane Ca^{2+} ATPase (PMCA) pumps and the Mitochondrial Ca^{2+} Uniporter (MCU) also reduce cytosolic Ca^{2+}. Lastly, it is also important to note that when blue light is on, the short-lived conducting P520 state of ChR2(C128S) exists in equilibrium with the P390 state and could also transition to the P480 and P500 states, which are non-conducting (Figure 2-6) (A. Berndt et al., 2009; Ritter et al., 2008). This could also lead to a reduction of influx of Ca^{2+} into the cytosol via ChR2, despite blue light being on, and in combination with the abovementioned mechanisms may result in lowering the net cytosolic Ca^{2+}.

In the case of 95%, it is interesting to note that after the first blue-amber stimulation, there are no major Ca^{2+} elevations during the subsequent stimulations (Figure 2-5C). There appears to be a stealth inactivation of the astrocytes as stimulation is continued, the exact mechanism of which is unknown. In addition to Ca^{2+} clearing cellular mechanisms in the astrocyte, we speculate about the possibility that due to lack of time for achieving the light-sensitive D470 state from P480 (~46s), as there is no dark phase throughout the stimulation (due to 95s of blue followed by 5s of amber), ChR2(C128S) could exist in the non-conducting states, thereby maintaining its Ca^{2+} levels comparable to pre-stimulation (Figures 2-5C and 2-6). Whether this inactivation can be overcome by introducing a rest period of a few minutes between each 95% stimulation is yet to be explored, which would require an increase in recording times. Interestingly, in neurons, upon stimulation (~20

seconds), the photocurrent through the channel seemed to remain constantly high (A. Berndt et al., 2009); however, whether this is maintained at higher stimulation durations (i.e., ~60s and 95s) is to be investigated. The complete characterization of the ChR2(C128S) parameters is also pending theoretical modeling and verification in astrocytes.
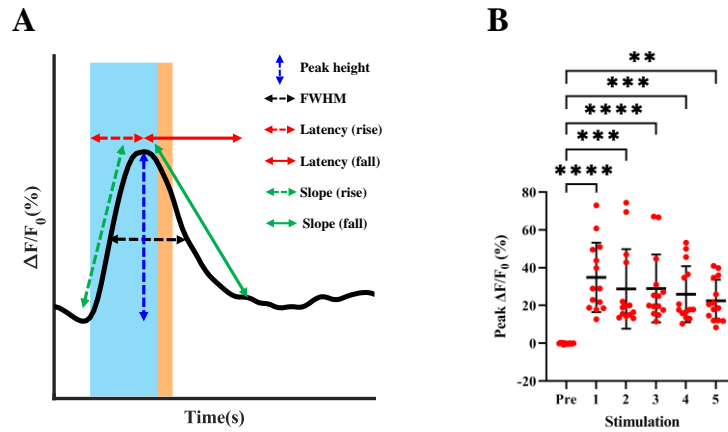
Figure 2-7 Parameter quantification from acute brain slices subjected to blue stimulation (20%). Blue ($\delta_{blue}(T) = 20\%$; T = 100s) and amber-5s/100 µW pulses (corresponding to Figure 2-5A). **(A)** Illustration of parameters quantified from astrocyte peak responses – peak height $\Delta F/F_0$, FWHM, latency, and slopes of rise and fall. **(B)** $\Delta F/F_0$ of the pre-stimulation period along with maximum $\Delta F/F_0$ astrocytic responses during each blue light stimulation window. Average data represented as mean ± std. (* $p \leq 0.05$; ** $p \leq 0.01$; *** $p \leq 0.001$; **** $p \leq 0.0001$).
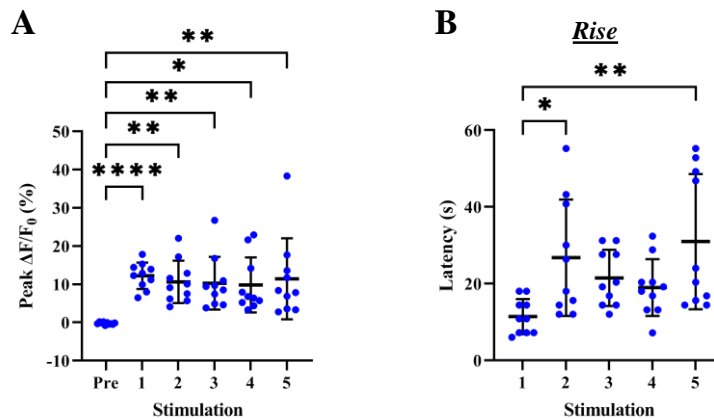
Figure 2-8 Scatter plot of parameter quantification of brain slices subjected to repeated blue stimulation (60%). Blue ($\delta_{blue}(T) = 60\%$; T = 100s) and amber-5s/100 μW pulses (corresponding to Figure 2-5B). (**A**) $\Delta F/F_0$ of the pre-stimulation period along with maximum $\Delta F/F_0$ astrocytic responses during each blue light stimulation window. Average data represented as mean ± std. (**B**) Latency (Rise) (* $p \leq 0.05$; ** $p \leq 0.01$; *** $p \leq 0.001$; **** $p \leq 0.0001$).
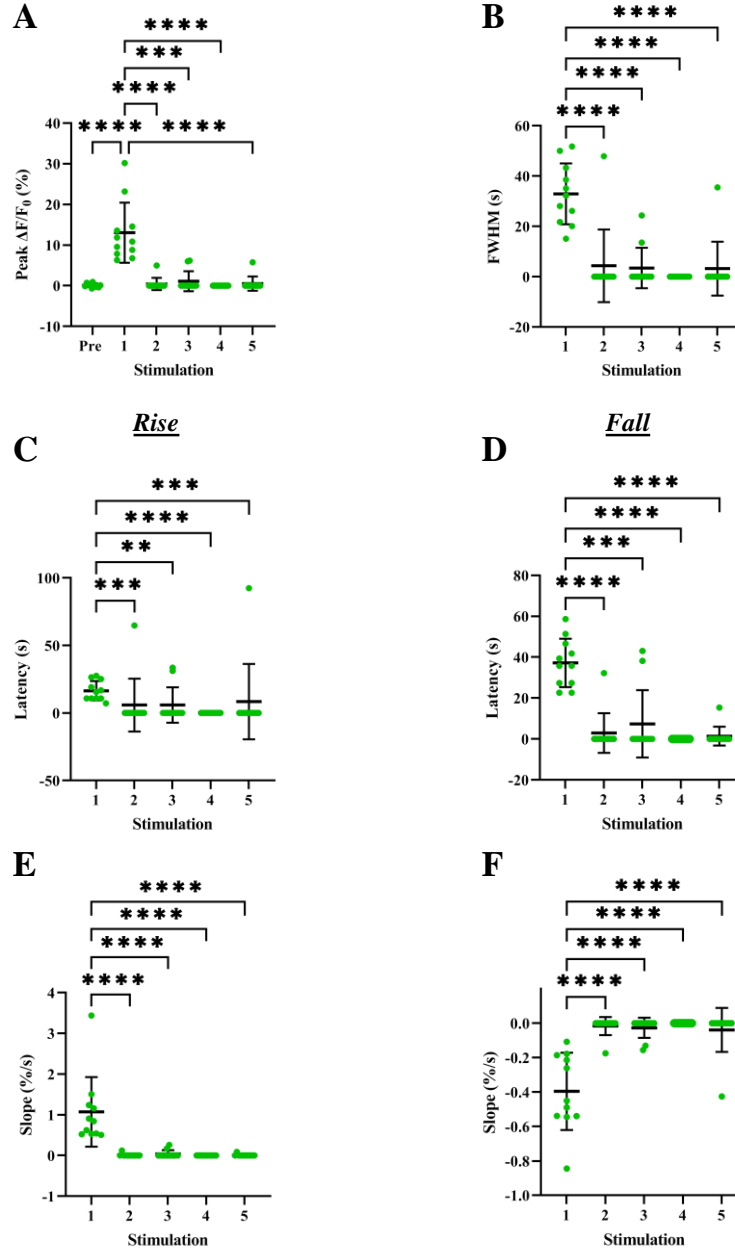
Figure 2-9 Scatter plot of parameter quantification of brain slices subjected to repeated blue stimulation (95%). Blue ($\delta_{blue}(T) = 95\%$; T = 100s) and amber-5s/100 μW pulses (corresponding to Figure 2-5C). (**A**) $\Delta F/F_0$ of the pre-stimulation period along with maximum $\Delta F/F_0$ astrocytic responses during each blue light stimulation window. Average data represented as mean ± std. (**B**) FWHM quantification (**C**) Latency

(Rise) (**D**) Latency (Fall) (**E**) Slope (Rise) (**F**) Slope (Fall) (* $p \leq 0.05$; ** $p \leq 0.01$; *** $p \leq 0.001$; **** $p \leq 0.0001$).

2.5.3 Effect of repeated 20% and 60% stimulation on astrocytes

Figure 2-7A illustrates the parameter quantification performed for the subsequent sections. They are: a) Peak height ($\Delta F/F_0$) within a stimulation paradigm, b) full-width half maximum (FWHM), c) latency rise (time taken from the onset of stimulation until peak height is achieved), d) slope rise, e) latency fall (time taken from peak height until Ca^{2+} basal level, matching pre-stimulation level is achieved) f) slope fall. Figure 2-7B shows the variation in peak heights upon repeated stimulation of astrocytes using $\delta_{blue}(T) = 20\%$; $T = 100s$. Peak $\Delta F/F_0$ during each stimulation (1-5) was significantly higher than during pre-stimulation. Parameters including FWHM, latency (rise and fall), and slopes (rise and fall) were not statistically significant among stimulations. Figure 2-8A shows that astrocytes upon being subjected to multiple stimulation cycles of $\delta_{blue}(T) = 60\%$; $T = 100s$, the peak $\Delta F/F_0$ during each stimulation were significantly higher than during the pre-stimulation period. The latency of the first peak (Figure 2-8B) was significant with respect to the 2nd and 5th stimulations, while all other parameters saw variations that were not statistically significant.

2.5.4 Effect of repeated 95% stimulation on astrocytes

Multiple stimulation cycles of $\delta_{blue}(T) = 95\%$; $T = 100s$ led to drastic and irreversible changes in astrocytic Ca^{2+} recorded during the given time frame (Figure 2-9). While the first stimulation led to a significant increase in peak $\Delta F/F_0$ (Figure 2-9A), there were little to no responses from the astrocytes during the subsequent stimulations (Figure 2-5C). As mentioned in the previous section, we speculate that due to prolonged light stimulation,

ChR2(C128S) is driven towards its non-conducting states, and coupled with the inhibition of the IP$_3$R, the buffering, SERCA, PMCA pumps, and MCU, there is a net reduction in cytosolic Ca^{2+} beyond a point of time. The lack of a prolonged dark phase prevents ChR2(C128S) from returning to its D470 state, which is photosensitive and could progress to the conducting state, resulting in the lack of robust responses in stimulations 2-5.
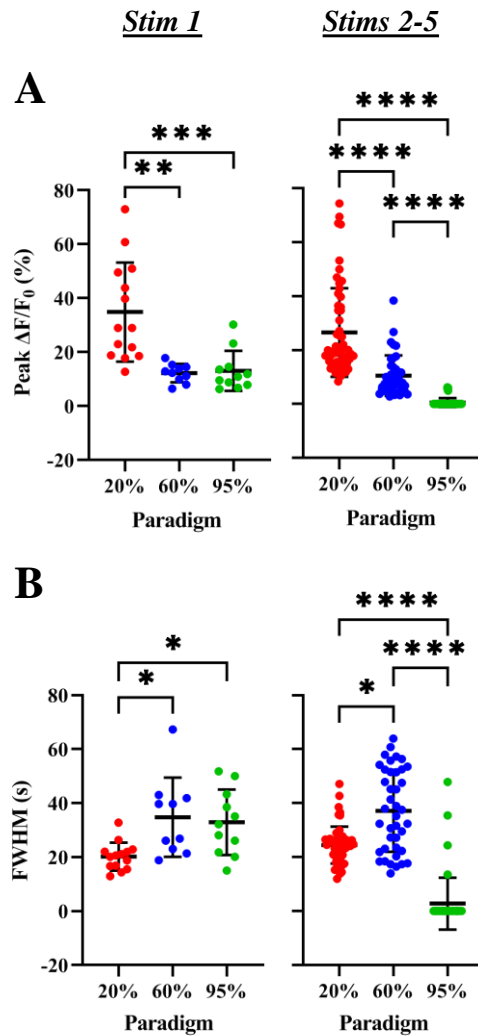
Figure 2-10 Scatter plot comparing the effects of all three light stimulation paradigms on astrocytic Ca^{2+} (Peak height and FWHM). (**A**) Comparison of peak heights and (**B**) FWHM across stimulation paradigms (20%, 60%, and 95%) and across the number of stimulations (Stims 1, 2-5). Average data represented as mean ± std (* p≤ 0.05; ** p≤ 0.01; *** p≤ 0.001; **** p≤ 0.0001).

2.5.5   Quantification of peak characteristics across paradigms

A comparison across light stimulation paradigms helps us understand the trends associated with progressing from a lower (20%) to a higher stimulation paradigm (95%). The peak height (of $\Delta F/F_0$) has a declining trend from the 20% to 60% and 95% paradigm across all the stimulations (Figure 2-10A). Especially in stimulation 1, the peak height achieved due to 20% is higher than in 60% and 95%. No significant differences between 60% and 95% could indicate despite the higher duration of stimulation, no further increases in peaks occurred suggestive of possible ChR2 influx saturation due to the channel residing in non-conductive states, as discussed in the above sections. With subsequent stimulations 2-5, there is a sharp declining trend from 20% to 60% and further down to 95%, as 95% hardly had any peaks past stimulation 1.

Figure 2-10B shows the FWHM quantification across paradigms and stimulations. While stimulation 1 shows a significantly lower FWHM in 20% as compared to the other paradigms, however, interestingly, there is no difference between 60% and 95%. This indicates that despite an increase in blue light stimulation from 60% to 95%, astrocytic Ca^{2+} levels return to baseline, and the Ca^{2+} response overall has a similar duration. Stimulations 2-5 (Figure 2-10B) lead to a bell-shaped trend, with an increase in FWHM from 20% to 60%, and a decrease at 95%, due to lack of Ca^{2+} responses in subsequent stimulations of 95%.
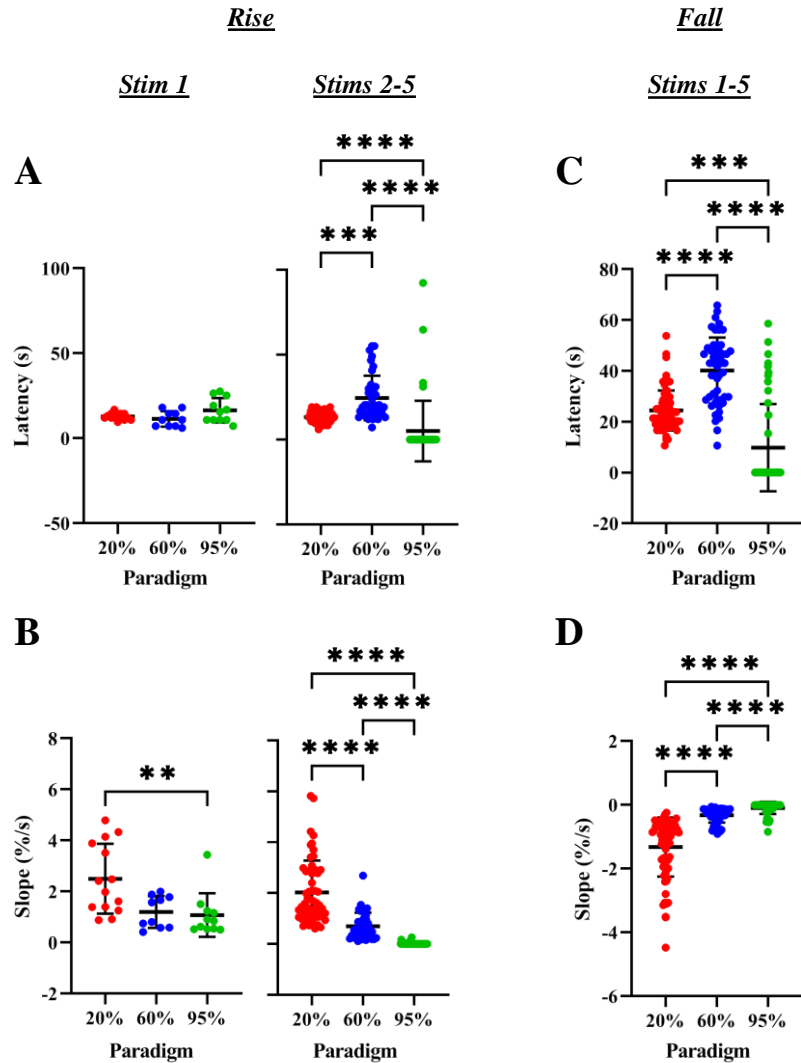
Figure 2-11 Scatter plot comparing the effects of all three light stimulation paradigms on increasing astrocytic Ca^{2+} (Latency and Slope). (**A**) Comparison of latency (rise), (**B**) slopes (rise), (**C**) latency (fall) and (**D**) slopes (fall) across stimulation paradigms (20%, 60% and 95%), and across number of stimulations (Stims 1-5). Average data represented as mean ± std (* p≤ 0.05; ** p≤ 0.01; *** p≤ 0.001; **** p≤ 0.0001).

2.5.6   Quantification of latency and slope across paradigms

Quantification of the latency and slopes (rise and fall) displays interesting trends compared to paradigms and repeated stimulations (Figure 2-11). With the quantification of rise parameters, the latency was similar in all three paradigms for the first stimulation, while

the subsequent stimulations saw a bell-shaped trend, with an increase from 20% to 60%, further leading to a decline for 95%. (Figure 2-11A). However, the slopes had a declining trend across paradigms, across all stimulations (Figure 2-11B). Together, these indicate that for stimulation 1, there was a quicker achievement and higher magnitude of peak $\Delta F/F_0$ (slope) for the 20% paradigm, while the slopes were similar for 60% and 95%.

For stimulations 2-5, there was an increase in latency periods (Figure 2-11A) from 20% to 60%, indicating longer durations to achieve peak $\Delta F/F_0$, and possibly lower levels of $\Delta F/F_0$, as seen in the declining trend of the slope graphs (Figure 2-11B).

Like the rise parameters, the quantification of the latency and slopes of fall were performed to compare the responses of the different paradigms and across stimulations. The fall latency time shows a bell-shaped trend while increasing from 20% to 60% (possibly due to gradual buildup of Ca^{2+} due to prolonged light stimulation) and further decline to 95% due to lack of Ca^{2+} spikes. (Figure 2-11C). The slopes of 20% were much steeper than 60% and 95%, showing a declining trend across paradigms, across all stimulations (Figure 2-11D).

2.6   CONCLUSION

In this chapter, we devised a protocol to perform simultaneous optogenetic stimulation and Ca^{2+} imaging and identified light stimulation paradigms conducive for eliciting on-demand astrocytic responses on live adult murine brain slices (2-5 months). We overcome major challenges by 1) minimizing the accelerated deterioration of *in situ* slice health when using an adult animal for Ca^{2+} imaging, 2) devising the protocol for using Rhod-2AM to prevent

the overlap between ChR2 and Ca^{2+} indicator related to simultaneous optogenetic stimulation and Ca^{2+} imaging and 3) identifying light stimulation paradigms leading to robust astrocytic Ca^{2+} increases in short-term stimulation.

The protocol encompassed details for experimental preparation, brain tissue processing, Rhod-2 AM loading specifics, maintenance of slice health, and Ca^{2+} imaging during light stimulation and was applied successfully to optogenetically control adult neocortical astrocytes. We identified paradigms 20% and 60% (of T=100s) to elicit robust Ca^{2+} responses upon multiple stimulations, while the 95% paradigm exhibited a response only during the first stimulation. We quantified several parameters, including peak height, FWHM, and latencies, and observe that the 20% paradigm has the highest peak $\Delta F/F_0$ among the paradigms across all stimulations and the lowest FWHM during the first stimulation. Overall, the 20% paradigm is a favorable choice for eliciting robust astrocytic Ca^{2+} responses in astrocytes while performing multiple stimulations, followed by 60%, although with lesser $\Delta F/F_0$. Paradigms 60% and 95% had comparable responses (peak height, FWHM, and latency) during the first light stimulation and could be employed for experiments requiring a single stimulation.

Table 2-1 Recipe for ice-cold cutting solution and aCSF[a,b].

Reagent	Cutting Solution (mM)	aCSF (mM)
Sucrose (Fisher Scientific, cat # S25590)	110	-
Glucose (Fisher Scientific, cat # BP350-1)	5	10
Sodium Chloride (Fisher Scientific, cat # S271)	60	124
Sodium Phosphate, Monobasic (Ward's Science, cat #470302-666)	1.25	1.25
Potassium Chloride (Fisher Scientific cat # BP366)	3	5
Sodium Bicarbonate (Fisher Scientific, cat # S233)	28	22
Calcium Chloride Dihydrate (Fisher Scientific, cat # C70)	0.5	2
Sodium Ascorbate (Fisher Scientific, cat # AC352681000)	0.6	-
Magnesium Sulphate Heptahydrate (Fisher Scientific cat # M63)	-	2

[a] Solutions are prepared in DI water

[b] Solutions are recommended to be made fresh on the day of the experiment to avoid bacterial contamination.

Table 2-2 Troubleshooting critical parameters during the experiment.

Problem	Possible cause	Solution
Compression of the mounted brain during sectioning or lack of intact sections	Effect of incorrect: 1. amplitude	1. Sectioning at very low amplitude (below 1.2 mm) causes compression of the brain tissue, while at a very high amplitude (2 mm) leads to the shearing of the tissue.
	2. speed of the vibratome	2. Sectioning at a higher speed (greater than 0.4 mm/sec) leads to compromised tissue integrity and very low cell viability. At lower speeds (lesser than 0.2 mm/sec), sectioning of the brain is challenging.

The amplitude and speed used for sectioning in this study were 1.6 mm and 0.3 mm/sec, corresponding to settings 8 and 1.5 on the Vibratome 1000 Plus, respectively.

Problem	Possible cause	Solution
Dye aggregates in the slice visualized during imaging	Lack of sonication and filtration of the dye during preparation	Filter the dye mixture and sonicate for a minimum of 20 minutes before adding to the brain slices.
Improper function of the vibratome head/ motor	Water leak to the inner base of the vibratome	Seal the back of the vibratome chamber using paper towels to absorb excess water while sectioning, preventing solution leak.
The rapid deterioration of health of brain slices (within 6 hours of sectioning), reflected as a bad Rhod-2 AM signal-to-noise ratio while imaging	1. Stoppage of bubbling during the experiment	1. Rigorous monitoring of bubbling during various steps is imperative for continuous buffering of HCO_3^- present in the aCSF. This avoids drastic changes in pH (Outside the 7.3-7.4 range).
	2. Lack of fresh Pluronic/ Kolliphor EL	2. Make fresh Pluronic and Kolliphor EL once a month.
	3. The pH of solution turning extremely acidic/ basic (outside the desired 7.3-7.4 range)	3. Recheck the pH of the solutions periodically during the experiment.
	4. Buildup of toxins	4. Holding in a large beaker after de-esterification keeps slices healthier, making them last longer. Avoid using a 6-well plate for holding.
	5. Incorrect DMSO/ Pluronic concentrations	5. Usage of recommended DMSO and Pluronic concentrations (Hamad, Krause, & Wahle, 2015).

	6. Increased temperature of the water bath	6. Maintain the water bath at 34˚C.
Repeated issues with staining, visualized as cells being too bright or too dim (unloaded)	An issue with a specific lot number of the dye	Order a fresh batch of dye.

CHAPTER 3   UNRAVELING CHR2-DRIVEN STOCHASTIC CA^{2+} DYNAMICS IN ASTROCYTES

The content of this chapter is published in PLOS Computational Biology as Arash Moshkforoush*, Lakshmini Balachandar*, Carolina Moncion*, Karla A. Montejo, and Jorge Riera Diaz (*equal author contribution). "Unraveling ChR2-driven stochastic Ca^{2+} dynamics in astrocytes: A call for new interventional paradigms" (Moshkforoush, Balachandar, Moncion, Montejo, & Riera, 2021).

3.1   INTRODUCTION

The role of astrocytic calcium signaling in various regulatory mechanisms in the brain is far from being fully understood and is a subject of considerable controversy [see refs (A. Araque et al., 2014; Bazargani & Attwell, 2016; Todd A Fiacco & McCarthy, 2018; Iadecola, 2017; Savtchouk & Volterra, 2018; Andrea Volterra et al., 2014)]. These are fueled in part by the limited *in vivo* reproducibility of *in vitro*/*in situ* experimental observations (Filosa, Morrison, Iddings, Du, & Kim, 2016; Machler et al., 2016; Magistretti & Allaman, 2018; Rosenegger & Gordon, 2015), as well as a dearth of cell-specific protocols to induce astrocytic Ca^{2+} signaling *in vivo* in order to delineate their role from ongoing neuronal activity. Sensory and transcranial direct current stimulation techniques (Monai & Hirase, 2016; Monai et al., 2016; Stobart et al., 2018) have been used to elicit Ca^{2+} changes in astrocytes. However, these methods lack cell specificity due to the concurrent activation of other cell types, including neurons. Studies have also modulated astrocytic Ca^{2+} activity *in vivo* using cell-specific techniques including Ca^{2+} uncaging (Chen et al., 2013; Takano et al., 2006), chemogenetics (Bonder & McCarthy, 2014;

Durkee et al., 2019) and optogenetics (Masamoto et al., 2015; Takata et al., 2018). Ca^{2+} uncaging requires invasive site-specific delivery of calcium vehicles, which are rendered inoperative upon depletion via photolysis. Chemogenetics, e.g., designer receptor exclusively activated by designer drugs (DREADDS), offers a platform for controlled, targeted drug delivery; however, they suffer from low temporal resolution. Contrarily, optogenetics is an avant-garde, minimally invasive, and reproducible approach (Adamantidis et al., 2014; Fenno et al., 2011), providing a platform to genetically target specific cell types with high temporal and spatial precision, which can be employed as a tool to exclusively modulate astrocytic Ca^{2+} signaling *in vivo*.

Despite the recent inception of the field of optogenetics, a wide variety of optogenetic tools have been constructed, among which ChR2 has been one of the most commonly used. More recently, several ChR2 variants have been engineered for enhanced channel conductance (ChETA) (Gunaydin et al., 2010), increased calcium permeability (CaTCh) (Kleinlogel et al., 2011), and faster recovery kinetics (ChRET/TC) (André Berndt et al., 2011). Contrary to neurons, a holistic approach to quantify the effect of light stimulation on astrocytes has not yet been formulated. Given that light activation of ChR2-enabled astrocytes alters dynamics of intracellular ionic species, mathematical modeling can be of importance in predicting how laser specifications, as well as the biophysical properties of the ChR2 construct, can affect astrocytic calcium signaling. Available theoretical models of Ca^{2+} dynamics in astrocytes primarily rely on elevating intracellular IP_3 levels to initiate a Ca^{2+} response from the intracellular stores and have not evaluated the effect of direct influx of these ions through transmembrane channels, e.g. ChR2. To achieve predictions with high

accuracy, it is also imperative that the model accounts for the stochastic nature of spontaneous calcium oscillations in these cells, which result from the random opening of the IP$_3$R channels in clusters. Such a model can guide experimentalists in optimizing light stimulation paradigms for existing optogenetic variants to achieve desired Ca^{2+} levels in astrocytes, as well as aid in the development of novel application-based constructs targeting these cells.

To this end, we outline a novel stochastic model of astrocytic calcium dynamics with an incorporated optogenetic component—ChR2. Firstly, we quantify and evaluate the effect of different light stimulation paradigms on the Ca^{2+} dynamics of single cells expressing three existing ChR2 variants i.e. wild type (WT), ChETA, and ChRET/TC. For the WT variant, we use the two channel characterizations provided in ref. (Stefanescu, Shivakeshavan, Khargonekar, & Talathi, 2013), namely WT$_1$ and WT$_2$. Using the model, we analyze the effect of light stimulation in astrocytes congruent with experimental recording durations (in the order of tens of minutes) (Balachandar et al., 2020; A. Skupin, Kettenmann, & Falcke, 2010; Alexander Skupin et al., 2008), and also gauge the potential effect of long-term optogenetic stimulation (in the order of several hours or beyond) in these cells. Secondly, we quantify the effect of varying stimulation light intensities on a ChR2-incorporated astrocyte with respect to its spiking rate and basal level. Thirdly, to identify key features necessary for the development of prospective ChR2 constructs, we perform a global sensitivity analysis of different parameters of the single cell model to the model output. Lastly, through the incorporation of gap junctions allowing for the diffusion of IP$_3$ and Ca^{2+}, we analyze the effect of local light stimulation on the global Ca^{2+} response

in a network of astrocytes expressing ChR2, and also characterize effects of varying ChR2 expression.

3.2 MATERIALS AND METHODS

The biophysical model outlined in Figure 3-1 consists of our previously developed model of astrocytic calcium dynamics (J. Riera, Hatanaka, Ozaki, & Kawashima, 2011; J. Riera, Hatanaka, Uchida, et al., 2011), based on the Li-Rinzel simplification of the De Young-Keizer model (De Young & Keizer, 1992; Li & Rinzel, 1994), and a 4-state model of ChR2 photocurrent kinetics adapted from refs. (Stefanescu et al., 2013; J. C. Williams et al., 2013). We incorporated a 4-state model of ChR2 photocycle, as previous studies have demonstrated its superiority in capturing the dynamics of the ChR2 photocurrent compared to 3-state models (Nikolic et al., 2009; Stefanescu et al., 2013). The ChR2 model assumes two sets of intra-transitional closed/open states, i.e., dark-adapted (c_1 and o_1) and light-adapted (c_2 and o_2), in describing the dynamics of a ChR2 photocycle. Light stimulation window ($S_0(t)$) is modeled as a pulsed train with unit amplitude and is characterized by a period (T) and a pulse width (δ) (expressed as a percentage of T), indicating the duration within the pulse period for which the light is on.

The model incorporates Ca^{2+} influx from the extracellular space through a light-evoked ChR2 flux (J_{ChR2}), a capacitive calcium entry (CCE) flux via store-operated Ca^{2+} channels (SOC) (J_{CCE}), and a leak flux representing other transmembrane Ca^{2+} channels and exchangers (J_{in}). It also accounts for the release of Ca^{2+} from the endoplasmic reticulum (ER) into the cytosol through inositol trisphosphate receptors (IP$_3$Rs) (J_{IP_3R}), a form of Ca^{2+}-induced Ca^{2+} release (CICR) process, and a leak flux (J_{Leak}). Replenishment of ER
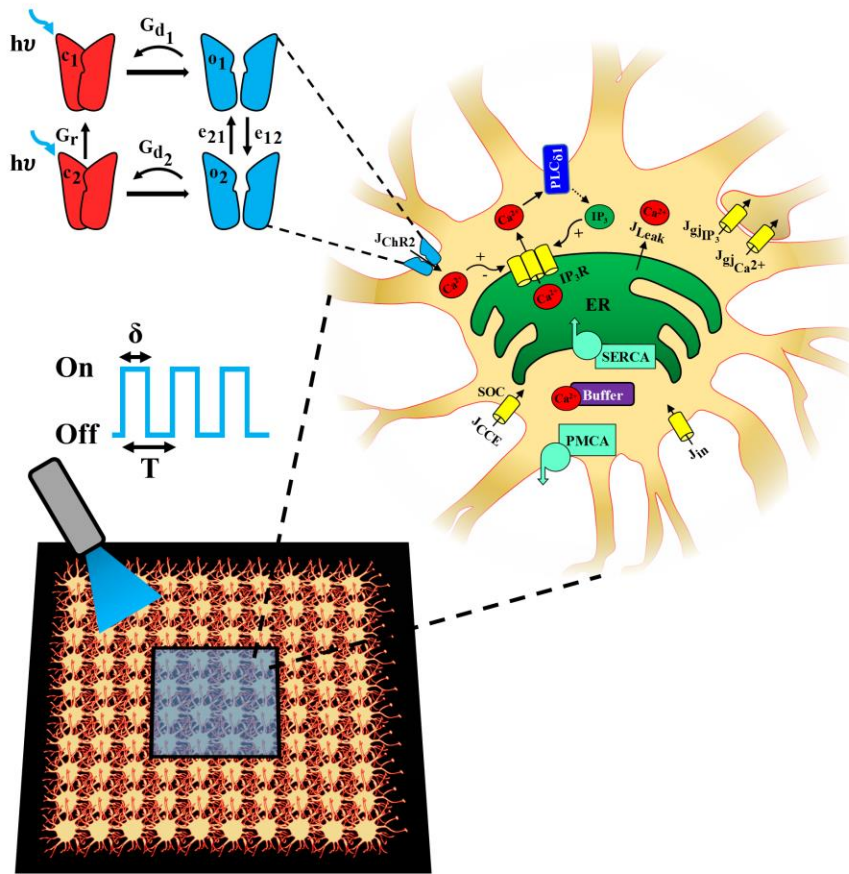
Figure 3-1 Schematic of the biophysical model. A model for a ChR2-expressing astrocyte is presented, accounting for: 1) Ca^{2+} release from the endoplasmic reticulum (ER) into the cytosol via the IP_3R clusters, 2) Phospholipase-C $\delta 1$ ($PLC_{\delta 1}$) mediated production of IP_3, 3) capacitive calcium entry (CCE) via the store operated calcium channel (SOC), 4) passive leak from the ER to the cytosol (J_{leak}), 5) replenishment of ER stores via sarco(endo)plasmic reticulum Ca^{2+}-ATPase (SERCA) pump, 6) extrusion of Ca^{2+} by plasma membrane Ca^{2+} ATPase (PMCA) pump into the extracellular (EC) space, 7) passive leak (J_{in}) into the cytosol from the EC space, and 8) Ca^{2+} buffering by endogenous buffer proteins. In astrocytic network simulations (bottom panel), each cell is connected to its neighboring cells though Ca^{2+} and IP_3 permeable gap junctions, indicated as $J_{gi_{Ca^{2+}}}$ and $J_{gi_{IP_3}}$, respectively, and a central region (blue shaded box) is stimulated with light. A 4-state model [closed states (c_1 and c_2) in red and open states (o_1 and o_2) in blue] is used to represent ChR2 gating dynamics. The blue light ($\lambda = 470$ nm) stimulation paradigm used to open ChR2, leading to a Ca^{2+} influx (J_{ChR2}), is characterized by pulse period (T) and pulse width (δ).

Ca^{2+} is done via activation of the sarco(endo)plasmic reticulum Ca^{2+}-ATPase (SERCA) pump, while plasma membrane Ca^{2+} ATPase (PMCA) pump extrudes cytosolic Ca^{2+} into the extracellular space. The dynamics of IP_3 concentration in the soma ($[IP_3]$) is included

via Ca^{2+}-dependent activation of the Phospholipase $C_{\delta1}$ ($PLC_{\delta1}$) pathway. Buffering of Ca^{2+} is explicitly accounted for by a fast buffering approximation process (Smith, Wagner, & Keizer, 1996). Intercellular signaling in a network of astrocytes is modeled by incorporation of Ca^{2+} and IP_3 permeable gap junctions between neighboring cells.

3.2.1 Single cell model

The dynamics of a single ChR2-enabled astrocyte can be summarized by the following system of stochastic differential equations (SDEs):

$$d\mathbf{x} = \mathbf{f}(t,\mathbf{x},\mathbf{p})dt + \mathbf{G}(t,\mathbf{x},\mathbf{p})d\boldsymbol{\omega} \tag{1}$$

where $\mathbf{x} = ([Ca^{2+}]_c, [IP_3], h, [C_o], o_1, o_2, c_1, c_2, s)^T$ is the vector of state variables, $[Ca^{2+}]_c$ is the cytosolic calcium concentration, $[C_o]$ is the total Ca^{2+} concentration in the cell, i.e., cytosol and ER, h is the fraction of open inactivation gates of IP_3R channels, and s captures the temporal kinetics of conformational changes of ChR2 following light stimulation. $\mathbf{p}$ denotes the vector of model parameters summarized in Table 3-1. Components of the $\mathbf{f}$ vector, i.e., the drift rate function, contain deterministic equations of the single cell model and are described in detail in later sections. $\mathbf{G}$ is a diagonal matrix of diffusion rate components of the stochastic processes (noise) associated with state variables. The Brownian motion vector is denoted as $d\boldsymbol{\omega}$.

The components of the $\mathbf{G}$ matrix are generally determined by the rate parameters of the deterministic part of the SDE, which lead to a state-dependent multiplicative noise in the system (A. Skupin et al., 2010; Van Kampen, 2007). In calcium dynamics, the source of stochasticity is mainly attributed to the aggregation of a small number of IP_3R channels in

56

clusters, which leads to the formation of intra-cluster Ca^{2+} blips (resulting from random opening of a single IP_3R) or Ca^{2+} puffs and sparks (from the concurrent opening of a large number of IP_3Rs within a cluster). When coupled with other clusters, synchronized Ca^{2+} puffs can originate global Ca^{2+} events in the cell (A. Skupin et al., 2010). Several schemes have been developed to model the stochastic dynamics of IP_3Rs in different cell types, ranging from models incorporating detailed Markov Chain processes, to those adapting Fokker-Planck approximations (or their equivalent Langevin equations) of the Markov approaches [refer to ref. (Sneyd & Falcke, 2005) for a review of the deterministic and stochastic models of IP_3Rs].

In this study, we adopted the Langevin approach outlined in ref. (Shuai & Jung, 2002) for the dynamics of open IP_3R inactivation gates in Eq. 1, where the associated noise is a Gaussian white noise with zero mean and the variance (σ_h^2) depending on the levels of $[Ca^{2+}]_c$, $[IP_3]$, h, and the number of IP_3Rs in a cluster. We have previously estimated the noise level in the equations for $[IP_3]$, $[Ca^{2+}]_c$, and $[C_o]$ in astrocytes as additive, uncorrelated Wiener processes with zero mean and a constant variance (σ_i^2; $i = [Ca_c^{2+}, IP_3, C_o]$) (J. Riera, Hatanaka, Ozaki, et al., 2011) using the local linearization (LL) filter (Ozaki, 1993) (Table 3-1). These processes account for potential sources of stochasticity other than the dynamics of the IP_3R channels. We further assume that the dynamics of ChR2 gating is only deterministic, i.e., $\sigma_{o_1} = \sigma_{o_2} = \sigma_{c_2} = \sigma_s = 0$.

The dynamics of the free cytosolic calcium concentration is given by:

$$d[Ca^{2+}]_c = \left([\lambda(J_{IP_3R} + J_{Leak} - J_{SERCA}) + \varepsilon(J_{in} + J_{CCE} - J_{PMCA} + J_{ChR2})]/(1+\theta)\right)dt +$$

$$\sigma_{Ca_c^{2+}} dw_{Ca_c^{2+}}, \tag{2}$$

where $\theta = b_t K / ([Ca^{2+}]_c + K)^2$ is the buffering factor; b_t is the total buffer protein concentration; and K is the buffer rate constant ratio (Smith et al., 1996).

The efflux of Ca^{2+} from the ER into the cytosol via the IP_3R channel can be described as:

$$J_{IP_3R} = \alpha_1 v_1 m_\infty^3 n_\infty^3 h^3 ([Ca^{2+}]_{ER} - [Ca^{2+}]_c), \tag{2.1}$$

where

$$[Ca^{2+}]_{ER} = \frac{(C_o - [Ca^{2+}]_c)}{\alpha_1} \tag{2.2}$$

$$m_\infty = \frac{[IP_3]}{([IP_3] + d_1)} \tag{2.3}$$

$$n_\infty = \frac{[Ca^{2+}]_c}{([Ca^{2+}]_c + d_5)} \tag{2.4}$$

The leak of Ca^{2+} ions from ER into the cytosol is modeled as:

$$J_{Leak} = v_2 ([Ca^{2+}]_{ER} - [Ca^{2+}]_c) \tag{2.5}$$

A hill-type kinetic model describing the activity of the SERCA pump is given by:

$$J_{SERCA} = V_{SERCA} \frac{([Ca^{2+}]_c)^2}{([Ca^{2+}]_c)^2 + (K_p)^2} \tag{2.6}$$

The flux through SOC channels is described using the following equation:

$$J_{CCE} = \frac{x_{CCE}(h_{CCE})^2}{\left([Ca^{2+}]_{ER}\right)^2 + (h_{CCE})^2} \qquad (2.7)$$

Ca^{2+} extrusion across the PM via PMCA is given by:

$$J_{PMCA} = k_{out}[Ca^{2+}]_c \qquad (2.8)$$

PLC$_{\delta 1}$- mediated IP$_3$ changes in the cell is described as:

$$d[IP_3] = \left(X_{IP_3} + J_{PLC_{\delta 1}} - K_{IP_3}[IP_3]\right) dt + \sigma_{IP_3} dw_{IP_3}, \qquad (3)$$

where X_{IP_3} denotes the basal rate of IP$_3$ production in the cell. PLC$_{\delta 1}$ activity is described with a Hill's kinetic model as:

$$J_{PLC_{\delta 1}} = v_\delta \frac{[Ca^{2+}]_c^2}{[Ca^{2+}]_c^2 + K_{\delta Ca}^2} \qquad (3.1)$$

The dynamics of the fraction of open inactivation IP$_3$R gates is given by:

$$dh = \left[\alpha_h(1-h) - \beta_h h\right]dt + \sigma_h(t,\mathbf{x},\mathbf{p})dw_h, \qquad (4)$$

where the opening (α_h) and closing (β_h) rates are defined as:

$$\alpha_h = \frac{ad_2([IP_3] + d_1)}{[IP_3] + d_3} \qquad (4.1)$$

$$\beta_h = a[Ca^{2+}]_c \qquad (4.2)$$

and

$$\sigma_h^2(t,\mathbf{x},\mathbf{p}) = \left[\alpha_h(1-h) + \beta_h h\right]/N, \qquad (4.3)$$

where N is the number of IP$_3$Rs within a cluster.

The total free Ca^{2+} in the cell is modeled as:

$$dC_o = (\ \varepsilon(J_{in} + J_{CCE} - J_{PMCA} + J_{ChR2})/(1 + \theta)\ )dt + \sigma_{C_o}dw_{C_o}, \tag{5}$$

with a zero-mean Gaussian noise component with a constant variance $\sigma_{C_o}^2$.

The open and closed gating dynamics of ChR2 are given by:

$$do_1 = (p_1sc_1 - (G_{d_1} + e_{12})o_1 + e_{21}o_2)dt + \sigma_{o_1}dw_{o_1} \tag{6}$$

$$do_2 = (p_2sc_2 + e_{12}o_1 - (G_{d_2} + e_{21})o_2)dt + \sigma_{o_2}dw_{o_2} \tag{7}$$

$$dc_2 = (G_{d_2}o_2 - (P_2s + G_r)c_2)dt + \sigma_{c_2}dw_{c_2} \tag{8}$$

$$ds = \left(\frac{(S_0(t) - s)}{\tau_{ChR2}}\right)dt + \sigma_Sdw_S \tag{9}$$

The existence of ChR2 in open and closed states satisfies the following algebraic condition:

$$c_1 + c_2 + o_1 + o_2 = 1 \tag{10}$$

The current generated through ChR2 is given by:

$$I_{ChR2} = A_m\,g_1\,(o_1 + \gamma o_2)G(V_m)(V_m - E_{ChR2}), \tag{11}$$

where $G(V_m)$ is the voltage dependent rectification function determining the shape of ChR2 photocurrent with changing V_m. The resultant flux through ChR2 is then derived as

$$J_{ChR2} = \frac{I_{ChR2}}{Fvol_{cyt} \ z_{Ca^{2+}}} \qquad\qquad (11.1)$$

Although ChR2 is a non-selective cation channel, in this study, we assume that J_{ChR2} is solely a calcium flux, as calcium dynamics is one of the most prominent modes of signaling in astrocytes.

3.2.2   Quantification of astrocytic activity

Throughout this manuscript, we calculated the light-evoked mean spiking rate and basal level of $[Ca^{2+}]_c$ as a measure of astrocytic activity. For spiking rate calculations, we first removed the trend of simulated calcium traces, i.e., ChR2-induced steady rise in the baseline levels as observed in the traces of Figures 3-2 and 3-3. Using a threshold of 0.2 µM, calcium spikes were detected from the baseline-corrected traces and used to compute the mean spiking rate over the entire duration of stimulation. This threshold was chosen to exclude small-amplitude Ca^{2+} fluctuations from the calculation of the mean spiking rate. Light-induced elevations in the Ca^{2+} basal levels were calculated at the end of the stimulation window. These two measures were compared to study the effect of different light stimulation paradigms, i.e., varying combinations of T and δ values, as well as model parameters, on the response of optogenetically stimulated astrocytes.

3.2.3   Sensitivity analysis

A global sensitivity analysis was performed to assess the sensitivity of the single cell model output, i.e., Ca^{2+} spiking rate and basal level, to variations in parameters determining the magnitude of ChR2 photocurrent and those describing the Ca^{2+} buffering kinetics. Each parameter was allowed to vary around its control value within a lower and upper bound

(Table 3-2), and the Latin hypercube sampling (LHS) method with uniform distribution was used to select 1000 random parameter sets to perform the sensitivity analysis (Marino, Hogue, Ray, & Kirschner, 2008; McKay, Beckman, & Conover, 2000). The upper and lower bounds were selected such that the range encompasses reported values of parameters for different variants of ChR2. The single cell model was solved for each parameter set, and the partial rank correlation coefficient (PRCC) for each parameter was then computed to determine the magnitude of the parameter influence (positive or negative) on the desired model output. A 95% confidence interval was chosen to determine if the exerted influence is statistically significant.

3.2.4   Astrocytic network model

To study the network-wide response of astrocytes to light stimulation, we incorporated Ca^{2+} and IP_3 permeable gap junctions between cells in a network of astrocytes. Fluxes:

$$J_{gj_{Ca_i^{2+}}} = \sum_k D_{Ca^{2+}}([Ca^{2+}]_{c_i} - [Ca^{2+}]_{c_k}) \tag{12}$$

$$J_{gj_{IP_{3_i}}} = \sum_k D_{IP_3}([IP_3]_i - [IP_3]_k) \tag{13}$$

represent the flow of Ca^{2+} and IP_3, respectively, from astrocyte 'i' in the network to its neighboring cells (indicated by index k). Local and global calcium events are simulated upon focal light stimulation of astrocytes, i.e., a region in the center of the network. Simulations were performed with varying levels of Ca^{2+} coupling coefficient, $D_{Ca^{2+}}$, in the presence and absence of Ca^{2+} buffering. Calcium responses in the network, i.e., the basal levels and spiking rates, were fitted with a symmetrical 2D Gaussian profile ($H(\zeta)$) to

quantify the peak Ca^{2+}-basal/spiking ($h_{max,\zeta}$), as well as the magnitude of the spread of Ca^{2+}-basal/spiking activity (σ_ζ) within the network:

$$H(\zeta) = h_{min,\zeta} + \frac{(h_{max,\zeta} - h_{min,\zeta})}{2\pi\sigma_\zeta^2 \exp(-\frac{(x - x_0)^2 + (y - y_0)^2}{2\sigma_\zeta^2})}, \tag{14}$$

where ζ represents calcium basal level or mean spiking rate, $h_{min,\zeta}$ is the minimum value of the ζ in the network, x_0 and y_0 are the indices of the astrocyte at the center, and x and y are the location of cells away from the origin in both directions. The effect of calcium buffering, varying levels of $D_{Ca^{2+}}$, and the number of cells expressing ChR2 on both the peak and spread of basal/spiking activity was investigated.

All simulations were performed in MATLAB using the Local Linearization method described in refs. (Jimenez & Ozaki, 2003; Ozaki, 1993) with an integration step size of 0.1 ms. A listing of all parameters and their descriptions is provided in Tables 3-1 and 3-2. The codes associated with this study can be downloaded from http://web.eng.fiu.edu/jrieradi/CaAnalysisCode/.

63
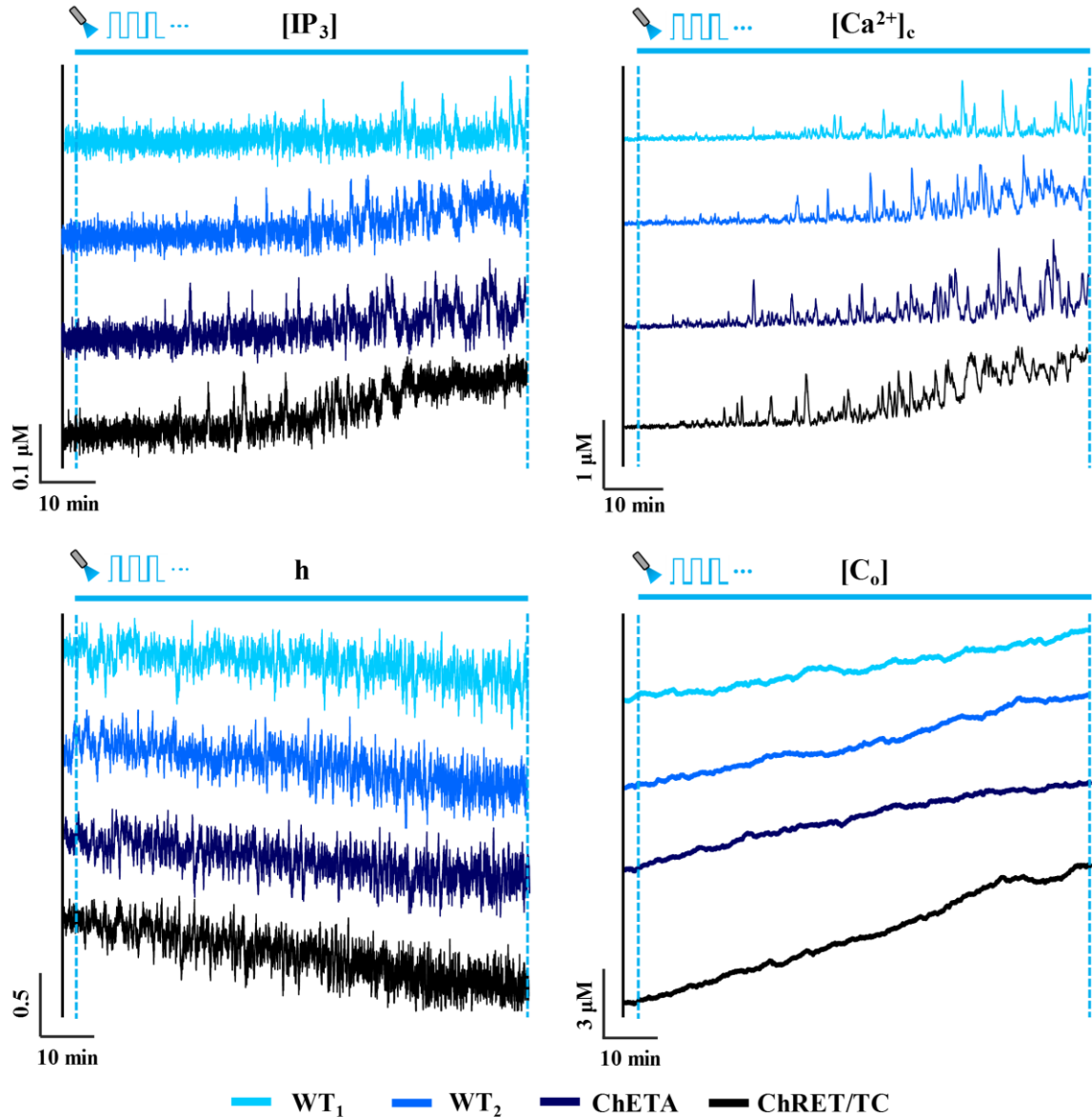
Figure 3-2 Response of ChR2 variants to light stimulation. Representative traces (90 minutes in duration) of IP$_3$ concentration ([IP$_3$]), cytosolic calcium concentration ([Ca^{2+}]$_c$), fraction of open inactivation IP$_3$R gates (h), and total calcium concentration ([C$_o$]) for an astrocyte expressing various ChR2 variants (wild type 1 (WT$_1$), wild type 2 (WT$_2$), ChETA and ChRET/TC) in response to light stimulation (T = 2 s, δ = 20% (0.4 s), unit amplitude). The blue horizontal solid line indicates the stimulation window.

3.3   RESULTS

3.3.1   Effect of ChR2 variants on the light-evoked response of astrocytes

Representative traces for the time evolution of state variables of Eq. 1 for astrocytes

64

expressing different variants of ChR2 are illustrated for 90 minutes of light stimulation (Figures 3-2 and A3-1). Simulations reveal a progressive increase in the spiking activity of cytosolic calcium in all variants with the duration of the stimulus. Apparent in the traces is a lag between the onset of light stimulation and regions with more regular spiking activity, likely reflecting the time required for $[Ca^{2+}]_c$ to reach sufficient levels to activate IP$_3$R channels. Traces show a steady increase in the total calcium content of the cell, and conversely, a decreasing trend in the fraction of open IP$_3$R inactivation gates (h). The [IP$_3$] levels, however, show a rather steady profile for WT and ChETA variants and predict only a slight increase towards the end of the stimulation window for ChRET/TC. This increase can be attributed to the elevated basal $[Ca^{2+}]_c$ in ChRET/TC expressing astrocytes, activating the production of IP$_3$ via the PLC$_{\delta 1}$ pathway ([Ca^{2+}] at half- maximal activation of PLC$_{\delta 1}$ is ~0.5 μM, Table 3-1). Comparison of results across variants suggests that light-induced changes are steepest in astrocytes expressing ChRET/TC. These model predictions are in line with the higher magnitude of the ChR2 flux in ChRET/TC compared to other variants in both transient and plateau regions of the photocurrent during the light stimulus (Figure A3-2). Furthermore, results suggest that for the simulation time in this figure, the mechanism of light-evoked increased spiking in cytosolic calcium, predominantly in WT or ChETA enabled astrocytes, is mainly through the activation of IP$_3$Rs by increases in $[Ca^{2+}]_c$ rather than elevations in [IP$_3$].

3.3.2   Effect of light stimulation paradigm on single cell model response

Heat maps (Figure 3-3A) show the effect of various light stimulation paradigms on the spiking rate and Ca^{2+} basal level in ChETA-expressing astrocytes for different stimulation

times, i.e., 45, 90, and 270 mins (for other ChR2 variants refer to Figure A3-3). Simulations show that as the stimulus duration increases, the Ca^{2+} basal level rises steadily due to a net Ca^{2+} entry into the cytosol (note the upward trend of $[C_o]$ in the traces of Figure 3-2). This effect is demonstrated in representative traces of Figure 3-3B, where depending on the T-δ combination, $[Ca^{2+}]_c$ may reach supraphysiological, toxic levels, which bring the cell outside of the window for regular spiking (i.e., $[Ca^{2+}]_c$ window for IP$_3$R-mediated Hopf bifurcation; notice the bottom trace of Figure 3-3B). Consequently, T-δ combinations that elicit high spiking activity in astrocytes during short-term stimulation (45 min) will transition into regions with medium and low activity as the stimulus progresses (notice the ◊ symbol in spiking rate heat maps, bottom panel of Figure 3-3A). Conversely, as seen in the top trace of Figure 3-3B, combinations with low levels of spiking in short-term stimulations might transition into regions eliciting high calcium activation, with basal levels within the physiological range, as the stimulation progresses. Thus, to remain within optimal spiking and basal $[Ca^{2+}]_c$ levels, one might choose stimulus waveforms based on the desired stimulation duration. It should be noted, however, that the predicted behavior is also a consequence of the Ca^{2+} buffering capacity of the cell, light intensity, and parameters determining the shape and magnitude of the ChR2 photocurrent (Figure 3-4).
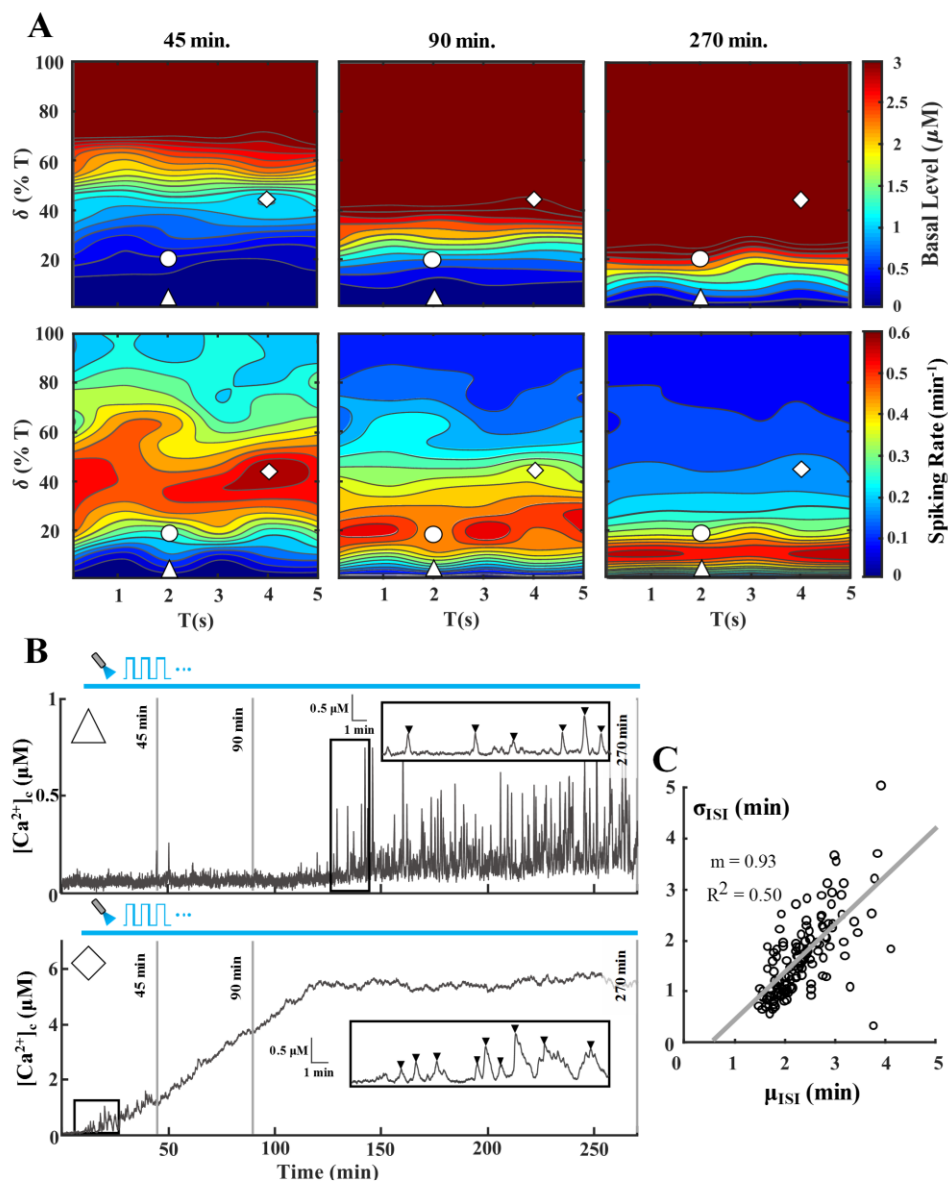
Figure 3-3 Response of a ChETA-expressing astrocyte to various light stimulation paradigms. Simulations were conducted to evaluate astrocytic Ca^{2+} response to different paradigms ranging from T = 1-5 s and δ = 0-100% of T (trials = 5). **(A)** Heat maps of Ca^{2+} basal level (top panel) and spiking rate (bottom panel) for the T-δ combinations assessed. Each column depicts basal level and spiking rate heat maps up to a certain point, i.e., 45, 90, and 270 minutes, to determine the cell response as light stimulation progresses from short-term to long-term. Scale bars for heat maps of basal level and spiking rate were capped to 3 μM and 0.6 spikes/min, respectively. The △ and ◊ symbols correspond to T-δ combinations that result in the traces of panel B. **(B)** Representative [Ca^{2+}]$_c$ traces corresponding to T-δ combinations highlighted in A [Top trace (△): T = 2 s, δ = 1% (0.02 s); Bottom trace (◊): T = 4 s, δ = 45% (1.8 s)]. The inset of each trace highlights a 15-minute section to show the detected Ca^{2+} spikes. For spike detection, a threshold of 0.2 μM above the basal level was utilized. Each vertical solid grey line denotes the time points corresponding to heatmaps of panel A. **(C)** Average (μ$_{ISI}$) vs. standard deviation of ISI (σ$_{ISI}$) where each point corresponds to a single simulated 270-min [Ca^{2+}]$_c$ trace. Solid line shows the linear fit between μ$_{ISI}$ and σ$_{ISI}$ values. Throughout

the manuscript, $\triangle$, $\circ$, and $\lozenge$ represent paradigms resulting in low, medium, and high Ca^{2+} spiking during short-term (45 min) stimulation of astrocytes, respectively.
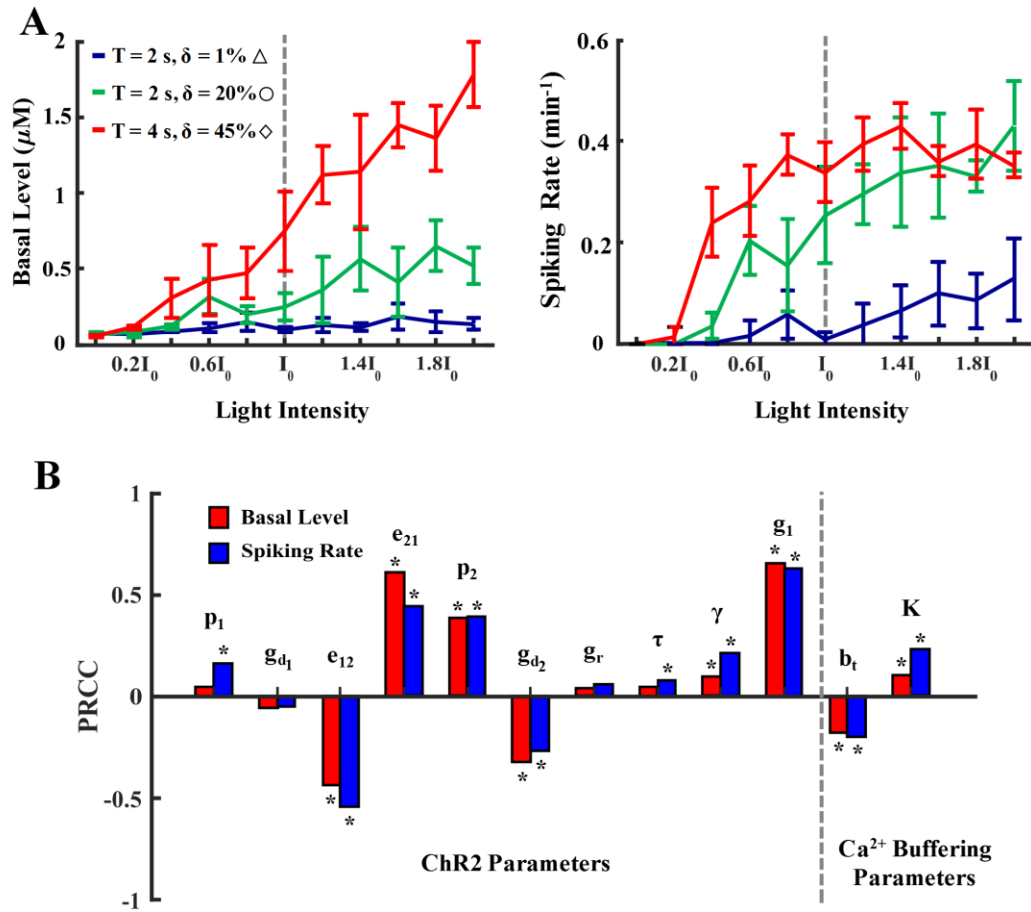
Figure 3-4 Model sensitivity to light intensity, Ca^{2+} buffering, and ChR2 parameters. **(A)** Effect of different light intensities and stimulation paradigms on the basal level and mean spiking rate of a ChETA-expressing astrocyte. Light intensity was varied as a fraction of the control value (I_0). Stimulation paradigms were selected based on the 45-min spiking rate heat map in Figure 3-3A for low ($\triangle$), medium ($\circ$), and high ($\lozenge$) activity regions. Data is shown as mean $\pm$ std (trials = 5). **(B)** Global sensitivity analysis of the astrocytic Ca^{2+} response to variations in ChR2 and Ca^{2+} buffering parameters during light stimulation (Δ: T = 2 s, δ = 1% (0.02 s)). Parameters were allowed to vary within a range (Table 3-2) and 1000 parameter sets were selected using Latin Hypercube Sampling (LHS) with uniform distribution. The partial rank correlation coefficient (PRCC) of each parameter was calculated as a measure of their effect on the basal level (red) and spiking rate (blue) of a ChR2-expressing astrocyte. * denotes statistically significant ($p < 0.05$) positive or negative influence.

To quantify the regularity of light-evoked calcium spiking in the astrocyte model, we demonstrate the σ_{ISI}-μ_{ISI} relationship for the inter-spike interval (ISI) values, i.e., the time

between subsequent calcium spikes, of simulations in Figure 3-3A. The average and standard deviation of ISI of the $[Ca^{2+}]_c$ traces are represented by μ_{ISI} and σ_{ISI}, respectively. This analysis has been performed for different cell types, including astrocytes, during spontaneous as well as IP$_3$-induced calcium oscillations (A. Skupin et al., 2010; Alexander Skupin et al., 2008). In agreement with these experimental observations, results from our simulations also show a positive and linear correlation between μ_{ISI} and σ_{ISI} values in the astrocytic calcium spiking during light stimulation (Figure 3-3C). Regions with Ca^{2+} levels outside of the predicted range for sustained oscillations, i.e., regions with either low or supraphysiological Ca^{2+} basal levels, result in infrequent and irregular spiking with higher μ_{ISI} and σ_{ISI} values.

3.3.3 Sensitivity to model parameters

Simulations predict salient features of light-induced responses in our model astrocyte, i.e., regions with elevated calcium spiking and a steady rise in the Ca^{2+} basal level. Results in Figure 3-4A show the effect of light intensity, or equivalently the amplitude of the waveform, on the Ca^{2+} response of ChETA-expressing astrocytes for three distinct T-δ combinations. These paradigms correspond to regions with low ($\triangle$), medium ($\circ$), and high ($\lozenge$) spiking activity in the 45-minute stimulation heatmap of Figure 3-3A, respectively. For all combinations, the Ca^{2+} basal level shows an upward trend with increasing light intensity (with varying slopes), indicating a larger Ca^{2+} influx through ChR2. Similar trends are observed for spiking rates in the case of low and medium T-δ combinations. For the stimulus paradigm with the highest spiking under control conditions (I_0), the spiking rate plateaus over a range of intensity values and follows a declining trend upon further increase

in the light intensity. This indicates that the associated increase in the basal level leads to a decrease in the firing rate of astrocytes as cytosolic calcium levels exit the region where regular oscillations can occur. These model predictions are similar to experimental observations of a monotonic increase in the firing of ChR2-positive neurons stimulated with increasing light intensities (H. Wang et al., 2007).

We further performed a global sensitivity analysis to evaluate the effect of parameters determining the dynamics of ChR2 photocycle and buffering capacity on the astrocytic Ca^{2+} responses for a low light stimulation paradigm (Figure 3-4B). Parameters that exerted statistically significant influence on the desired model output are marked with an asterisk. Results indicate the differential effects of model parameters on the Ca^{2+} response of the astrocyte to light stimulation. For instance, increasing the maximum conductance of ChR2 in o_1 state (g_1) is positively correlated with both spiking rate and basal levels, as the elevated conductance results in higher magnitudes of Ca^{2+} influx through the channel resulting in the elevation of basal levels and further activation of IP$_3$Rs. Similarly, e_{21} (the rate of transition from o_2 to o_1) has a positive correlation with both measures, while the rate of the reverse reaction (e_{12}) is shown to be negatively correlated to the model output. These results suggest that by transitioning the state of ChR2 from o_2 to o_1, both spiking rate and basal level of Ca^{2+} will likely increase. This model prediction can be attributed to the higher conductance of the channel in the o_1 state, the transient region of the ChR2 photocurrent in Figure A3-2, compared to o_2 state, the plateau region. Global sensitivity analysis of the Ca^{2+} buffering parameters demonstrates that with increasing buffering capacity, i.e., increasing total buffer concentration (b_t) or reducing the affinity of buffer proteins to Ca^{2+}

(K), both basal Ca^{2+} level and mean spiking rate of single astrocytes will expectedly decrease.

3.3.4 Network-wide astrocytic response to light stimulation

A 10-by-10 network of gap-connected astrocytes was modeled in Figure 3-5. Light stimulation ($T = 4s$, $\delta = 45\%$; $D_{Ca^{2+}} = 0.1$ s^{-1}) was applied to a central region (the highlighted box in Figure 3-5A), and simulations were performed for 45 minutes. Figure 3-5A heatmaps demonstrate the resulting basal Ca^{2+} level in the network after light stimulation, with and without the inclusion of Ca^{2+} buffering. Under both conditions, results show increased basal levels in the stimulated region and the propagation of calcium to unstimulated cells. Basal levels reached in focal and distal astrocytes without buffering were drastically higher compared to those with buffering. In the presence of Ca^{2+} buffering, only the area in close vicinity of the stimulated region exhibits an increase in the basal level, whereas, in the absence of buffering, even the cells farthest from the stimulation region undergo an increase in calcium. This suggests that buffering reduces the diffusion range of Ca^{2+} within the network, thereby limiting propagation. Given the focal and centered stimulation of the network, the distribution of calcium can be suitably quantified using a 2D Gaussian fit (Eq. 14). In Figure 3-5B, the peak basal level, along with the spread from the center (in terms of number of astrocytes), are quantified with varying $D_{Ca^{2+}}$ values. In both cases, an intuitive decrease in peak basal level coupled with an increase in the spread is observed as $D_{Ca^{2+}}$ increases. Both trends plateaued as $D_{Ca^{2+}}$ values reached higher than 0.1 s^{-1}.
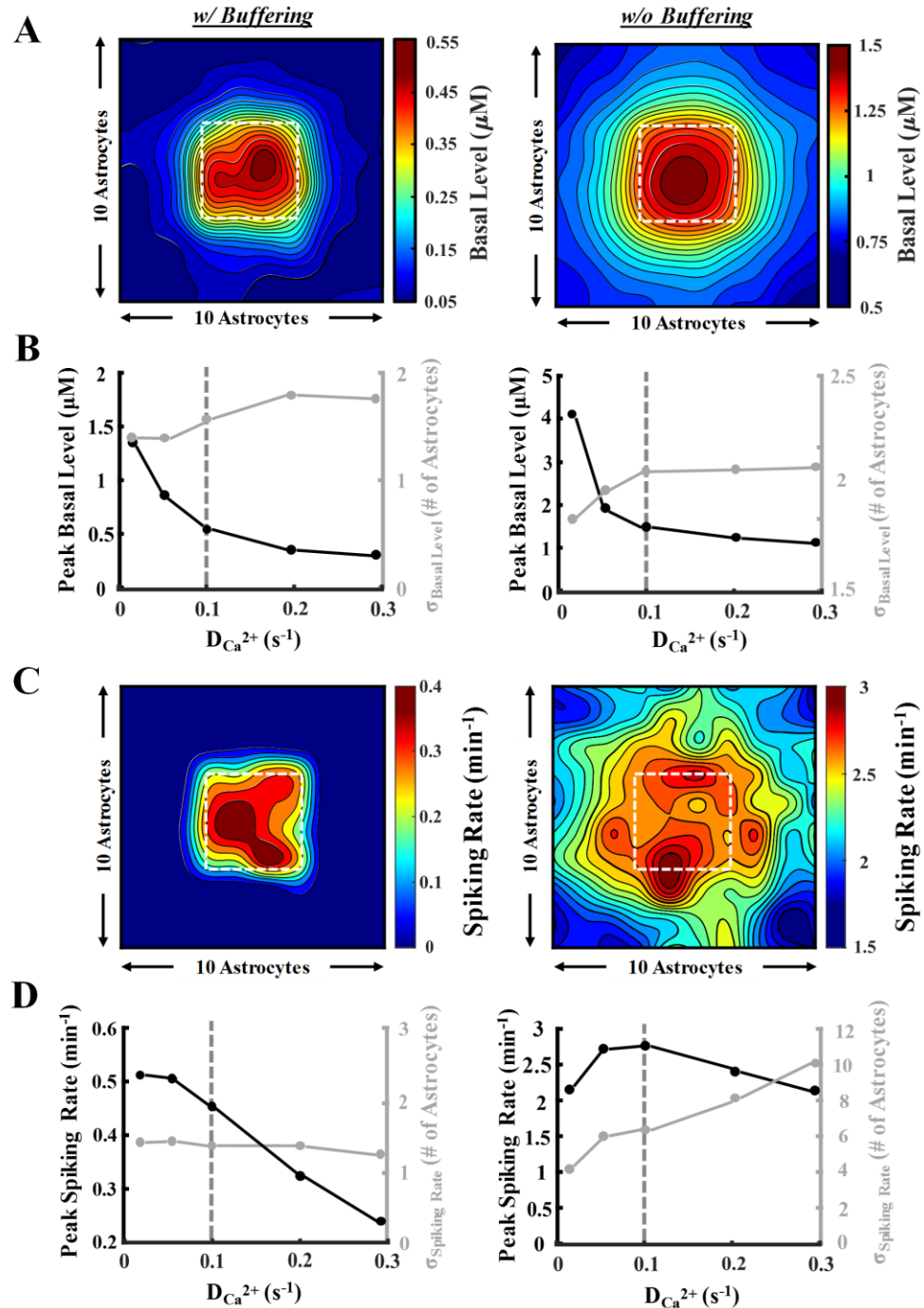
Figure 3-5 Network-wide astrocytic Ca²⁺ response to light stimulation. A 10-by-10 network of astrocytes was employed to analyze the response of cells when the central 4-by-4 astrocytes (white square in heatmaps of panels A and C) were stimulated ($\Diamond$: T = 4 s, δ = 45% (1.8 s), 45 min). See the network organization schematic in Figure 3-1. Simulations were conducted in the presence (left panel) and absence (right panel) of Ca²⁺ buffering with varying gap junctional Ca²⁺ coupling coefficient ($D_{Ca^{2+}}$). A symmetric 2D Gaussian fit was utilized to quantify the response, i.e., peak and magnitude of the spread from the stimulated region. **(A)** Heat maps of network-wide light stimulation-induced Ca²⁺ basal levels. **(B)** Plots of the peak basal level and $\sigma_{basal\text{-}level}$ obtained from the Gaussian fit with varying $D_{Ca^{2+}}$ values. Vertical dashed grey line denotes the

$D_{Ca^{2+}}$ value used to generate the heat maps in panels A and C. **(C)** Heat maps of network-wide spiking rate response corresponding to basal levels in panel A. For spike classification, a threshold of 0.2 μM above the basal level was selected. **(D)** Plots for the peak spiking rate and $\sigma_{spiking\ rate}$ with varying $D_{Ca^{2+}}$ values.

Similar responses are observed in the mean spiking rate of the astrocytic network upon light stimulation (Figure 3-5C). The inclusion of calcium buffering limited the spiking activity of astrocytes only in regions immediately surrounding the stimulated region. On the contrary, without calcium buffering, the spiking activity propagated to unstimulated areas and resulted in much higher mean spiking rate values. Analysis of network-wide peak spiking rate and spread with buffering in Figure 3-5D (left panel) indicates a decreasing trend of peak spiking with $D_{Ca^{2+}}$. The propagation of the spiking rate, however, remained almost unchanged over the entire range of $D_{Ca^{2+}}$ values examined. Conversely, when buffering was not included (Figure 3-5D, right panel), the increase in $D_{Ca^{2+}}$ resulted in an increasing trend in the spread of spiking activity while the peak spiking rate remained at high values throughout. Increasing the number of cells expressing ChR2 in the network also resulted in a steady increase in both spiking rate and Ca^{2+} basal levels in the network (Figure A3-4) when buffering was included. With no buffering, the peak basal level showed a steep incline, while the spread remained constant. Both peak spiking rate and spread showed an upward trend with increased expression level, with peak levels reaching a plateau when higher than 50% of the cells expressed ChR2. Collectively, simulations in Figure 3-5 highlight the role of Ca^{2+} buffering in limiting the diffusion of free Ca^{2+} in the network of astrocytes and thereby reducing both the basal and spiking levels of calcium in cells. Additionally, comparison of the network results with those of single cells (Figure 3-3) reveals that the dispersion of Ca^{2+} into the neighboring cells through gap junctions drastically reduces the supraphysiological values of Ca^{2+} predicted in isolated cells.

3.4   DISCUSSION

In this study, we discuss the development of a mathematical model to analyze light-evoked changes in the Ca^{2+} dynamics of astrocytes expressing the most widely used opsin—ChR2. In our analysis, we used three existing ChR2 variants, wild type, ChETA, and ChRET/TC. The outlined framework can be further expanded to investigate other opsins when the channel characterizations become readily available. We incorporated a 4-state model of ChR2 photocycle, as previous studies have demonstrated its superiority in capturing the dynamics of the ChR2 photocurrent compared to 3-state models (Nikolic et al., 2009; Stefanescu et al., 2013). Selectively targeting astrocytes, and their Ca^{2+} signaling, using advanced techniques like optogenetics can aid in resolving controversies (discussed in Chapter 1) and help find answers to their exact roles in health and disease. The mathematical modeling framework outlined in our study is a step in this direction in providing a tool for experimentalists to precisely achieve desired astrocytic Ca^{2+} levels to examine their role in the abovementioned phenomena.

3.4.1   Salient features of light-evoked calcium signaling in astrocytes

Simulation results predict that calcium dynamics in astrocytes, as seen in experimental studies (Balachandar et al., 2020; Figueiredo et al., 2014; Figueiredo et al., 2011), can be heavily regulated by light-induced activation of ChR2. Consistent in all simulations performed in this study, upon light activation, astrocytes underwent increases in their basal calcium level and exhibited changes in the spiking activity (Figures 3-2 and 3-3). Our results demonstrate that the extent of the rise in calcium (reflecting the higher magnitude of entry through ChR2 compared to the rate of scavenging by PMCA, SERCA, and buffer

proteins) is largely dependent on the specifications of the laser stimulus, i.e., T-δ combination and light intensity, as well as parameters determining the shape of the ChR2 photocurrent (Figures 3-3 and 3-4). Additionally, whether astrocytes show high or low spiking activity is also contingent upon the duration of light stimulation. As such, T-δ combinations with high spiking activity of single cells in short-term stimulations may transition to regions with medium or low spiking in longer durations, or vice versa (Figure 3-3B). These results emphasize the importance of choosing an 'ideal' T and δ combination for the desired short-term or long-term astrocytic activity. An inaccurate selection of these combinations could prompt astrocytes to an unphysiological Ca^{2+} signaling regime, which might be detrimental for the health of the cells. Whether these model predictions are physiologically accurate needs to be validated against experimental observations for both short and long-term activation of ChR2. When coupled with other astrocytes in a network, however, the dispersion of calcium to neighboring cells dramatically reduced the basal levels reached in the stimulated region (Figure 3-5A), with values depending on the magnitude of the calcium and IP_3 coupling coefficients in the network. This indicates that experimental design for optogenetic stimulation of a network of astrocytes, e.g., *in vivo* recordings, cannot be solely based on predictions drawn from single cells and that network activity depends on ChR2 expression level (Figure A3-4).

3.4.2 Engineering of application-based ChR2 variants

Several research groups have engineered ChR2 variants with distinct characteristics, e.g., enhanced conductance, sensitivity, and faster recovery kinetics (André Berndt et al., 2011; Gunaydin et al., 2010) for specific applications in excitable cells. Our study results can be

useful in the development of future ChR2 constructs for eliciting desired activity targeting astrocytes. More specifically, results of our sensitivity analysis (Figure 3-4B) indicated that the kinetics of ChR2 photocycle significantly affect the Ca^{2+} spiking rate and basal levels. Intuitively, directing ChR2 to the open states (o_1 and o_2) from the closed states (c_1 and c_2) leads to an increase in astrocytic activity in response to light stimulation. For instance, decreasing G_{d_1} and G_{d_2} facilitates the existence of ChR2 in the open states as they are negatively correlated to both basal level and spiking rate. Also, an increase in p_2 drives the system to the open state and is positively correlated to both measures. However, less intuitively, for the simulations performed in our study, increased astrocytic activity was achieved when ChR2 resided more in the o_1 state as compared to the o_2 state. This can be observed as an increase in e_{21} and a decrease in $e_{12,}$ leading to the existence of ChR2 in o_1 (see Figure 3-1 ChR2 photocycle). The shape of the photocurrents in Figure A3-2 also confirms that the channel has the highest flux in the o_1 state (the transient phase). Collectively, these results suggest that tailoring new ChR2 constructs such that the photocurrent is directed mainly towards the o_1 state can enhance the astrocytic activity. The same analysis can be performed under different stimulation paradigms and for varying durations of stimulus.

Table 3-1 Model Parameters.

	Value	Unit	Description	Source
IP$_3$ Dynamics				
v_δ	0.15	µM/s	Maximum rate of IP$_3$ production (PLC$_{\delta 1}$)	(J. Riera, Hatanaka, Ozaki, et al., 2011)
$K_\delta Ca$	0.55	µM	Half saturation constant of Ca^{2+} (PLC$_{\delta 1}$)	(J. Riera, Hatanaka, Ozaki, et al., 2011)
K_{IP_3}	1.25	s^{-1}	IP$_3$ degradation rate	(J. Riera, Hatanaka, Ozaki, et al., 2011)
X_{IP_3}	0.14	µM/s	Basal level of cytosolic IP$_3$ production	(J. Riera, Hatanaka, Ozaki, et al., 2011)
Ca^{2+} Dynamics				
x_{CCE}	0.01	µM/s	Maximum CCE influx	(J. Riera, Hatanaka, Ozaki, et al., 2011)
h_{CCE}	10	µM	Half-inactivation constant for CCE influx	(J. Riera, Hatanaka, Ozaki, et al., 2011)
α_1	0.19	~	Volume ratio between ER and cytosol	(J. Riera, Hatanaka, Ozaki, et al., 2011)
v_{SERCA}	0.90	µM/s	Maximum rate constant of SERCA pump	(J. Riera, Hatanaka, Ozaki, et al., 2011)
K_p	0.10	µM	Half-maximal activation of the SERCA pump	(J. Riera, Hatanaka, Ozaki, et al., 2011)
d_1	0.13	µM	Dissociation constant for IP$_3$ (IP$_3$R)	(J. Riera, Hatanaka, Ozaki, et al., 2011)
d_5	0.08	µM	Ca^{2+} activation constant (IP$_3$R)	(J. Riera, Hatanaka, Ozaki, et al., 2011)
v_1	6	s^{-1}	Ligand-operated IP$_3$R channel flux constant	(J. Riera, Hatanaka, Ozaki, et al., 2011)
v_2	0.11	s^{-1}	Ca^{2+} passive leakage flux constant	(J. Riera, Hatanaka, Ozaki, et al., 2011)
k_{out}	0.50	s^{-1}	Rate constant of Ca^{2+} extrusion	(J. Riera, Hatanaka, Ozaki, et al., 2011)
λ	1	~	Time scaling factor	(J. Riera, Hatanaka, Ozaki, et al., 2011)
ε	0.01	~	Ratio of PM to ER membrane surface area	(J. Riera, Hatanaka, Ozaki, et al., 2011)
J_{in}	0.04	µM/s	Passive leakage	(J. Riera, Hatanaka, Ozaki, et al., 2011)
V_m	-70	mV	Membrane voltage	Model assumption
$G(V_m)$	$\dfrac{\left(10.6\text{-}14.6\exp^{-\left(\frac{V_m}{42.7}\right)}\right)}{V_m}$	~	Voltage dependent rectification function	(J. C. Williams et al., 2013)
vol_{cyt}	10^{-12}	L	Volume of the cytosol, assuming spherical cell	(V. Williams, Grossman, & Edmunds, 1980)
A_m	4.83×10^{-6}	cm^2	Surface area of the astrocyte membrane (calculated using vol_{cyt} and	Model assumption

				assuming spherical cell shape)	
F	9.65×10^4		C/mol	Faraday's constant	
$\mathbf{z_{Ca^{2+}}}$	2		~	Valence of Ca^{2+} ions	
$\mathbf{b_t}$	200		μM	Total buffer protein concentration	(Savtchenko et al., 2018)
K	20		μM	Buffer rate constant ratio	(Savtchenko et al., 2018)
N	20		~	Number of IP_3Rs within a cluster	(Shuai & Jung, 2002)
Gating Parameters					
a	0.20		$(μMs)^{-1}$	Rate constant for Ca^{2+} binding in IP_3 inhibitory site	(J. Riera, Hatanaka, Ozaki, et al., 2011)
$\mathbf{d_2}$	1.05		μM	Dissociation constant for Ca^{2+} inhibition (IP_3R)	(J. Riera, Hatanaka, Ozaki, et al., 2011)
$\mathbf{d_3}$	0.94		μM	Dissociation constant for IP_3 (IP_3R)	(J. Riera, Hatanaka, Ozaki, et al., 2011)
Network Dynamics					
$\mathbf{D_{IP_3}}$	1		s^{-1}	Coupling coefficient of IP_3	Model estimate
$\mathbf{D_{Ca^{2+}}}$	0.1		s^{-1}	Coupling coefficient of Ca^{2+}	Model estimate
Wiener Processes					
$\mathbf{\sigma_{IP_3}}$	0.02		$s^{-1/2}$	Variance of Wiener process of $[IP_3]$	(J. Riera, Hatanaka, Ozaki, et al., 2011)
$\mathbf{\sigma_{Ca^{2+}}}$	0.01		$s^{-1/2}$	Variance of Wiener process of $[Ca^{2+}]_c$	(J. Riera, Hatanaka, Ozaki, et al., 2011)
$\mathbf{\sigma_{c_o}}$	0.01		$s^{-1/2}$	Variance of Wiener process of $[C_o]$	(J. Riera, Hatanaka, Ozaki, et al., 2011)
ChR2 Parameters					
$\mathbf{p_1}$	**ChRWT$_1$** **ChRWT$_2$** **ChETA** **ChRET/TC**	0.06 0.12 0.07 0.13	ms^{-1}	Maximum excitation rate of c_1	(André Berndt et al., 2011; Gunaydin et al., 2010; Stefanescu et al., 2013)
$\mathbf{G_{d_1}}$	**ChRWT$_1$** **ChRWT$_2$** **ChETA** **ChRET/TC**	0.46 0.01 0.01 0.01	ms^{-1}	Rate constant for the o_1 to c_1 transition	(André Berndt et al., 2011; Gunaydin et al., 2010; Stefanescu et al., 2013)
$\mathbf{e_{12}}$	**ChRWT$_1$** **ChRWT$_2$** **ChETA** **ChRET/TC**	0.20 4.38 10.51 16.11	ms^{-1}	Rate constant for the o_1 to o_2 transition	(André Berndt et al., 2011; Gunaydin et al., 2010; Stefanescu et al., 2013)
$\mathbf{e_{21}}$	**ChRWT$_1$** **ChRWT$_2$** **ChETA** **ChRET/TC**	0.01 1.60 0.01 1.09	ms^{-1}	Rate constant for the o_2 to o_1 transition	(André Berndt et al., 2011; Gunaydin et al., 2010; Stefanescu et al., 2013)

p_2	ChRWT$_1$	0.06	ms^{-1}	Maximum excitation rate of c_2	(André Berndt et al., 2011; Gunaydin et al., 2010; Stefanescu et al., 2013)
	ChRWT$_2$	0.01			
	ChETA	0.06			
	ChRET/TC	0.02			
G_{d_2}	ChRWT$_1$	0.07	ms^{-1}	Rate constant for the o_2 to c_2 transition	(André Berndt et al., 2011; Gunaydin et al., 2010; Stefanescu et al., 2013)
	ChRWT$_2$	0.12			
	ChETA	0.15			
	ChRET/TC	0.13			
G_r	ChRWT$_1$	9.35×10^{-5}	ms^{-1}	Recovery rate of the c_1 state after light pulse is turned off	(André Berndt et al., 2011; Gunaydin et al., 2010; Stefanescu et al., 2013)
	ChRWT$_2$	9.35×10^{-5}			
	ChETA	1×10^{-3}			
	ChRET/TC	3.85×10^{-4}			
τ_{ChR2}	ChRWT$_1$	6.32	ms^{-1}	Activation time of the ChR2 ion channel	(André Berndt et al., 2011; Gunaydin et al., 2010; Stefanescu et al., 2013)
	ChRWT$_2$	0.50			
	ChETA	1.59			
	ChRET/TC	0.36			
g_1	ChRWT$_1$	0.11	mS/cm^2	Maximum conductance of the ChR2 ion channel in the o_1 state	(André Berndt et al., 2011; Gunaydin et al., 2010; Stefanescu et al., 2013)
	ChRWT$_2$	0.10			
	ChETA	0.88			
	ChRET/TC	0.56			
γ	ChRWT$_1$	0.03	~	Ratio of maximum conductance of the ChR2 ion channel in the o_2 and o_1 state $\left(\frac{g_2}{g_1}\right)$	(André Berndt et al., 2011; Gunaydin et al., 2010; Stefanescu et al., 2013)
	ChRWT$_2$	0.02			
	ChETA	0.01			
	ChRET/TC	0.02			
E_{ChR2}	All variants	0	mV	Reversal potential of ChR2	(J. C. Williams et al., 2013)

Table 3-2 Range of parameters for global sensitivity analysis.

Parameter	Range	Unit
ChR2 parameters		
p_1	$51.28 - 1.50 \times 10^2$	ms^{-1}
G_{d_1}	$8.16 - 5.47 \times 10^2$	ms^{-1}
e_{12}	$163.52 - 1.93 \times 10^4$	ms^{-1}
e_{21}	$4.00 - 1.92 \times 10^3$	ms^{-1}
p_2	$10.00 - 7.69 \times 10^1$	ms^{-1}
G_{d_2}	$56.32 - 1.81 \times 10^2$	ms^{-1}
G_r	$7.48 \times 10^{-2} - 1.20$	ms^{-1}
τ_{ChR2}	$2.89 \times 10^{-4} - 7.6 \times 10^{-3}$	ms^{-1}
γ	$1.13 \times 10^{-2} - 3.66 \times 10^{-2}$	~
g_1	$7.84 \times 10^{-2} - 1.05$	mS/cm^2
Buffering Parameters		
b_t	$160 - 240$	μM
K	$16 - 24$	μM

APPENDIX A3
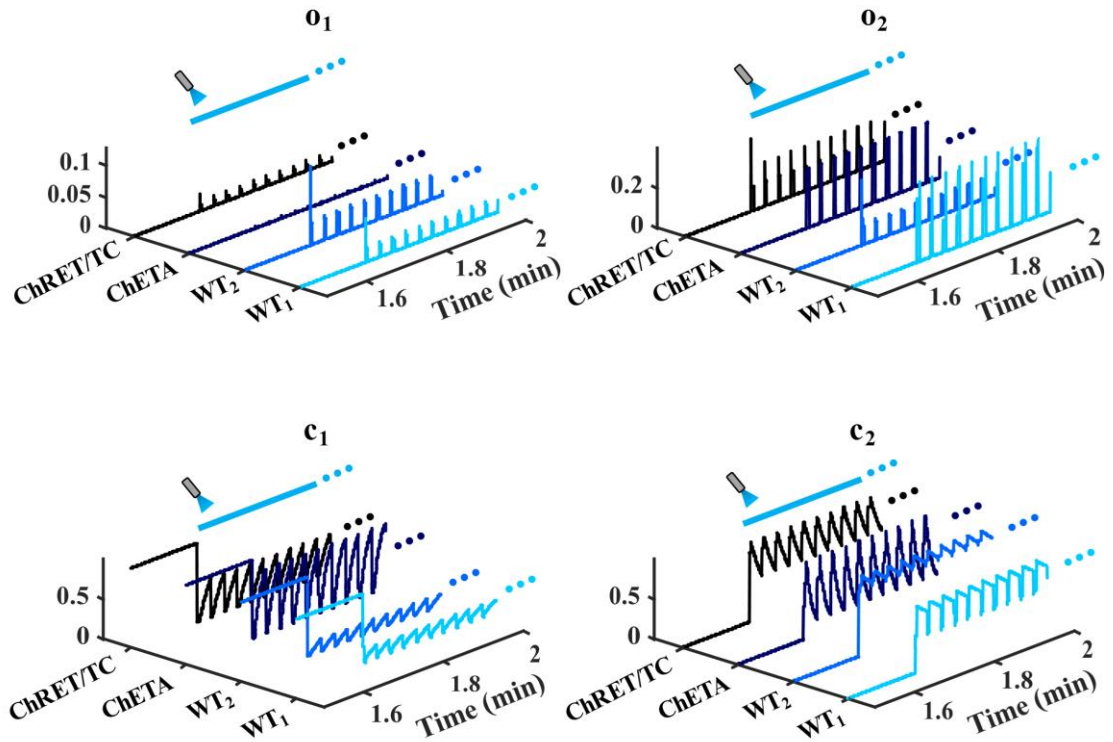
Figure A3-1 ChR2 gating dynamics during light stimulation. Representative traces of open state (o_1 and o_2) and closed state (c_1 and c_2) gating dynamics during light stimulation, corresponding to the 90-min simulation depicted in Figure 3-2 (wild type 1 (WT_1), wild type 2 (WT_2), ChETA. and ChRET/TC). A 30-second segment of each trace is shown to highlight details. Prior to light stimulation, all variants reside in the c_1 state. Once stimulation is initiated, the variants reside in different states at varying levels. Within the open states, they mainly reside in o_2. The solid horizontal blue line corresponds to the period during which the light stimulation was on.
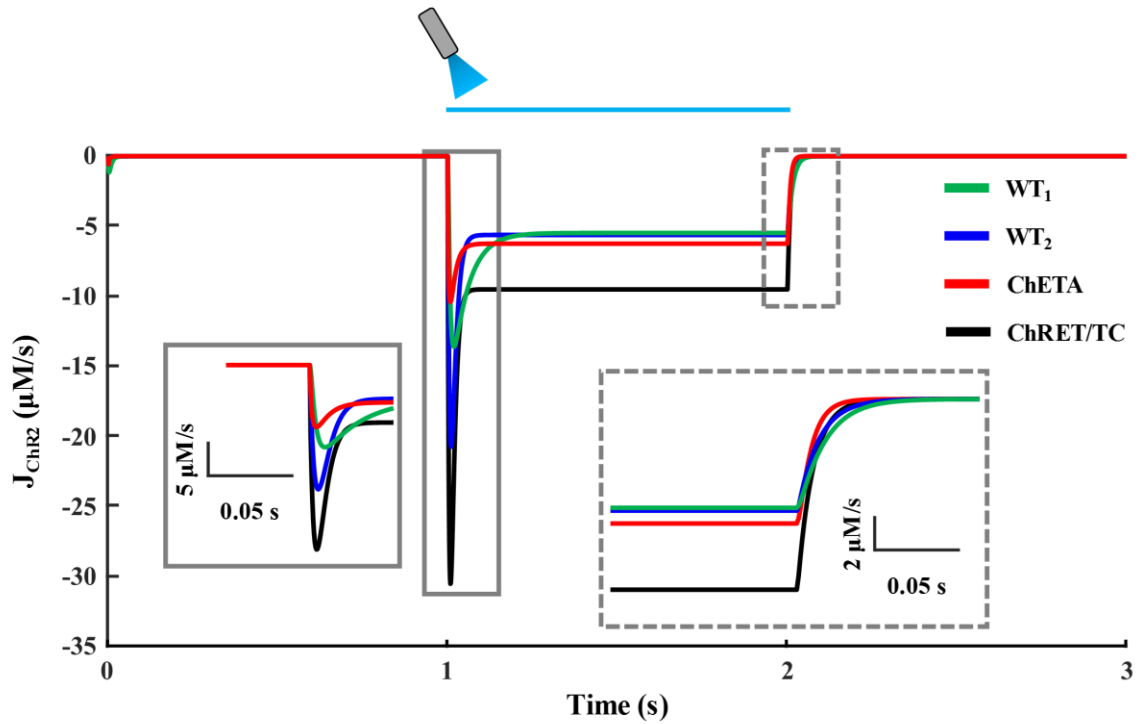
Figure A3-2 Comparison of the ChR2 flux across variants. Simulated ChR2 channel flux (J_{ChR2}) in response to a 1-sec pulse stimulation. The solid horizontal blue line corresponds to the period during which the light pulse was on. The solid grey box highlights a transient phase, during which all variants exhibit a brief large-magnitude flux (ChRET/TC > WT_2 > WT_1 > ChETA), corresponding to the light-induced transition to the o_1 state. The dashed grey box shows the plateau phase of the flux, corresponding to the transition and stabilization in the low-magnitude o_2 state. The plateau phase flux magnitudes are in the order ChRET/TC > ChETA > WT_2 > WT_1.
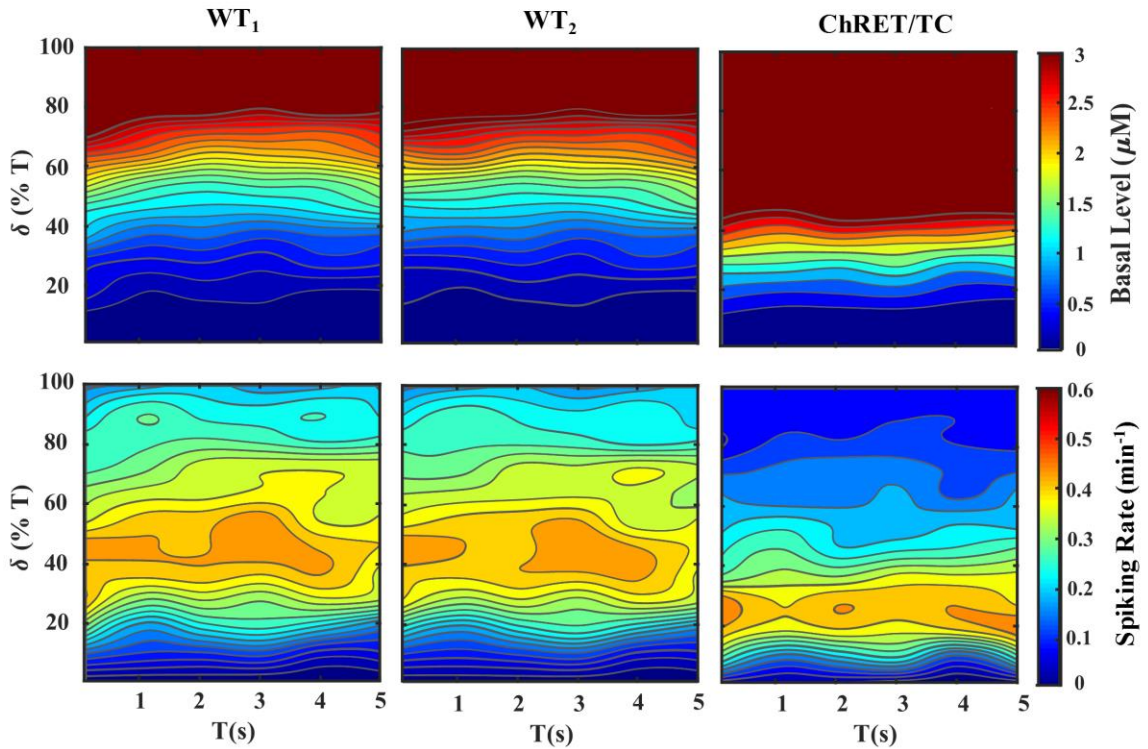
Figure A3-3 Response of astrocytes expressing different ChR2 constructs to various light stimulation paradigms. Simulations (45 min) were conducted to evaluate astrocytic Ca^{2+} response while expressing various ChR2 constructs. Different stimulation paradigms ranging from T = 1-5 s and δ = 0-100% of T (trials = 5) were applied from 100 seconds, until the end of the simulation. Each column corresponds to an evaluated ChR2 variant, i.e. WT_1 (left), WT_2 (center) and ChRET/TC (right). Heat maps of Ca^{2+} basal level (top panels) and spiking rate (bottom panels) for T-δ combinations are depicted. The scale bar for each heat map was capped to 3 μM and 0.6 spikes/min, respectively. For spike detection, a threshold of 0.2 μM above the basal level was utilized. Results show a similar basal level and spiking rate distribution for WT_1 and WT_2. However, ChRET/TC shows a smaller region of increased spiking activity coupled with a larger region of T-δ combinations eliciting supraphysiological basal level changes.
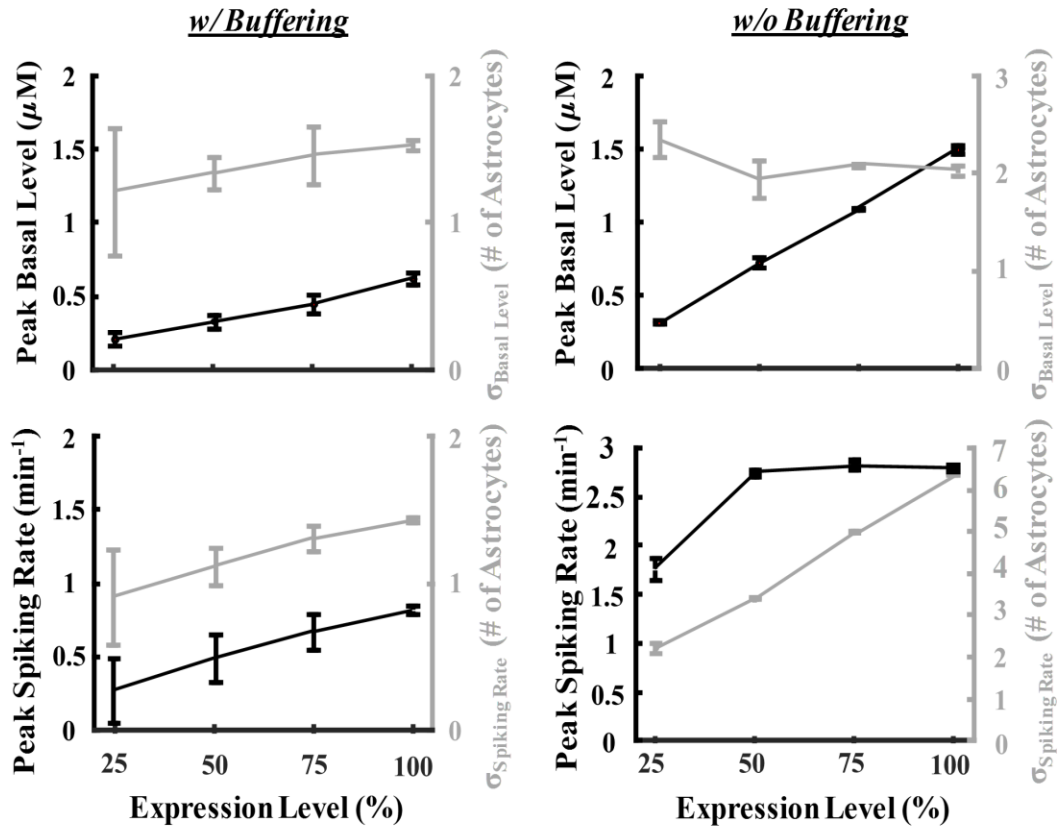
Figure A3-4 Effect of expression heterogeneity on the network-wide response to stimulation. A 10-by-10 network of astrocytes was used to demonstrate the resulting response when the expression of the central 4-by-4 astrocytes (white square in Figure 3-5A and C) is varied [Light stimulation: (◊) T = 4 s, δ=45% (1.8 s)]. Simulations were conducted for 45 minutes while the percentage of the central astrocytes randomly selected to express ChETA was varied (25, 50, 75, 100%) in the presence (left panel) and absence (right panel) of Ca^{2+} buffering. A total of 5 trials were conducted for each expression level. A symmetric 2D Gaussian fit was used to quantify the response, i.e., peak and magnitude of the spread from the stimulated region. Top row of plots shows the average and standard deviation of peak basal level and $\sigma_{basal\ level}$ as a function of expression. Bottom row of plots shows the average and standard deviation of peak spiking rate and $\sigma_{spiking\ rate}$ as a function of expression. For spike classification, a threshold of 0.2 μM above basal level was selected. Increasing the number of cells expressing ChR2 in the stimulation region resulted in a steady increase in both peak basal level and spiking rate in the presence of buffering, coupled with a steady increase in their corresponding σ values. A similar trend can be observed in the absence of buffering; however, after a threshold, the basal level continues to increase, while the spiking rate plateaus.

APPENDIX B3

Our research group is interested in performing longitudinal studies on mice, studying astrocytic Ca^{2+} signaling in the cortex while being optogenetically stimulated. As seen in Chapter 2, upon repeated stimulation with pulsed blue light, astrocytes show synchronized increases in Rhod-2 AM fluorescence (Figures 2-4 and 2-5A, B) that gradually return to basal fluorescence indicative of sharp Ca^{2+} fluctuations in these cells. This chapter exclusively detailed our computational model, which aims to provide a theoretical platform to identify light stimulation paradigms that elicit maximal astrocytic activity within physiological levels for short-term and long-term optogenetic stimulation. The example provided below (Figure B3-1) is a short-term Ca^{2+} recording (~12 minutes), along with the theoretical model response upon fitting some select model parameters, namely the whole-cell conductance of ChR2 and parameters determining the buffering capacity of the cell. The readout of our experimental data is a change in Rhod-2 AM fluorescence ($\Delta F/F_0$), which reflects changes in levels of Ca^{2+}. Our model simulations are presented as Ca_c and $\Delta B/B_0$, i.e., relative changes in the baseline, for comparison purposes. Although the comparison is rather qualitative, the example below demonstrates the model's ability to capture Ca^{2+} responses in astrocytes upon light stimulation.
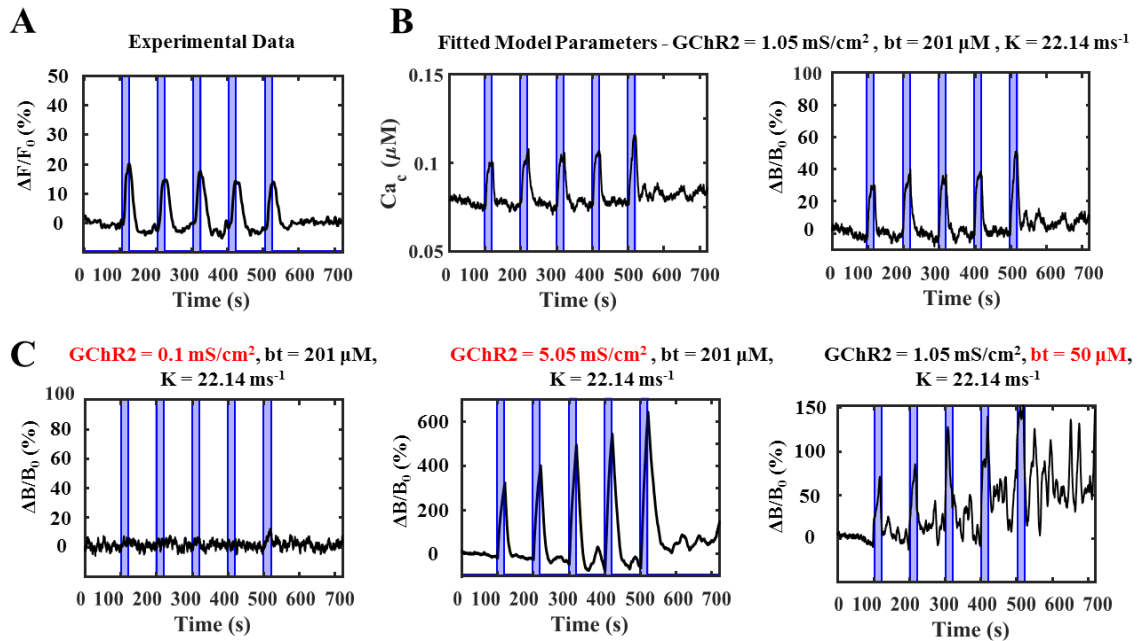
Figure B3-1 Model fitting of experimental data. (A) Average Rhod-2 AM $\Delta F/F_0$ of astrocytes from an MlC1-ChR2+ mouse slice subjected to repeated blue light stimulation over the recording period ($T = 100$ s and $\delta = 20\%$ of T, blue-shaded regions). Traces are normalized for comparison and visualized as $\Delta F/F_0$, where baseline fluorescence (F_0) is taken to be the median fluorescence intensity of the pre-stimulus imaging window. **(B)** Based on the sensitivity analysis performed in the manuscript (Figure 3-4B), model parameters (GChR2, bt, K) are selected and estimated to fit experimental data shown in A. Evidently, parameter values that fit the experimental data closely are similar to those used as the control values for the simulations in the manuscript (GChR2 = 0.8759 mS/cm^2, bt = 200 μM, K = 20 ms^{-1}). The left panel shows raw Ca^{2+} responses (n = 50 trials) upon repeated light stimulation, also represented as $\Delta B/B_0$ (calculated similarly to $\Delta F/F_0$) in the right panel. Values fitted to the experimental data are: GChR2 = 1.05 mS/cm^2, bt = 201 μM, K = 22.14 ms^{-1}, rest of the parameters remained the same as used in the manuscript. **(C)** Drastic variations (in red) in fitted parameters illustrating susceptibility of changes in $\Delta B/B_0$ of the Ca^{2+} response (n = 50 trials). The left panel shows an expected lack of response to light when GChR2 is a low value. The Center panel shows extreme supraphysiological increases in Ca^{2+} responses when GChR2 is increased by a factor of ~5 in reference to the value for ChETA. The right panel shows asynchronous increases in Ca^{2+} levels with respect to light stimulation due to a reduction of buffering.

CHAPTER 4   SEROTYPE-BASED EVALUATION OF AN OPTOGENETIC CONSTRUCT IN RAT CORTICAL ASTROCYTES

The content of this chapter is to be submitted as <u>Lakshmini Balachandar</u>, Diana Borrego, and Jorge Riera Diaz. "Serotype-based evaluation of an optogenetic construct in rat cortical astrocytes".

4.1   INTRODUCTION

Optogenetics—a novel state-of-the-art technique—provides a platform for precise cellular targeting and control using light, with the potential for delving into a variety of pathological conditions in the brain (Deisseroth, 2015; Fenno et al., 2011). One of the earliest investigations for astrocytic control using optogenetic methodologies by Gradinaru *et al.* (Gradinaru, Mogri, Thompson, Henderson, & Deisseroth, 2009) demonstrated the relevance of thalamic stimulation *in vivo* by employing a lentivirus-based delivery of the optogenetic construct for probing astrocytes. Few studies in literature also point out to the investigation of astrocytic Ca^{2+} dynamics and to study their role in cerebral blood flow and neurovascular coupling upon light stimulation (Figueiredo et al., 2014; Figueiredo et al., 2011; Masamoto et al., 2015). Rat-based models for studying a variety of brain disorders, including AD (Do Carmo & Cuello, 2013), FCD-II (Deshmukh et al., 2018), and Huntington's Disease (HD) (Hohn et al., 2011), can benefit from the translation of ChR2-based intervention of astrocytes. This can aid in understanding the roles of astrocytic Ca^{2+} signaling in several of these disorders and explore their translational potential.

Viral delivery of the optogenetic construct has precise cellular targeting, is both time and cost-effective, and facilitates application of optogenetics to existing rat disease models

(Kuhlman & Huang, 2008). For a multitude of reasons, adeno-associated viral (AAV) vectors are preferred for gene delivery over other viral vector types—lentiviral (LV), adenoviral vectors (AVV), and retroviral (RV). Their characteristics of low immunogenicity, ability to efficiently target both dividing and non-dividing cells, robust gene delivery, and persistence of expression in rodent models make them potent tools for research and gene therapy. Furthermore, they can be engineered to facilitate high transduction capabilities of a diverse set of target tissues and species (McCown et al., 1996; S. Nayak & R. W. Herzog, 2010; S. Sun & Schaffer, 2018).

Cellular targeting using AAV-based optogenetics requires an appropriate selection of the serotype. AAV capsid serotype plays a crucial role in determining the efficacy and extent of gene delivery and transduction. Serotype-based delivery differs based on target cell type, brain area, species of intervention, and size of the construct, which imparts unique capabilities of targeting a various range of cells. Tailoring the serotype also influences AAV vector transport and optimizing vector-host interaction (Buning, Huber, Zhang, Meumann, & Hacker, 2015; Chakrabarty et al., 2013; Salegio et al., 2013). Therefore, it is imperative to perform a comprehensive evaluation of an optogenetic construct for targeting a given brain region, cell type, and species.

This study seeks to provide a holistic characterization of AAV serotypes of a ChR2-based optogenetic construct for targeting rat cortical astrocytes and achieving maximal stable transduction patterns. We evaluate transduction patterns of the optogenetic component— AAV-GFAP-hChR2(H134R)-mCherry in rat cortical astrocytes. The selection of potential serotypes (1, 5, and 8) used in this study was based on previous findings *in vivo* and *in vitro*

for non-optogenetic constructs, in various CNS regions and species (Aschauer, Kreuz, & Rumpel, 2013; Koerber et al., 2009; Petrosyan et al., 2014). The virus was delivered to the rat brain by intracerebral injections and following perfusion and histology, astrocytic expression of the construct was evaluated. Upon quantification of transduction, we found that serotype 8 of the optogenetic construct had the maximum viral spread (in both tangential and radial directions), as compared to serotypes 1 and 5, in the astrocytes of the rat neocortex. Our results, therefore, suggest that rAAV8 can be employed as a tool for manipulating gene expression in rat cortical astrocytes *in vivo* for ChR2-based optogenetic interrogation. Our study provides an insight into a systematic serotype evaluation of AAV-based optogenetic astrocytic targeting, which can further be used to establish robust astrocytic control and mediation for interventions in neurological disorders.

4.2   MATERIALS AND METHODS

4.2.1   AAV viral vectors

AAV vectors (AAV-GFAP-hChR2(H134R)-mCherry) of serotypes 1,5 and 8 were provided by The University of North Carolina Vector Core at Chapel Hill (~10^{12} GC/ml).

4.2.2   Animal preparation and stereotaxic microinjections

Male Wistar rats (7-10 weeks) were housed in standard cages at a 12h-12h light-dark cycle with free access to food and water. All experimental procedures and animal care in this study are approved and carried out in compliance with the Institutional Animal Care and Use Committee (IACUC) at Florida International University (Approval No. 16-032,19-045), IBC (16-001,19-013), and NIH guidelines. The rats were anesthetized using

isoflurane anesthesia (5% for initial induction, 1.5% for maintenance, 1L/min O_2, 14.7 PSI). After mounting the rat's head on the stereotaxic frame (Narishige, Japan), the body temperature was maintained at ~37 °C using a water-circulating heating pad (TPZ-0510EA, Texas Scientific Instruments, LLC) with a pump (TP700, Texas Scientific Instruments, LLC). The temperature and respiration rate were monitored continuously using the PowerLabs 8/35 data acquisition device and the LabChart software (AD Instruments). An incision was made in the middle of the scalp, and connective tissue was cleared to better visualize the *lambda* and *bregma* stereotaxic coordinates. The measurements were taken from the top of the skull, bregma, and midline. A burr hole was made at the injection coordinates—2 mm distal to the bregma and 2 mm from the midline, in the right hemisphere. 1 μL of the virus stock was injected at 50nl/minute, 1 μm into the cortex, using a microinjection syringe: Hamilton (80314: 10 μL, Model 701 RN SYR, 32 ga, 2 in, point style 3 needle), controlled by an UltraMicroPump with SYS-Micro4Controller (World Precision Instruments) and MPC-325 Multi-Micromanipulator system (Sutter Instruments). To prevent backflow of the viral volume, the needle was kept in place for 10 minutes after injection, withdrawn halfway, and allowed to rest for another 10 minutes before being fully withdrawn. The scalp was sutured using silk braided surgical sutures (Keebomed). The rats were treated with Enroflox 100 (Norbrook) and Carprofen (Carprieve, 50mg/ml) for a week post-surgery to promote recovery, as well as to prevent infection and inflammation.
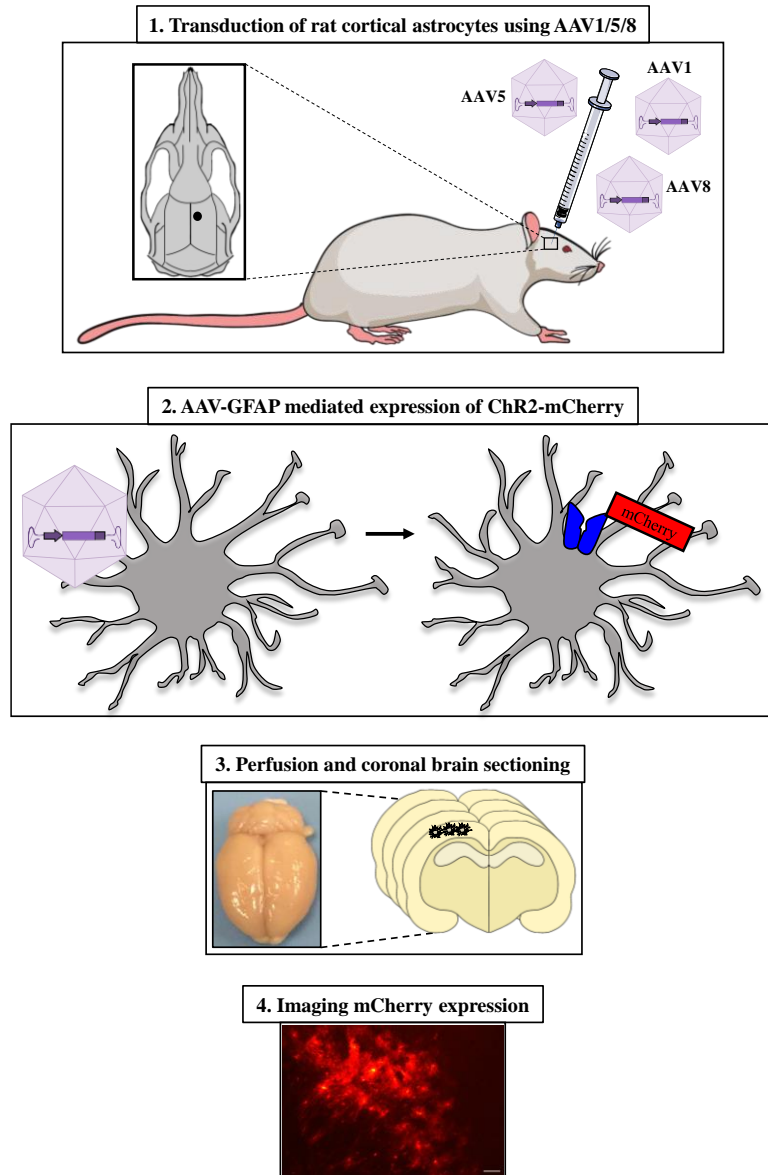
Figure 4-1 Experimental flow for studying rat cortical astrocyte transduction using various viral vector serotypes. Experimental steps including 1. Microinjection of serotypes 1,5 or 8 of the AAV-GFAP-ChR2(H134R)-mCherry virus targeting rat cortical astrocytes. Inset shows microinjection location (2mm posterior to the Bregma, 2mm from the midline). 2. Targeted expression of ChR2-mCherry on the GFAP[+] astrocyte. 3. Perfusion and coronal brain sectioning, 2 weeks post-surgery, and 4. mCherry expression analysis to determine serotype expression efficacy.

4.2.3 Tissue preparation

Two weeks after surgery, rats were deeply anesthetized under isoflurane anesthesia (5%, 1 L/min O2, 14.7 PSI) and transcardially perfused with 4% paraformaldehyde. Subsequently,

91

the brain was removed and placed in 4% PFA for 24 hours at 4°C. It was then transferred

to 30% sucrose/PBS for cryoprotection at 4°C. The target region of the brain was embedded

in Leica freezing medium and frozen at -80 °C. Coronal brain sections (30 μm thick) were

made using a Leica cryostat (CM1950), mounted on Fisher Superfrost Plus slides, and left

to dry overnight, before cover-slipping with Diamond Antifade Mountant (ThermoFisher

Scientific) and imaging (refer to Figure 4-1 for the stepwise procedure).

4.2.4 Quantitative analysis

To determine the viral spread of the various serotypes of the optogenetic construct AAV-

GFAP-hChR2(H134R)-mCherry targeting astrocytes, we quantified intracranial injections

of the virus (Sample size (n) = 5 rats/ serotype). The number of slices displaying mCherry

expression was multiplied by a factor of 30 (indicative of the slice thickness of 30 μm) to

obtain the final distance of spread of the virus in the brain. Transduced area per section was

measured using FIJI (Schindelin et al., 2012). Statistical tests were performed using

GraphPad Prism version 8.4.3. The summary data are presented as mean ± std.

(A)   **(B)**
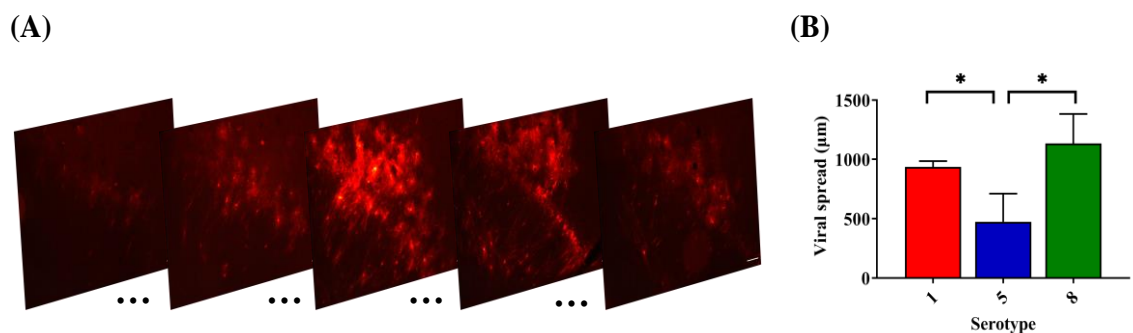
Figure 4-2 Quantification of serotype-based mCherry expression in the rat neocortex across coronal sections. (A) Representative images of AAV-GFAP-ChR2(H134R)-mCherry serotype 8 expression at 1) 1.69mm, 2) 1.78mm, 3) 2.02mm, 4) 2.29mm and 5) 2.41mm from the Bregma. **(B)** Quantification of the viral spread of the serotypes 1,5 and 8 (n = 5/ serotype). Average data are represented as mean ± std. 1-way

92

ANOVA, p<0.001, 95% CI. Tukey's multiple comparisons test reveals the significance of pairwise comparisons to be: Serotype 1 vs. 5 (**), Serotype 8 vs. 5 (***), Serotype 1 vs. 8 (ns). Scale bar – 100μm.

(A)   **(B)**
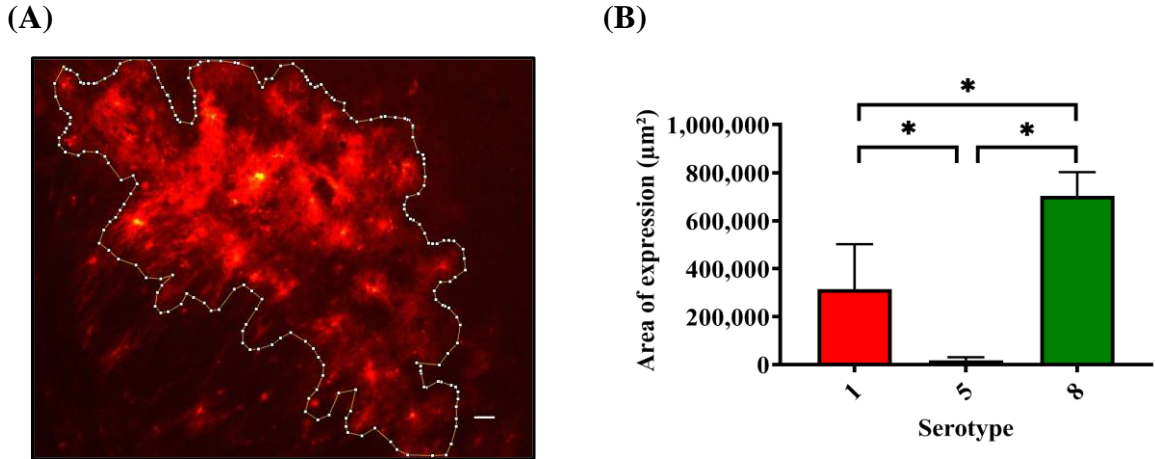
Figure 4-3 Quantification of radial expression of various AAV serotypes in the rat neocortex. (A) Representative image of an AAV8-transduced rat slice (enclosed within the highlighted bound area) **(B)** Quantification of the radial viral spread of the serotypes 1,5 and 8 (n = 5/ serotype). Average data are represented as mean ± std. Kruskal Wallis test, p<0.0001, 95% CI. Mann Whitney test reveals the significance of pairwise comparisons to be: Serotype 1 vs. 5 (*), Serotype 8 vs. 5 (**), Serotype 1 vs. 8 (*). Scale bar – 100μm.

4.3   RESULTS

Our experiments showed that there was a significant difference between serotypes 8, 5, and 1 (Figure 4-2), where serotype 5 had the least viral spread as compared to the others. After confirming normality of the data using the Shapiro-Wilkins test, a one-way ANOVA and Tukey's multiple comparisons test were conducted to establish statistical significance. To determine the radial spread of the serotypes of the optogenetic construct, we employed ImageJ to calculate the area of transduction. Traces of the area of the central slice of expression were drawn and quantified on the software. From our experiments, we observe that serotype 8 had the highest radial spread of the virus in the rat brain cortex, as compared to both serotypes 1 and 5 (Figure 4-3). Thus, for targeting astrocytes optogenetically using this construct, rAAV8 had the maximum transduction efficiency. The results were obtained by performing a Shapiro Wilkins test for normality, non-parametric ANOVA with a

Kruskal Wallis test, followed by a Welch's T-test between pairs of serotypes (significance declared at $p < 0.05$).

4.4   DISCUSSION

AAVs are single-stranded non-enveloped DNA viruses with capsids sized ~ 4.7 kb, making them among the smallest known viruses. They have been studied extensively to probe into their capabilities of gene delivery and therapy for neurological disorders (Ruitenberg, Eggers, Boer, & Verhaagen, 2002; Weinberg, Samulski, & McCown, 2013), with transduction efficacy varying greatly with each capsid, as detailed in their serotype. Studies suggest that transduction efficiency depends on the compatible serotype, target transduction area, and route of administration (Cearley & Wolfe, 2006; Zincarelli, Soltys, Rengo, & Rabinowitz, 2008). The evaluation of tropisms of AAV capsid serotypes has been performed in a plethora of organs in a variety of rodent models. Specifically, serotypes 2, 4, and 5 have transduced ependymal cells (Davidson et al., 2000), while 7, 8, 9, and rh10 transduced neurons (Cearley & Wolfe, 2006) via intracerebral injections in mice efficiently. Furthermore, serotypes 1, 2, 5 transduced the SN pars compacta showing high efficiency; additionally, 1 and 5 transduced the pars reticulata in the CNS of rats (Burger et al., 2004). Notably, even if the vectors contained the same genome, they exhibited markedly different patterns of transduction, owing to their serotype (Chakrabarty et al., 2013). A study by Yang *et al.* (Yang et al., 2002) details the difference in uptake of the genetic material via AAV delivery to the murine retina and elucidates how a shorter construct of the AAV2 serotype has a significantly higher uptake by the retina, as compared to a longer construct of AAV2.

94

Our study indicates that for optogenetic targeting of cortical astrocytes, serotype 8 had the most efficient expression, compared to the two other serotypes recommended to target brain cells (1 and 5). This is in accordance with the robust serotype 8 rAAV-mediated gene expression that has been observed and employed extensively non-optogenetic construct delivery to astrocytes in the rodent CNS. For example, Pignataro *et al.* studied rAAV8 for astrocyte-specific delivery of therapeutic genes in the CNS (Pignataro et al., 2017), while Klein et al. (Klein, Dayton, Tatom, Henderson, & Henning, 2008) demonstrated the use of AAV serotypes 8, 9, Rh10, and Rh43, with transduction efficiencies similar to that of AAV8. AAV8 and AAV7 vectors were also used for enhancing gene transfer efficiency in the murine striatum and in an orthotopic glioblastoma tumor model (Harding et al., 2006). Interestingly, a synthetic serotype AAVDJ8 (generated by modifying specific residues of AAV8) displayed a higher tropism to astrocytes compared to other serotypes (Hammond, Leek, Richman, & Tjalkens, 2017). It is noteworthy that use of the GFAP promoter resulted in predominantly astrocytic transduction (~88%) with AAV8 (Lawlor, Bland, Mouravlev, Young, & During, 2009), and there is high penetrance and almost complete specificity of gene delivery using AAV8-GFAP constructs to astrocytes (Adamsky et al., 2018). Future work building on our study can characterize and quantify via immunohistochemistry the percentage of each cell type transduced by serotypes of optogenetic construct employed in this study.

CHAPTER 5   CONCLUDING REMARKS

5.1   SUMMARY

The work presented in this dissertation provides a systematic characterization of a) induced increases in astrocytic Ca^{2+} due to varying light stimulation paradigms and b) optogenetic construct serotype transduction targeting astrocytes to implement optogenetics for inducing astrocytic Ca^{2+} increases in a controlled and tunable manner. In order to facilitate optogenetic intervention of astrocytes, we investigate light stimulation paradigms conducive for eliciting robust Ca^{2+} signaling. This was described in detail in this dissertation using *in situ*, *in silica,* and *in vivo* approaches and depicts how astrocytic Ca^{2+} signaling can be studied and modulated.

In Chapter 2, we discussed the development of a protocol to perform simultaneous optogenetics and Ca^{2+} imaging on neocortical astrocytes in adult murine brain slices. We standardized the protocol for brain extraction, sectioning, Rhod-2 AM loading, maintenance of slice health, and Ca^{2+} imaging during light stimulation. We also identified light paradigms capable of eliciting robust astrocytic Ca^{2+} signaling upon multiple stimulations. For a given T of 100s, we found that paradigm 20% gave the maximum astrocytic peak $\Delta F/F_0$, with robust recovery during multiple photo-stimulations.

In Chapter 3, our mathematical model helped us study light-induced Ca^{2+} responses in both a single and a network of homogenously/heterogeneously ChR2 expressing astrocytes and identify light stimulation paradigms for short and long-term stimulation. We quantified the effect of varying laser stimulation characterizations, as well as the sensitivity of the model

output to changes in the regulation kinetics of ChR2 photocurrent. The outlined model provides the insight necessary to identify stimulation paradigms ideal for controlling astrocytic Ca^{2+} activity and offers geneticists an efficient theoretical framework for an application-oriented design of new variants. Consistent with the experimental data, the model showed robust Ca^{2+} responses in the short-term stimulation paradigm chosen.

In Chapter 4, we discuss the serotype evaluation of the construct AAV-GFAP-hCHR2(H134R)-mCherry targeting astrocytes. Results show that serotype 8 had the maximum viral spread (in both tangential and radial directions) compared to serotypes 1 and 5 in neocortical astrocytes in the rat brain.

5.2   FUTURE DIRECTIONS

5.2.1   Acute slice work

Longitudinal studies for investigating neurodegenerative disorders like Alzheimer's disease, stroke, and Parkinson's disease employ mice across ages—young (<2 months), adults (2-14 months), and aged mice (>18 months) (J. Riera, Hatanaka, Uchida, et al., 2011; Rodriguez-Arellano, Parpura, Zorec, & Verkhratsky, 2016; Verkhratsky et al., 2014). The study of brain slices from adult mice is challenging due to astrocytic vulnerability pertaining to age-related toxicity and morphological factors. This is attributed to atrophy and high levels of oxidative stress, mainly due to the rapid depletion of cellular antioxidants, including ascorbate and reduced glutathione. Brain slices from these older mice are also more prone to insults during dissection leading to lower viability (Brahma, Forman, Stewart, Nicholson, & Rice, 2000; Matias et al., 2019). While this study focuses on slice preparation from mice aged 2-5 months, we encourage adopters to perceive this method as

work in progress towards imaging in even older mice. We believe that our study can serve as a guideline towards methodological improvements to curb deterioration and prolong slice viability when using mice >5 months.

It is crucial for studies that combine the use of ChR2 and Ca^{2+} imaging to choose a red-shifted Ca^{2+} indicator due to limited spectral availability, without a confounding effect between light stimulation and Ca^{2+} indicator excitation (refer to Figure 2-1C). To evaluate astrocytic Ca^{2+} responses, we utilize Rhod-2 AM—a robust red-shifted indicator. Rhod-2 AM has been extensively characterized in acute brain slice studies probing several cell types across young mice cohorts, predominantly juvenile and young adults <2 months (He et al., 2012; W. Sun et al., 2013). It is noteworthy that recently, a highly sensitive Ca^{2+} indicator in the red spectrum—Calbryte 590 AM has been used in vivo to detect neuronal dendritic calcium spikes (Suzuki & Larkum, 2017). Although this is pending optimization for use in acute brain slice studies, it holds the potential for obtaining Ca^{2+} responses with enhanced sensitivity and a higher signal-to-noise ratio. Other tools like genetically encoded calcium indicators, specifically R-Camps, can be further engineered to target astrocytes to facilitate simultaneous optogenetic stimulation and Ca^{2+} imaging (Akerboom et al., 2013; Inoue et al., 2015). Also, it is noteworthy to mention that the protocol discussed in this dissertation can also be employed in adult mice brain slice preparations which have been virally injected for delivery of ChR2 to cortical astrocytes.

It is important to note that usage of a 2-photon microscope would aid in the demarcation of Ca^{2+} responses from astrocytic soma versus processes and would facilitate recording for longer periods of time with reduced photobleaching. Longer recording times would provide

more information for various other T-δ combinations and help understand the effect of a rest period after a stimulation cycle, even in cases of 95%. For example, if resting after 1-2 stimulations could help revive the lack of spiking as observed in Figure 2-5C, if there enough time for ChR2(C128S) to go to the dark adaptive state D470 (Figure 2-6).

5.2.2   Mathematical modeling

ChR2 is a non-selective cation channel, with varying permeability for Na^+, K^+, Ca^{2+}, and H^+ across different variants (John Y Lin, 2012; J. Y. Lin et al., 2009). Cationic entry has shown to induce membrane depolarization which can activate voltage-gated calcium channels, although their functional role in astrocytes is a subject of ongoing debate (Agulhon et al., 2012), and result in a further influx of calcium, potentially activating large conductance calcium activated potassium currents (Mager, Wood, & Bamberg, 2017). Activation of these channels changes the membrane potential of the cell and can thus affect the magnitude of the ChR2 photocurrent since ChR2 is V_m-sensitive. Our model does not include the dynamics of other major ionic species and does not account for the abovementioned dependencies on the membrane potential. We have also not explicitly accounted for other intracellular compartments, e.g., microdomains and mitochondria, involved in the calcium dynamics of astrocytes. In a recent study (Moshkforoush, Ashenagar, Tsoukias, & Alevriadou, 2019), it was demonstrated that the inclusion of microdomains and mitochondria compartments reduced the calcium and IP_3 levels required for the activation of IP_3Rs in non-excitable cells and can thus affect the ChR2-induced calcium signaling in our model. Another limitation of the model is that, in this study, we adopted the Langevin approach outlined in ref. (Shuai & Jung, 2002) for the

implementation of stochasticity in the dynamics of the IP$_3$R channels and have not accounted for the detailed diffusion of calcium ions within and between IP$_3$R clusters. This would require a system of partial differential equations as demonstrated in ref. (A. Skupin et al., 2010). In this study, we sought to provide a minimalistic theoretical framework that can readily be employed by researchers for the investigation of light-induced Ca^{2+} responses in astrocytes. Combination of the presented model with more detailed models as in (Savtchenko et al., 2018) and (Lallouette, De Pittà, & Berry, 2019), where exhaustive geometry and dynamics of various ionic species are accounted for, can enhance our understanding of the intricacies of the behavior of astrocytes and their response to light.

5.2.3 *In vivo* experiments

Viral vector transduction poses future challenges as a consequence of heterogeneities in cell expression and nuisance neuroinflammation triggered by microinjection protocols. In addition to this, evaluating transduction approaches also holds future applications for clinical translational work. To set the initial platform by using an optimal transduction strategy, it is important to evaluate via future work, not pertinent to this dissertation, heterogeneity in cell expression from transduction approaches and to disentangle any neuroinflammatory processes generated due to microinjection. Recently, Schober *et al.* (Schober et al., 2016) evaluated the transduction efficiency of serotypes 2 and 6 in non-optogenetic constructs in the rat brain cortex (*in vivo*) and found that serotype 6 efficiently transduced astrocytes. The implications of these modifications and the evaluation of a broader range of serotypes of the optogenetic construct targeting astrocytes is a future direction of this study. We recognize a gap in literature wherein there is no systematic

evaluation available for elucidating the most efficient AAV capsid serotype for the optogenetic construct targeting astrocytes in the rat brain cortex and hence aimed to provide a foundation for the characterization of the optogenetic construct AAV-GFAP-ChR2(H134R)-mCherry, specifically for the light-induced intervention of astrocyte activity thereby establishing future robust control and detailed study of astrocytic Ca^{2+} dynamics and downstream effects.

Overall, this dissertation serves to set the foundation for characterizing astrocytic Ca^{2+} responses to various light stimulation paradigms, studying the implications of light stimulation, short and long-term, and characterizing transduction patterns to achieve regulated and controlled manipulation of astrocytes using optogenetics.

REFERENCES

Adamantidis, A. R., Zhang, F., de Lecea, L., & Deisseroth, K. (2014). Optogenetics: opsins and optical interfaces in neuroscience. *Cold Spring Harb Protoc, 2014*(8), 815-822. doi:10.1101/pdb.top083329

Adamsky, A., Kol, A., Kreisel, T., Doron, A., Ozeri-Engelhard, N., Melcer, T., . . . Goshen, I. (2018). Astrocytic Activation Generates De Novo Neuronal Potentiation and Memory Enhancement. *Cell, 174*(1), 59-71 e14. doi:10.1016/j.cell.2018.05.002

Agulhon, C., Sun, M. Y., Murphy, T., Myers, T., Lauderdale, K., & Fiacco, T. A. (2012). Calcium Signaling and Gliotransmission in Normal vs. Reactive Astrocytes. *Front Pharmacol, 3*, 139. doi:10.3389/fphar.2012.00139

Akerboom, J., Carreras Calderon, N., Tian, L., Wabnig, S., Prigge, M., Tolo, J., . . . Looger, L. L. (2013). Genetically encoded calcium indicators for multi-color neural activity imaging and combination with optogenetics. *Front Mol Neurosci, 6*, 2. doi:10.3389/fnmol.2013.00002

Araque, A., Carmignoto, G., Haydon, P. G., Oliet, S. H., Robitaille, R., & Volterra, A. (2014). Gliotransmitters travel in time and space. *Neuron, 81*(4), 728-739. doi:10.1016/j.neuron.2014.02.007

Araque, A., Parpura, V., Sanzgiri, R. P., & Haydon, P. G. (1998). Glutamate-dependent astrocyte modulation of synaptic transmission between cultured hippocampal neurons. *European Journal of Neuroscience, 10*(6), 2129-2142. doi:10.1046/j.1460-9568.1998.00221.x

Araque, A., Parpura, V., Sanzgiri, R. P., & Haydon, P. G. (1999). Tripartite synapses: glia, the unacknowledged partner. *Trends Neurosci, 22*(5), 208-215. doi:10.1016/s0166-2236(98)01349-6

Arcuino, G., Lin, J. H., Takano, T., Liu, C., Jiang, L., Gao, Q., . . . Nedergaard, M. (2002). Intercellular calcium signaling mediated by point-source burst release of ATP. *Proc Natl Acad Sci U S A, 99*(15), 9840-9845. doi:10.1073/pnas.152588599

Aronica, E., Ravizza, T., Zurolo, E., & Vezzani, A. (2012). Astrocyte immune responses in epilepsy. *Glia, 60*(8), 1258-1268. doi:10.1002/glia.22312

Aschauer, D. F., Kreuz, S., & Rumpel, S. (2013). Analysis of transduction efficiency, tropism and axonal transport of AAV serotypes 1, 2, 5, 6, 8 and 9 in the mouse brain. *PloS one, 8*(9), e76310. doi:10.1371/journal.pone.0076310

Attwell, D., Buchan, A. M., Charpak, S., Lauritzen, M., Macvicar, B. A., & Newman, E. A. (2010). Glial and neuronal control of brain blood flow. *Nature, 468*(7321), 232-243. doi:10.1038/nature09613

Balachandar, L., Montejo, K. A., Castano, E., Perez, M., Moncion, C., Chambers, J. W., . . . Diaz, J. R. (2020). Simultaneous Ca(2+) Imaging and Optogenetic Stimulation of Cortical Astrocytes in Adult Murine Brain Slices. *Curr Protoc Neurosci, 94*(1), e110. doi:10.1002/cpns.110

Bazargani, N., & Attwell, D. (2016). Astrocyte calcium signaling: the third wave. *Nature neuroscience, 19*(2), 182-189. doi:10.1038/nn.4201

Bedner, P., Dupper, A., Hüttmann, K., Müller, J., Herde, M. K., Dublin, P., . . . Haas, C. A. (2015). Astrocyte uncoupling as a cause of human temporal lobe epilepsy. *Brain, 138*(5), 1208-1222.

Bernardinelli, Y., Muller, D., & Nikonenko, I. (2014). Astrocyte-synapse structural plasticity. *Neural Plast, 2014*, 232105. doi:10.1155/2014/232105

Berndt, A., Schoenenberger, P., Mattis, J., Tye, K. M., Deisseroth, K., Hegemann, P., & Oertner, T. G. (2011). High-efficiency channelrhodopsins for fast neuronal stimulation at low light levels. *Proceedings of the National Academy of Sciences, 108*(18), 7595-7600. doi:10.1073/pnas.1017210108

Berndt, A., Yizhar, O., Gunaydin, L. A., Hegemann, P., & Deisseroth, K. (2009). Bi-stable neural state switches. *Nat Neurosci, 12*(2), 229-234. doi:10.1038/nn.2247

Bonder, D. E., & McCarthy, K. D. (2014). Astrocytic Gq-GPCR-linked IP3R-dependent Ca2+ signaling does not mediate neurovascular coupling in mouse visual cortex in vivo. *J Neurosci, 34*(39), 13139-13150. doi:10.1523/JNEUROSCI.2591-14.2014

Brahma, B., Forman, R. E., Stewart, E. E., Nicholson, C., & Rice, M. E. (2000). Ascorbate inhibits edema in brain slices. *J Neurochem, 74*(3), 1263-1270. doi:10.1046/j.1471-4159.2000.741263.x

Buning, H., Huber, A., Zhang, L., Meumann, N., & Hacker, U. (2015). Engineering the AAV capsid to optimize vector-host-interactions. *Curr Opin Pharmacol, 24*, 94-104. doi:10.1016/j.coph.2015.08.002

Burda, J. E., Bernstein, A. M., & Sofroniew, M. V. (2016). Astrocyte roles in traumatic brain injury. *Experimental neurology, 275*, 305-315. doi:10.1016/j.expneurol.2015.03.020

Burger, C., Gorbatyuk, O. S., Velardo, M. J., Peden, C. S., Williams, P., Zolotukhin, S., . . . Muzyczka, N. (2004). Recombinant AAV viral vectors pseudotyped with viral capsids from serotypes 1, 2, and 5 display differential efficiency and cell tropism after delivery to different regions of the central nervous system. *Mol Ther, 10*(2), 302-317. doi:10.1016/j.ymthe.2004.05.024

Buskila, Y., Breen, P. P., Tapson, J., van Schaik, A., Barton, M., & Morley, J. W. (2014). Extending the viability of acute brain slices. *Sci Rep, 4*(1), 5309. doi:10.1038/srep05309

Cearley, C. N., & Wolfe, J. H. (2006). Transduction characteristics of adeno-associated virus vectors expressing cap serotypes 7, 8, 9, and Rh10 in the mouse brain. *Mol Ther, 13*(3), 528-537. doi:10.1016/j.ymthe.2005.11.015

Chakrabarty, P., Rosario, A., Cruz, P., Siemienski, Z., Ceballos-Diaz, C., Crosby, K., . . . Levites, Y. (2013). Capsid serotype and timing of injection determines AAV transduction in the neonatal mice brain. *PloS one, 8*(6), e67680. doi:10.1371/journal.pone.0067680

Charles, A. C. (1994). Glia-neuron intercellular calcium signaling. *Dev Neurosci, 16*(3-4), 196-206. doi:10.1159/000112107

Charles, A. C., Merrill, J. E., Dirksen, E. R., & Sandersont, M. J. (1991). Intercellular signaling in glial cells: calcium waves and oscillations in response to mechanical stimulation and glutamate. *Neuron, 6*(6), 983-992.

Chen, Y., Mancuso, J. J., Zhao, Z., Li, X., Cheng, J., Roman, G., & Wong, S. T. (2013). Vasodilation by in vivo activation of astrocyte endfeet via two-photon calcium uncaging as a strategy to prevent brain ischemia. *Journal of biomedical optics, 18*(12), 126012. doi:10.1117/1.JBO.18.12.126012

Cornell-Bell, A. H., Finkbeiner, S. M., Cooper, M. S., & Smith, S. J. (1990). Glutamate induces calcium waves in cultured astrocytes: long-range glial signaling. *Science, 247*(4941), 470-473.

Dani, J. W., Chernjavsky, A., & Smith, S. J. (1992). Neuronal activity triggers calcium waves in hippocampal astrocyte networks. *Neuron, 8*(3), 429-440. doi:10.1016/0896-6273(92)90271-e

Davidson, B. L., Stein, C. S., Heth, J. A., Martins, I., Kotin, R. M., Derksen, T. A., . . . Chiorini, J. A. (2000). Recombinant adeno-associated virus type 2, 4, and 5 vectors: transduction of variant cell types and regions in the mammalian central nervous system. *Proc Natl Acad Sci U S A, 97*(7), 3428-3432. doi:10.1073/pnas.050581197

De Carlos, J. A., & Borrell, J. (2007). A historical reflection of the contributions of Cajal and Golgi to the foundations of neuroscience. *Brain Res Rev, 55*(1), 8-16. doi:10.1016/j.brainresrev.2007.03.010

De Young, G. W., & Keizer, J. (1992). A single-pool inositol 1,4,5-trisphosphate-receptor-based model for agonist-stimulated oscillations in Ca2+ concentration. *Proc Natl Acad Sci U S A, 89*(20), 9895-9899. doi:10.1073/pnas.89.20.9895

Deisseroth, K. (2015). Optogenetics: 10 years of microbial opsins in neuroscience. *Nat Neurosci, 18*(9), 1213-1225. doi:10.1038/nn.4091

Deshmukh, A., Leichner, J., Bae, J., Song, Y., Valdés-Hernández, P. A., Lin, W.-C., & Riera, J. J. (2018). Histological Characterization of the Irritative Zones in Focal Cortical

Dysplasia Using a Preclinical Rat Model. *Frontiers in cellular neuroscience, 12*. doi:10.3389/fncel.2018.00052.

Devinsky, O., Vezzani, A., Najjar, S., De Lanerolle, N. C., & Rogawski, M. A. (2013). Glia and epilepsy: excitability and inflammation. *Trends in neurosciences, 36*(3), 174-184.

Do Carmo, S., & Cuello, A. C. (2013). Modeling Alzheimer's disease in transgenic rats. *Mol Neurodegener, 8*(1), 37. doi:10.1186/1750-1326-8-37

Durkee, C. A., Covelo, A., Lines, J., Kofuji, P., Aguilar, J., & Araque, A. (2019). Gi/o protein-coupled receptors inhibit neurons but activate astrocytes and stimulate gliotransmission. *Glia, 67*(6), 1076-1093. doi:10.1002/glia.23589

Ellis, E., McKinney, J., Willoughby, K., Liang, S., & Povlishock, J. (1995). A new model for rapid stretch-induced injury of cells in culture: characterization of the model using astrocytes. *Journal of neurotrauma, 12*(3), 325-339.

Eng, L. F., Ghirnikar, R. S., & Lee, Y. L. (2000). Glial fibrillary acidic protein: GFAP-thirty-one years (1969-2000). *Neurochem Res, 25*(9-10), 1439-1451. doi:10.1023/a:1007677003387

Fatatis, A., & Russell, J. T. (1992). Spontaneous changes in intracellular calcium concentration in type I astrocytes from rat cerebral cortex in primary culture. *Glia, 5*(2), 95-104. doi:10.1002/glia.440050203

Fenno, L., Yizhar, O., & Deisseroth, K. (2011). The development and application of optogenetics. *Annu Rev Neurosci, 34*, 389-412. doi:10.1146/annurev-neuro-061010-113817

Fiacco, T. A., & McCarthy, K. D. (2006). Astrocyte calcium elevations: properties, propagation, and effects on brain signaling. *Glia, 54*(7), 676-690. doi:10.1002/glia.20396

Fiacco, T. A., & McCarthy, K. D. (2018). Multiple lines of evidence indicate that gliotransmission does not occur under physiological conditions. *Journal of Neuroscience, 38*(1), 3-13. doi:10.1523/JNEUROSCI.0016-17.2017

Figueiredo, M., Lane, S., Stout, R. F., Jr., Liu, B., Parpura, V., Teschemacher, A. G., & Kasparov, S. (2014). Comparative analysis of optogenetic actuators in cultured astrocytes. *Cell Calcium, 56*(3), 208-214. doi:10.1016/j.ceca.2014.07.007

Figueiredo, M., Lane, S., Tang, F., Liu, B. H., Hewinson, J., Marina, N., . . . Kasparov, S. (2011). Optogenetic experimentation on astrocytes. *Exp Physiol, 96*(1), 40-50. doi:10.1113/expphysiol.2010.052597

Filosa, J. A., Morrison, H. W., Iddings, J. A., Du, W., & Kim, K. J. (2016). Beyond neurovascular coupling, role of astrocytes in the regulation of vascular tone. *Neuroscience, 323*, 96-109. doi:10.1016/j.neuroscience.2015.03.064

Fleischer, W., Theiss, S., Slotta, J., Holland, C., & Schnitzler, A. (2015). High-frequency voltage oscillations in cultured astrocytes. *Physiological reports, 3*(5).

Girouard, H., & Iadecola, C. (2006). Neurovascular coupling in the normal brain and in hypertension, stroke, and Alzheimer disease. *Journal of applied physiology, 100*(1), 328-335.

Gradinaru, V., Mogri, M., Thompson, K. R., Henderson, J. M., & Deisseroth, K. (2009). Optical deconstruction of parkinsonian neural circuitry. *Science, 324*(5925), 354-359. doi:10.1126/science.1167093

Guerra-Gomes, S., Sousa, N., Pinto, L., & Oliveira, J. F. (2017). Functional Roles of Astrocyte Calcium Elevations: From Synapses to Behavior. *Front Cell Neurosci, 11*, 427. doi:10.3389/fncel.2017.00427

Gunaydin, L. A., Yizhar, O., Berndt, A., Sohal, V. S., Deisseroth, K., & Hegemann, P. (2010). Ultrafast optogenetic control. *Nat Neurosci, 13*(3), 387-392. doi:10.1038/nn.2495

Guthrie, P. B., Knappenberger, J., Segal, M., Bennett, M. V., Charles, A. C., & Kater, S. B. (1999). ATP released from astrocytes mediates glial calcium waves. *J Neurosci, 19*(2), 520-528. doi:10.1523/JNEUROSCI.19-02-00520.1999

Guthrie, P. B., Knappenberger, J., Segal, M., Bennett, M. V., Charles, A. C., & Kater, S. B. (1999). ATP released from astrocytes mediates glial calcium waves. *Journal of Neuroscience, 19*(2), 520-528.

Hamad, M. I., Krause, M., & Wahle, P. (2015). Improving AM ester calcium dye loading efficiency. *J Neurosci Methods, 240*, 48-60. doi:10.1016/j.jneumeth.2014.11.010

Hamby, M. E., & Sofroniew, M. V. (2010). Reactive astrocytes as therapeutic targets for CNS disorders. *Neurotherapeutics, 7*(4), 494-506.

Hamilton, N., Vayro, S., Kirchhoff, F., Verkhratsky, A., Robbins, J., Gorecki, D. C., & Butt, A. M. (2008). Mechanisms of ATP- and glutamate-mediated calcium signaling in white matter astrocytes. *Glia, 56*(7), 734-749. doi:10.1002/glia.20649

Hammond, S. L., Leek, A. N., Richman, E. H., & Tjalkens, R. B. (2017). Cellular selectivity of AAV serotypes for gene delivery in neurons and astrocytes by neonatal intracerebroventricular injection. *PloS one, 12*(12), e0188830. doi:10.1371/journal.pone.0188830

Hanisch, U. K. (2002). Microglia as a source and target of cytokines. *Glia, 40*(2), 140-155. doi:10.1002/glia.10161

Harding, T. C., Dickinson, P. J., Roberts, B. N., Yendluri, S., Gonzalez-Edick, M., Lecouteur, R. A., & Jooss, K. U. (2006). Enhanced gene transfer efficiency in the murine

striatum and an orthotopic glioblastoma tumor model, using AAV-7-and AAV-8-pseudotyped vectors. *Human gene therapy, 17*(8), 807-820. doi:10.1089/hum.2006.17.807

Hassinger, T., Guthrie, P., Atkinson, P., Bennett, M. V., & Kater, S. (1996). An extracellular signaling component in propagation of astrocytic calcium waves. *Proceedings of the National Academy of Sciences, 93*(23), 13268-13273.

He, L., Linden, D. J., & Sapirstein, A. (2012). Astrocyte inositol triphosphate receptor type 2 and cytosolic phospholipase A2 alpha regulate arteriole responses in mouse neocortical brain slices. *PloS one, 7*(8), e42194. doi:10.1371/journal.pone.0042194

Heuser, K., Nome, C. G., Pettersen, K. H., Åbjørsbråten, K. S., Jensen, V., Tang, W., . . . Enger, R. (2018). Ca2+ Signals in Astrocytes Facilitate Spread of Epileptiform Activity. *Cerebral Cortex, 28*(11), 4036-4048. doi:10.1093/cercor/bhy196

Hirase, H., Qian, L., Bartho, P., & Buzsaki, G. (2004). Calcium dynamics of cortical astrocytic networks in vivo. *PLoS Biol, 2*(4), E96. doi:10.1371/journal.pbio.0020096

Hohn, S., Dallerac, G., Faure, A., Urbach, Y. K., Nguyen, H. P., Riess, O., . . . Doyere, V. (2011). Behavioral and in vivo electrophysiological evidence for presymptomatic alteration of prefrontostriatal processing in the transgenic rat model for huntington disease. *J Neurosci, 31*(24), 8986-8997. doi:10.1523/JNEUROSCI.1238-11.2011

Iadecola, C. (2017). The neurovascular unit coming of age: a journey through neurovascular coupling in health and disease. *Neuron, 96*(1), 17-42. doi:10.1016/j.neuron.2017.07.030

Inoue, M., Takeuchi, A., Horigane, S., Ohkura, M., Gengyo-Ando, K., Fujii, H., . . . Bito, H. (2015). Rational design of a high-affinity, fast, red calcium indicator R-CaMP2. *Nat Methods, 12*(1), 64-70. doi:10.1038/nmeth.3185

Jeremic, A., Jeftinija, K., Stevanovic, J., Glavaski, A., & Jeftinija, S. (2001). ATP stimulates calcium-dependent glutamate release from cultured astrocytes. *Journal of neurochemistry, 77*(2), 664-675.

Jimenez, J., & Ozaki, T. (2003). Local linearization filters for non-linear continuous-discrete state space models with multiplicative noise. *International Journal of Control, 76*(12), 1159-1170. doi:10.1080/0020717031000138214

Kettenmann, H., & Verkhratsky, A. (2008). Neuroglia: the 150 years after. *Trends Neurosci, 31*(12), 653-659. doi:10.1016/j.tins.2008.09.003

Khakh, B. S., & McCarthy, K. D. (2015). Astrocyte calcium signaling: from observations to functions and the challenges therein. *Cold Spring Harb Perspect Biol, 7*(4), a020404. doi:10.1101/cshperspect.a020404

Klein, R. L., Dayton, R. D., Tatom, J. B., Henderson, K. M., & Henning, P. P. (2008). AAV8, 9, Rh10, Rh43 vector gene transfer in the rat brain: effects of serotype, promoter and purification method. *Mol Ther, 16*(1), 89-96. doi:10.1038/sj.mt.6300331

Kleinlogel, S., Feldbauer, K., Dempski, R. E., Fotis, H., Wood, P. G., Bamann, C., & Bamberg, E. (2011). Ultra light-sensitive and fast neuronal activation with the Ca(2)+-permeable channelrhodopsin CatCh. *Nat Neurosci, 14*(4), 513-518. doi:10.1038/nn.2776

Koerber, J. T., Klimczak, R., Jang, J. H., Dalkara, D., Flannery, J. G., & Schaffer, D. V. (2009). Molecular evolution of adeno-associated virus for enhanced glial gene delivery. *Mol Ther, 17*(12), 2088-2095. doi:10.1038/mt.2009.184

Krook-Magnuson, E., Ledri, M., Soltesz, I., & Kokaia, M. (2014). How might novel technologies such as optogenetics lead to better treatments in epilepsy? In *Issues in Clinical Epileptology: A View from the Bench* (pp. 319-336): Springer.

Kuchibhotla, K. V., Lattarulo, C. R., Hyman, B. T., & Bacskai, B. J. (2009). Synchronous hyperactivity and intercellular calcium waves in astrocytes in Alzheimer mice. *Science, 323*(5918), 1211-1215. doi:10.1126/science.1169096

Kuhlman, S. J., & Huang, Z. J. (2008). High-resolution labeling and functional manipulation of specific neuron types in mouse brain by Cre-activated viral gene expression. *PloS one, 3*(4), e2005.

Kunkler, P. E., & Kraig, R. P. (1998). Calcium waves precede electrophysiological changes of spreading depression in hippocampal organ cultures. *Journal of Neuroscience, 18*(9), 3416-3425. doi:10.1523/JNEUROSCI.18-09-03416.1998

Lallouette, J., De Pittà, M., & Berry, H. (2019). Astrocyte networks and intercellular calcium propagation. In *Computational Glioscience* (pp. 177-210): Springer.

Lawlor, P. A., Bland, R. J., Mouravlev, A., Young, D., & During, M. J. (2009). Efficient gene delivery and selective transduction of glial cells in the mammalian brain by AAV serotypes isolated from nonhuman primates. *Mol Ther, 17*(10), 1692-1702. doi:10.1038/mt.2009.170

Li, Y. X., & Rinzel, J. (1994). Equations for InsP3 receptor-mediated [Ca2+]i oscillations derived from a detailed kinetic model: a Hodgkin-Huxley like formalism. *J Theor Biol, 166*(4), 461-473. doi:10.1006/jtbi.1994.1041

Lin, J. Y. (2012). Optogenetic excitation of neurons with channelrhodopsins: light instrumentation, expression systems, and channelrhodopsin variants. In *Progress in brain research* (Vol. 196, pp. 29-47): Elsevier.

Lin, J. Y., Lin, M. Z., Steinbach, P., & Tsien, R. Y. (2009). Characterization of engineered channelrhodopsin variants with improved properties and kinetics. *Biophys J, 96*(5), 1803-1814. doi:10.1016/j.bpj.2008.11.034

Lind, B. L., Brazhe, A. R., Jessen, S. B., Tan, F. C., & Lauritzen, M. J. (2013). Rapid stimulus-evoked astrocyte Ca2+ elevations and hemodynamic responses in mouse somatosensory cortex in vivo. *Proc Natl Acad Sci U S A, 110*(48), E4678-4687. doi:10.1073/pnas.1310065110

Lopez-Hidalgo, M., Kellner, V., & Schummers, J. (2017). Astrocyte Calcium Responses to Sensory Input: Influence of Circuit Organization and Experimental Factors. *Front Neural Circuits, 11*, 16. doi:10.3389/fncir.2017.00016

Losi, G., Cammarota, M., & Carmignoto, G. (2012). The role of astroglia in the epileptic brain. *Frontiers in pharmacology, 3*, 132.

Machler, P., Wyss, M. T., Elsayed, M., Stobart, J., Gutierrez, R., von Faber-Castell, A., . . . Weber, B. (2016). In Vivo Evidence for a Lactate Gradient from Astrocytes to Neurons. *Cell Metab, 23*(1), 94-102. doi:10.1016/j.cmet.2015.10.010

Mager, T., Wood, P. G., & Bamberg, E. (2017). Optogenetic control of Ca2+ and voltage-dependent large conductance (BK) potassium channels. *Journal of Molecular Biology, 429*(6), 911-921. doi:10.1016/j.jmb.2017.02.004

Magistretti, P. J., & Allaman, I. (2018). Lactate in the brain: from metabolic end-product to signalling molecule. *Nat Rev Neurosci, 19*(4), 235-249. doi:10.1038/nrn.2018.19

Mak, D. O., & Foskett, J. K. (2015). Inositol 1,4,5-trisphosphate receptors in the endoplasmic reticulum: A single-channel point of view. *Cell Calcium, 58*(1), 67-78. doi:10.1016/j.ceca.2014.12.008

Maragakis, N. J., & Rothstein, J. D. (2006). Mechanisms of Disease: astrocytes in neurodegenerative disease. *Nat Clin Pract Neurol, 2*(12), 679-689. doi:10.1038/ncpneuro0355

Marino, S., Hogue, I. B., Ray, C. J., & Kirschner, D. E. (2008). A methodology for performing global uncertainty and sensitivity analysis in systems biology. *J Theor Biol, 254*(1), 178-196. doi:10.1016/j.jtbi.2008.04.011

Masamoto, K., Unekawa, M., Watanabe, T., Toriumi, H., Takuwa, H., Kawaguchi, H., . . . Suzuki, N. (2015). Unveiling astrocytic control of cerebral blood flow with optogenetics. *Sci Rep, 5*, 11455. doi:10.1038/srep11455

Matias, I., Morgado, J., & Gomes, F. C. A. (2019). Astrocyte Heterogeneity: Impact to Brain Aging and Disease. *Front Aging Neurosci, 11*, 59. doi:10.3389/fnagi.2019.00059

McCown, T. J., Xiao, X., Li, J., Breese, G. R., & Samulski, R. J. (1996). Differential and persistent expression patterns of CNS gene transfer by an adeno-associated virus (AAV) vector. *Brain Res, 713*(1-2), 99-107. doi:10.1016/0006-8993(95)01488-8

McKay, M. D., Beckman, R. J., & Conover, W. J. (2000). A comparison of three methods for selecting values of input variables in the analysis of output from a computer code. *Technometrics, 42*(1), 55-61. doi:10.2307/1268522

Monai, H., & Hirase, H. (2016). Astrocytic calcium activation in a mouse model of tDCS-Extended discussion. *Neurogenesis (Austin), 3*(1), e1240055. doi:10.1080/23262133.2016.1240055

Monai, H., Ohkura, M., Tanaka, M., Oe, Y., Konno, A., Hirai, H., . . . Hirase, H. (2016). Calcium imaging reveals glial involvement in transcranial direct current stimulation-induced plasticity in mouse brain. *Nat Commun, 7*(1), 11100. doi:10.1038/ncomms11100

Moshkforoush, A., Ashenagar, B., Tsoukias, N. M., & Alevriadou, B. R. (2019). Modeling the role of endoplasmic reticulum-mitochondria microdomains in calcium dynamics. *Sci Rep, 9*(1), 17072. doi:10.1038/s41598-019-53440-7

Moshkforoush, A., Balachandar, L., Moncion, C., Montejo, K. A., & Riera, J. (2021). Unraveling ChR2-driven stochastic Ca2+ dynamics in astrocytes: A call for new interventional paradigms. *PLoS Comput Biol, 17*(2), e1008648. doi:10.1371/journal.pcbi.1008648

Nayak, S., & Herzog, R. W. (2010). Progress and prospects: immune responses to viral vectors. *Gene therapy, 17*(3), 295.

Nayak, S., & Herzog, R. W. (2010). Progress and prospects: immune responses to viral vectors. *Gene Ther, 17*(3), 295-304. doi:10.1038/gt.2009.148

Nedergaard, M., Cooper, A. J., & Goldman, S. A. (1995). Gap junctions are required for the propagation of spreading depression. *Journal of neurobiology, 28*(4), 433-444.

Nett, W. J., Oloff, S. H., & Mccarthy, K. D. (2002). Hippocampal astrocytes in situ exhibit calcium oscillations that occur independent of neuronal activity. *Journal of neurophysiology, 87*(1), 528-537. doi:10.1152/jn.00268.2001

Nikolic, K., Grossman, N., Grubb, M. S., Burrone, J., Toumazou, C., & Degenaar, P. (2009). Photocycles of channelrhodopsin-2. *Photochem Photobiol, 85*(1), 400-411. doi:10.1111/j.1751-1097.2008.00460.x

Nizar, K., Uhlirova, H., Tian, P., Saisan, P. A., Cheng, Q., Reznichenko, L., . . . MacDonald, C. L. (2013). In vivo stimulus-induced vasodilation occurs without IP3 receptor activation and may precede astrocytic calcium increase. *Journal of Neuroscience, 33*(19), 8411-8422. doi: 10.1523/JNEUROSCI.3285-12.2013

Ozaki, T. (1993). A local linearization approach to nonlinear filtering. *International Journal of Control, 57*(1), 75-96. doi:10.1080/00207179308934379

Parpura, V., Basarsky, T. A., Liu, F., Jeftinija, K., Jeftinija, S., & Haydon, P. G. (1994). Glutamate-mediated astrocyte-neuron signalling. *Nature, 369*(6483), 744-747. doi:10.1038/369744a0

Parri, H. R., Gould, T. M., & Crunelli, V. (2001). Spontaneous astrocytic Ca 2+ oscillations in situ drive NMDAR-mediated neuronal excitation. *Nature neuroscience, 4*(8), 803-812. doi:10.1038/90507

Pascual, O., Ben Achour, S., Rostaing, P., Triller, A., & Bessis, A. (2012). Microglia activation triggers astrocyte-mediated modulation of excitatory neurotransmission. *Proc Natl Acad Sci U S A, 109*(4), E197-205. doi:10.1073/pnas.1111098109

Pascual, O., Casper, K. B., Kubera, C., Zhang, J., Revilla-Sanchez, R., Sul, J. Y., . . . Haydon, P. G. (2005). Astrocytic purinergic signaling coordinates synaptic networks. *Science, 310*(5745), 113-116. doi:10.1126/science.1116916

Pekny, M., & Pekna, M. (2014). Astrocyte reactivity and reactive astrogliosis: costs and benefits. *Physiol Rev, 94*(4), 1077-1098. doi:10.1152/physrev.00041.2013

Pekny, M., & Pekna, M. (2016). Reactive gliosis in the pathogenesis of CNS diseases. *Biochim Biophys Acta, 1862*(3), 483-491. doi:10.1016/j.bbadis.2015.11.014

Peters, O., Schipke, C. G., Hashimoto, Y., & Kettenmann, H. (2003). Different mechanisms promote astrocyte Ca2+ waves and spreading depression in the mouse neocortex. *Journal of Neuroscience, 23*(30), 9888-9896. doi:10.1523/JNEUROSCI.23-30-09888.2003

Petrosyan, H., Alessi, V., Singh, V., Hunanyan, A., Levine, J., & Arvanian, V. (2014). Transduction efficiency of neurons and glial cells by AAV-1,-5,-9,-rh10 and-hu11 serotypes in rat spinal cord following contusion injury. *Gene therapy, 21*(12), 991-1000. doi:10.1038/gt.2014.74

Pignataro, D., Sucunza, D., Vanrell, L., Lopez-Franco, E., Dopeso-Reyes, I. G., Vales, A., . . . Gonzalez-Aseguinolaza, G. (2017). Adeno-Associated Viral Vectors Serotype 8 for Cell-Specific Delivery of Therapeutic Genes in the Central Nervous System. *Front Neuroanat, 11*, 2. doi:10.3389/fnana.2017.00002

Pnevmatikakis, E. A., & Giovannucci, A. (2017). NoRMCorre: An online algorithm for piecewise rigid motion correction of calcium imaging data. *J Neurosci Methods, 291*, 83-94. doi:10.1016/j.jneumeth.2017.07.031

Porter, J. T., & McCarthy, K. D. (1996). Hippocampal astrocytes in situ respond to glutamate released from synaptic terminals. *J Neurosci, 16*(16), 5073-5081. doi:10.1523/JNEUROSCI.16-16-05073.1996

Poskanzer, K. E., & Yuste, R. (2016). Astrocytes regulate cortical state switching in vivo. *Proc Natl Acad Sci U S A, 113*(19), E2675-2684. doi:10.1073/pnas.1520759113

Riera, J., Hatanaka, R., Ozaki, T., & Kawashima, R. (2011). Modeling the spontaneous Ca2+ oscillations in astrocytes: Inconsistencies and usefulness. *J Integr Neurosci, 10*(4), 439-473. doi:10.1142/S0219635211002877

Riera, J., Hatanaka, R., Uchida, T., Ozaki, T., & Kawashima, R. (2011). Quantifying the uncertainty of spontaneous Ca2+ oscillations in astrocytes: particulars of Alzheimer's disease. *Biophys J, 101*(3), 554-564. doi:10.1016/j.bpj.2011.06.041

Riera, J. J., Schousboe, A., Waagepetersen, H. S., Howarth, C., & Hyder, F. (2008). The micro-architecture of the cerebral cortex: functional neuroimaging models and metabolism. *Neuroimage, 40*(4), 1436-1459. doi:10.1016/j.neuroimage.2007.12.051

Ritter, E., Stehfest, K., Berndt, A., Hegemann, P., & Bartl, F. J. (2008). Monitoring light-induced structural changes of Channelrhodopsin-2 by UV-visible and Fourier transform infrared spectroscopy. *J Biol Chem, 283*(50), 35033-35041. doi:10.1074/jbc.M806353200

Robel, S., Berninger, B., & Gotz, M. (2011). The stem cell potential of glia: lessons from reactive gliosis. *Nat Rev Neurosci, 12*(2), 88-104. doi:10.1038/nrn2978

Robillard, J. M., Gordon, G. R., Choi, H. B., Christie, B. R., & MacVicar, B. A. (2011). Glutathione restores the mechanism of synaptic plasticity in aged mice to that of the adult. *PloS one, 6*(5), e20676. doi:10.1371/journal.pone.0020676

Rodriguez-Arellano, J. J., Parpura, V., Zorec, R., & Verkhratsky, A. (2016). Astrocytes in physiological aging and Alzheimer's disease. *Neuroscience, 323*, 170-182. doi:10.1016/j.neuroscience.2015.01.007

Rosenegger, D. G., & Gordon, G. R. (2015). A slow or modulatory role of astrocytes in neurovascular coupling. *Microcirculation, 22*(3), 197-203. doi:10.1111/micc.12184

Ruitenberg, M. J., Eggers, R., Boer, G. J., & Verhaagen, J. (2002). Adeno-associated viral vectors as agents for gene delivery: application in disorders and trauma of the central nervous system. *Methods, 28*(2), 182-194. doi:10.1016/s1046-2023(02)00222-0

Salegio, E. A., Samaranch, L., Kells, A. P., Mittermeyer, G., San Sebastian, W., Zhou, S., . . . Bankiewicz, K. S. (2013). Axonal transport of adeno-associated viral vectors is serotype-dependent. *Gene therapy, 20*(3), 348-352. doi:10.1038/gt.2012.27

Savtchenko, L. P., Bard, L., Jensen, T. P., Reynolds, J. P., Kraev, I., Medvedev, N., . . . Rusakov, D. A. (2018). Disentangling astroglial physiology with a realistic cell model in silico. *Nat Commun, 9*(1), 3554. doi:10.1038/s41467-018-05896-w

Savtchouk, I., & Volterra, A. (2018). Gliotransmission: Beyond Black-and-White. *J Neurosci, 38*(1), 14-25. doi:10.1523/JNEUROSCI.0017-17.2017

Schindelin, J., Arganda-Carreras, I., Frise, E., Kaynig, V., Longair, M., Pietzsch, T., . . . Cardona, A. (2012). Fiji: an open-source platform for biological-image analysis. *Nat Methods, 9*(7), 676-682. doi:10.1038/nmeth.2019

Schober, A. L., Gagarkin, D. A., Chen, Y., Gao, G., Jacobson, L., & Mongin, A. A. (2016). Recombinant Adeno-Associated Virus Serotype 6 (rAAV6) Potently and Preferentially Transduces Rat Astrocytes In vitro and In vivo. *Front Cell Neurosci, 10*, 262. doi:10.3389/fncel.2016.00262

Schummers, J., Yu, H., & Sur, M. (2008). Tuned responses of astrocytes and their influence on hemodynamic signals in the visual cortex. *Science, 320*(5883), 1638-1643. doi:10.1126/science.1156120

Seiffert, E., Dreier, J. P., Ivens, S., Bechmann, I., Tomkins, O., Heinemann, U., & Friedman, A. (2004). Lasting blood-brain barrier disruption induces epileptic focus in the rat somatosensory cortex. *Journal of Neuroscience, 24*(36), 7829-7836.

Shigetomi, E., Saito, K., Sano, F., & Koizumi, S. (2019). Aberrant Calcium Signals in Reactive Astrocytes: A Key Process in Neurological Disorders. *Int J Mol Sci, 20*(4), 996. doi:10.3390/ijms20040996

Shuai, J.-W., & Jung, P. (2002). Stochastic properties of Ca2+ release of inositol 1, 4, 5-trisphosphate receptor clusters. *Biophysical journal, 83*(1), 87-97. doi:10.1016/S0006-3495(02)75151-5

Sirko, S., Behrendt, G., Johansson, P. A., Tripathi, P., Costa, M., Bek, S., . . . Gotz, M. (2013). Reactive glia in the injured brain acquire stem cell properties in response to sonic hedgehog. [corrected]. *Cell stem cell, 12*(4), 426-439. doi:10.1016/j.stem.2013.01.019

Skupin, A., Kettenmann, H., & Falcke, M. (2010). Calcium signals driven by single channel noise. *PLoS Comput Biol, 6*(8), e1000870. doi:10.1371/journal.pcbi.1000870

Skupin, A., Kettenmann, H., Winkler, U., Wartenberg, M., Sauer, H., Tovey, S. C., . . . Falcke, M. (2008). How does intracellular Ca2+ oscillate: by chance or by the clock? *Biophysical journal, 94*(6), 2404-2411. doi:10.1529/biophysj.107.119495

Smith, G. D., Wagner, J., & Keizer, J. (1996). Validity of the rapid buffering approximation near a point source of calcium ions. *Biophys J, 70*(6), 2527-2539. doi:10.1016/S0006-3495(96)79824-7

Sneyd, J., & Falcke, M. (2005). Models of the inositol trisphosphate receptor. *Prog Biophys Mol Biol, 89*(3), 207-245. doi:10.1016/j.pbiomolbio.2004.11.001

Somjen, G. G. (1988). Nervenkitt: notes on the history of the concept of neuroglia. *Glia, 1*(1), 2-9. doi:10.1002/glia.440010103

Steardo Jr, L., Bronzuoli, M. R., Iacomino, A., Esposito, G., Steardo, L., & Scuderi, C. (2015). Does neuroinflammation turn on the flame in Alzheimer's disease? Focus on astrocytes. *Frontiers in neuroscience, 9*. doi:10.3389/fnins.2015.00259.

Stefanescu, R. A., Shivakeshavan, R. G., Khargonekar, P. P., & Talathi, S. S. (2013). Computational modeling of channelrhodopsin-2 photocurrent characteristics in relation to neural signaling. *Bull Math Biol, 75*(11), 2208-2240. doi:10.1007/s11538-013-9888-4

Steinhäuser, C., Grunnet, M., & Carmignoto, G. (2016). Crucial role of astrocytes in temporal lobe epilepsy. *Neuroscience, 323*, 157-169.

Stobart, J. L., Ferrari, K. D., Barrett, M. J. P., Stobart, M. J., Looser, Z. J., Saab, A. S., & Weber, B. (2018). Long-term In Vivo Calcium Imaging of Astrocytes Reveals Distinct Cellular Compartment Responses to Sensory Stimulation. *Cereb Cortex, 28*(1), 184-198. doi:10.1093/cercor/bhw366

Stout, C. E., Costantin, J. L., Naus, C. C., & Charles, A. C. (2002). Intercellular calcium signaling in astrocytes via ATP release through connexin hemichannels. *Journal of Biological Chemistry, 277*(12), 10482-10488.

Sun, S., & Schaffer, D. V. (2018). Engineered viral vectors for functional interrogation, deconvolution, and manipulation of neural circuits. *Current opinion in neurobiology, 50*, 163-170.

Sun, W., McConnell, E., Pare, J. F., Xu, Q., Chen, M., Peng, W., . . . Nedergaard, M. (2013). Glutamate-dependent neuroglial calcium signaling differs between young and adult brain. *Science, 339*(6116), 197-200. doi:10.1126/science.1226740

Suzuki, M., & Larkum, M. E. (2017). Dendritic calcium spikes are clearly detectable at the cortical surface. *Nat Commun, 8*(1), 276. doi:10.1038/s41467-017-00282-4

Takano, T., He, W., Han, X., Wang, F., Xu, Q., Wang, X., . . . Nedergaard, M. (2014). Rapid manifestation of reactive astrogliosis in acute hippocampal brain slices. *Glia, 62*(1), 78-95. doi:10.1002/glia.22588

Takano, T., Tian, G. F., Peng, W., Lou, N., Libionka, W., Han, X., & Nedergaard, M. (2006). Astrocyte-mediated control of cerebral blood flow. *Nat Neurosci, 9*(2), 260-267. doi:10.1038/nn1623

Takata, N., Nagai, T., Ozawa, K., Oe, Y., Mikoshiba, K., & Hirase, H. (2013). Cerebral blood flow modulation by basal forebrain or whisker stimulation can occur independently of large cytosolic Ca 2+ signaling in astrocytes. *PloS one, 8*(6), e66525. doi:10.1371/journal.pone.0066525

Takata, N., Sugiura, Y., Yoshida, K., Koizumi, M., Hiroshi, N., Honda, K., . . . Suematsu, M. (2018). Optogenetic astrocyte activation evokes BOLD fMRI response with oxygen

consumption without neuronal activity modulation. *Glia, 66*(9), 2013-2023. doi:10.1002/glia.23454

Tanaka, K. F., Matsui, K., Sasaki, T., Sano, H., Sugio, S., Fan, K., . . . Yamanaka, A. (2012). Expanding the repertoire of optogenetically targeted cells with an enhanced gene expression system. *Cell Rep, 2*(2), 397-406. doi:10.1016/j.celrep.2012.06.011

Theodosis, D. T., Poulain, D. A., & Oliet, S. H. (2008). Activity-dependent structural and functional plasticity of astrocyte-neuron interactions. *Physiol Rev, 88*(3), 983-1008. doi:10.1152/physrev.00036.2007

Tian, G. F., Azmi, H., Takano, T., Xu, Q., Peng, W., Lin, J., . . . Nedergaard, M. (2005). An astrocytic basis of epilepsy. *Nat Med, 11*(9), 973-981. doi:10.1038/nm1277

Van Kampen, N. (2007). *Stochastic processes in physics and chemistry*. Retrieved from

Verkhratsky, A., & Kettenmann, H. (1996). Calcium signalling in glial cells. *Trends Neurosci, 19*(8), 346-352. doi:10.1016/0166-2236(96)10048-5

Verkhratsky, A., & Nedergaard, M. (2018). Physiology of Astroglia. *Physiol Rev, 98*(1), 239-389. doi:10.1152/physrev.00042.2016

Verkhratsky, A., Rodriguez, J. J., & Parpura, V. (2014). Neuroglia in ageing and disease. *Cell Tissue Res, 357*(2), 493-503. doi:10.1007/s00441-014-1814-z

Verkhratsky, A., Steardo, L., Parpura, V., & Montana, V. (2016). Translational potential of astrocytes in brain disorders. *Prog Neurobiol, 144*, 188-205. doi:10.1016/j.pneurobio.2015.09.003

Verkhratsky, A., Zorec, R., Rodriguez, J. J., & Parpura, V. (2016). Astroglia dynamics in ageing and Alzheimer's disease. *Curr Opin Pharmacol, 26*, 74-79. doi:10.1016/j.coph.2015.09.011

Volterra, A., Liaudet, N., & Savtchouk, I. (2014). Astrocyte Ca 2+ signalling: an unexpected complexity. *Nature Reviews Neuroscience, 15*(5), 327-335. doi:10.1038/nrn3725

Volterra, A., & Meldolesi, J. (2005). Astrocytes, from brain glue to communication elements: the revolution continues. *Nat Rev Neurosci, 6*(8), 626-640. doi:10.1038/nrn1722

Wang, H., Peca, J., Matsuzaki, M., Matsuzaki, K., Noguchi, J., Qiu, L., . . . Deisseroth, K. (2007). High-speed mapping of synaptic connectivity using photostimulation in Channelrhodopsin-2 transgenic mice. *Proceedings of the National Academy of Sciences, 104*(19), 8143-8148. doi:10.1073/pnas.0700384104

Wang, X., Lou, N., Xu, Q., Tian, G.-F., Peng, W. G., Han, X., . . . Nedergaard, M. (2006). Astrocytic Ca 2+ signaling evoked by sensory stimulation in vivo. *Nature neuroscience, 9*(6), 816-823. doi:10.1038/nn1703

Watras, J., & Ehrlich, B. E. (1991). Bell-shaped calcium-response curves of lns (l, 4, 5) P 3-and calcium-gated channels from endoplasmic reticulum of cerebellum. *Nature, 351*(6329), 751-754. doi:10.1038/351751a0

Weinberg, M. S., Samulski, R. J., & McCown, T. J. (2013). Adeno-associated virus (AAV) gene therapy for neurological disease. *Neuropharmacology, 69*, 82-88. doi:10.1016/j.neuropharm.2012.03.004

Williams, J. C., Xu, J., Lu, Z., Klimas, A., Chen, X., Ambrosi, C. M., . . . Entcheva, E. (2013). Computational optogenetics: empirically-derived voltage- and light-sensitive channelrhodopsin-2 model. *PLoS Comput Biol, 9*(9), e1003220. doi:10.1371/journal.pcbi.1003220

Williams, V., Grossman, R. G., & Edmunds, S. M. (1980). Volume and surface area estimates of astrocytes in the sensorimotor cortex of the cat. *Neuroscience, 5*(7), 1151-1159. doi:10.1016/0306-4522(80)90194-3

Yang, G. S., Schmidt, M., Yan, Z., Lindbloom, J. D., Harding, T. C., Donahue, B. A., . . . Davidson, B. L. (2002). Virus-mediated transduction of murine retina with adeno-associated virus: effects of viral capsid and genome size. *J Virol, 76*(15), 7651-7660. doi:10.1128/jvi.76.15.7651-7660.2002

Zarb, Y., Weber-Stadlbauer, U., Kirschenbaum, D., Kindler, D. R., Richetto, J., Keller, D., . . . Byzova, T. (2019). Ossified blood vessels in primary familial brain calcification elicit a neurotoxic astrocyte response. *Brain*.

Zincarelli, C., Soltys, S., Rengo, G., & Rabinowitz, J. E. (2008). Analysis of AAV serotypes 1-9 mediated gene expression and tropism in mice after systemic injection. *Mol Ther, 16*(6), 1073-1080. doi:10.1038/mt.2008.76

VITA

LAKSHMINI BALACHANDAR

Born, Chennai, India

2008-2012	B.Tech., Bioengineering SASTRA University Thanjavur, India
2013-2021	PhD, Biomedical Engineering Florida International University Miami, Florida

PUBLICATIONS AND PRESENTATIONS

Balachandar, L., Montejo, K. A., Castano, E., Perez, M., Moncion, C., Chambers, J. W., Lujan, J.L., & Diaz, J. R. (2020). *Simultaneous Ca^{2+} Imaging and Optogenetic Stimulation of Cortical Astrocytes in Adult Murine Brain Slices*. Current Protocols in Neuroscience, 94(1), e110.

Moshkforoush, A.*, Balachandar, L.*, Moncion, C.*, Montejo, K. A., & Riera, J. (2021). *Unraveling ChR2-driven stochastic Ca^{2+} dynamics in astrocytes: A call for new interventional paradigms*. PLOS Computational Biology, 17(2), e1008648. (* equal author contribution).

Balachandar, L., Borrego, D., & Riera, J.R. *An in vivo evaluation of optogenetic construct serotypes targeting rat cortical astrocytes*, (Manuscript ready to be submitted).

Balachandar, L., Moncion, C., Montejo, K. A., & Diaz, J. R. *Identifying light stimulation paradigms for robust astrocytic Ca^{2+} signaling: An in situ evaluation*. (Manuscript under preparation to be submitted to Glia).

Moncion, C., Balachandar, L., Bojja-Venkatakrishnan, S., Riera, J. J., & Volakis, J. L. (2019). *Fully-passive wireless implant for neuropotential acquisition: An In Vivo validation*. IEEE Journal of Electromagnetics, RF and Microwaves in Medicine and Biology, 3(3), 199-205.

Liu, S., Moncion, C., Zhang, J., Balachandar, L., Kwaku, D., Riera, J. J., Volakis, J.L., & Chae, J. (2019). *Fully Passive Flexible Wireless Neural Recorder for the Acquisition of Neuropotentials from a Rat Model*. ACS sensors, 4(12), 3175-3185.

Moncion, C., Borges, J., Balachandar, L., Venkatakrishnan, S. B., Diaz, J. R., & Volakis, J. L. (2019). *In Vivo Evaluation of a Fully-Passive Wireless Neurosensing System*.

International Workshop on Antenna Technology (pp. 37-40), IEEE. Miami, Florida.

Balachandar, L., Moshkforoush, A., Moncion, C., Montejo, K.A., Perez, M., Castano, E., Laffitte, C., & Riera, J. (2019). *Unraveling ChR2-driven Stochastic Ca^{2+} Dynamics in Astrocytes-A Call for New Interventional Paradigms*. Society for Neuroscience, Chicago, Illinois.

Balachandar, L., Moshkforoush, A., Moncion, C., Perez, M., Montejo, K.A., Santana, J., & Riera, J. (2019). *Unraveling ChR2-driven Stochastic Ca^{2+} Dynamics in Astrocytes-A Call for New Interventional Paradigms*. Brain Satellite Workshop, Suwon, South Korea.

Balachandar, L., Borrego, D., & Riera, J. (2017). *Evaluation of an optogenetic construct in rat cortical astrocytes to target neuroinflammation in epilepsy*. American Epilepsy Society Conference, Washington D.C.

Balachandar, L., Borrego, D., & Riera, J. (2016). *Serotype-based evaluation of an optogenetic construct in rat cortical astrocytes.* Society for Neuroscience, San Diego, California.

Balachandar, L., Santana, J., & Riera, J. (2015). *A Quantitative evaluation of optogenetically induced calcium signaling in Astrocytes.* Biomedical Engineering Society Conference, Tampa, Florida.

Balachandar, L., Raymond, A., Nair, M., Santana, J., & Riera, J. (2014). *A Quantitative evaluation of optogenetically induced calcium signaling in Astrocytes.* Society for Neuroscience, Washington D.C.

Moncion, C., Balachandar, L., Bojja-Venkatakrishnan, S., Kiourti, A., Riera, J. J., & Volakis, J. L. (2021). *Passive Wireless Neurosensing System for Multi-Unit Neuronal Activity Monitoring*. National Radio Science Meeting, Boulder, Colorado.

Moncion, C., Balachandar, L., Bojja-Venkatakrishnan, S., Riera, J. J., & Volakis, J. L. (2019). *In Vivo Recording of Epileptiform Neural Activation using a Novel Fully-Passive Implantable System*. National Radio Science Meeting, Boulder, Colorado.